DETECTION AND SEGMENTATION OF MITOCHONDRIA
FROM ELECTRON MICROSCOPE TOMOGRAPHY IMAGES

A THESIS SUBMITTED TO
THE GRADUATE SCHOOL OF INFORMATICS OF
MIDDLE EAST TECHNICAL UNIVERSITY

BY

FARİS SERDAR TAŞEL

IN PARTIAL FULFILLMENT OF THE REQUIREMENTS FOR
THE DEGREE OF DOCTOR OF PHILOSOPHY
IN
MEDICAL INFORMATICS

JUNE 2016

**DETECTION AND SEGMENTATION OF MITOCHONDRIA
FROM ELECTRON MICROSCOPE TOMOGRAPHY IMAGES**

Submitted by **FARİS SERDAR TAŞEL** in partial fulfillment of the requirements for the degree of **Doctor of Philosophy in Medical Informatics, Middle East Technical University** by,

Prof. Dr. Nazife Baykal
Director, **Graduate School of Informatics**
_____

Assoc. Prof. Dr. Yeşim Aydın Son
Head of Department, **Health Informatics**
_____

Prof. Dr. Ünal Erkan Mumcuoğlu
Supervisor, **Health Informatics**
_____

Assist. Prof. Dr. Reza Zare Hassanpour
Co-Supervisor, **Department of Computer Engineering,
Çankaya University**
_____

Examining Committee Members:

Assoc. Prof. Dr. Tolga Esat Özkurt
Health Informatics, METU
_____

Prof. Dr. Ünal Erkan Mumcuoğlu
Health Informatics, METU
_____

Assist. Prof. Dr. Aybar Can Acar
Health Informatics, METU
_____

Assoc. Prof. Dr. Hadi Hakan Maraş
Computer Engineering, Çankaya Univ.
_____

Assoc. Prof. Dr. Pınar Duygulu Şahin
Computer Engineering, Hacettepe Univ.
_____

Date: 10/06/2016

I hereby declare that all information in this document has been obtained and presented in accordance with academic rules and ethical conduct. I also declare that, as required by these rules and conduct, I have fully cited and referenced all material and results that are not original to this work.

Name, Last name: Faris Serdar Taşel

Signature   :   _____

ABSTRACT

DETECTION AND SEGMENTATION OF MITOCHONDRIA FROM ELECTRON MICROSCOPE TOMOGRAPHY IMAGES

Taşel, Faris Serdar
Supervisor: Prof. Dr. Ünal Erkan Mumcuoğlu
Co-Supervisor: Assist. Prof. Dr. Reza Zare Hassanpour

May 2016, 89 pages

Recent studies exhibit that mitochondria have a significant role in cellular functions that are associated to the diseases of aging caused by neuron degeneration. These studies accentuate that the peripheral membrane and crista morphology of a mitochondrion deserves attention in order to reveal the relation between mitochondrial function and its physical structure. The analysis of the inner structures of mitochondria is carried out by electron microscope tomography (EMT) which provides detailed visualization of large volumes. In order to accelerate the studies that investigate the correlation between mitochondrial structure and its function, computerized segmentation of mitochondria with minimum manual effort is required. As a preliminary study, 2D detection and segmentation of mitochondria from transmission electron microcopy (TEM) images were performed on a limited dataset. An ellipse fitting algorithm utilizing double membrane features followed by a balloon snake extraction and a livewire-based automatic segmentation refinement process was applied. By considering the deficiencies of the initial attempt, a curve fitting approach was adopted and tested on a several datasets. For this purpose, a membrane extraction process was performed by utilizing a parabolic arc model. Then, active contour model based on curve energy was used to outline candidate mitochondrial regions. The final segmentation data were obtained by a validator function. Additionally, 3D extension of the algorithms were studied and provided. The proposed method achieved an F-score performance of 0.84 on average. Average Dice similarity coefficient and median boundary error were measured as 0.87 and 14 nm respectively.

Keywords: Image Processing, Electron tomography, Curve fitting, Active contour, Mitochondrion

ÖZ

ELEKTRON MİKROSKOBU TOMOGRAFİSİ GÖRÜNTÜLERİNDEN MİTOKONDRİLERİN SAPTANMASI VE BÖLÜTLENMESİ

Taşel, Faris Serdar
Tez Danışmanı: Prof. Dr. Ünal Erkan Mumcuoğlu
Yardımcı Tez Danışmanı: Yrd. Doç. Dr. Reza Zare Hassanpour

Mayıs 2016, 89 sayfa

Güncel çalışmalar, yaşlılığa bağlı olarak nöronların dejenerasyonu nedeniyle ortaya çıkan hastalıklara ilişkin hücresel işlevlerde mitokondrilerin önemli sorumluluk taşımakta olduklarını ortaya çıkarmıştır. Bu çalışmalar, mitokondri işlevinin ve fiziksel yapısının arasındaki ilişkinin araştırılması açısından mitokondrilerin membran ve krista yapısına dikkat çekilmesi gerektiğini vurgulamaktadır. Elektron mikroskobu tomografisi (EMT), geniş hacimlerde yüksek detayda görsel veri sağlayarak mitokondrinin içyapısının incelenmesine imkân tanımaktadır. Mitokondrilerin el ile harcanan eforun en aza indirilerek bilgisayarla bölütlenmesi, mitokondri yapısı ve işlevi arasındaki bağıntının çalışmasına hız kazandırılması açısından temel bir öneme sahiptir. Hazırlık çalışması olarak, kısıtlı bir veri seti üzerinde Geçirimli Elektron Mikroskobu (GEM) görüntülerinden mitokondrilerin 2B saptanması ve bölütlenmesi gerçekleştirilmiştir. Çift membran özniteliklerini kullanan bir elips uydurma algoritmasını takiben balon yılan çıkarımı ve canlı-tel tabanlı otomatik bölütleme iyileştirme işlemi uygulanmıştır. İlk yöntemin yetersizlikleri göz önünde bulundurularak, bir eğri uydurma yaklaşımı benimsenmiş ve çeşitli veri setleri üzerinde test edilmiştir. Bu amaçla, membran yapılarının çıkarılması için parabolik yay modeli kullanılmıştır. Daha sonra, ana hatlarını kabaca çevreleyen aday mitokondri bölgelerini elde etmek amacıyla eğri enerjisi tabanlı aktif çevritler çalıştırılmıştır. Bir geçerleme fonksiyonu yardımı ile son bölütleme verisi elde edilmiştir. Ayrıca, algoritmaların 3B uyarlanması çalışılmış ve gösterilmiştir. Öne sürülen yöntemin ulaşmış olduğu F-skoru performansı ortalama 0.84'tür. Ortalama Dice benzerliği katsayısı ve sınır hatası sırasıyla 0.87 ve 14 nm olarak ölçülmüştür.

Anahtar Kelimeler: Görüntü İşleme, Elektron tomografisi, Eğri Uydurma, Aktif Çevrit, Mitokondri

DEDICATION

In loving memory of my beloved mother

ACKNOWLEDGMENTS

TABLE OF CONTENTS

LIST OF TABLES

LIST OF FIGURES

xii

xv

LIST OF ABBREVIATIONS

2D	:	Two Dimensions
2.5D	:	Two-and-half Dimensions
3D	:	Three Dimensions
AdaBoost	:	Adaptive Boosting
CCD	:	Charge-Coupled Device
CCDB	:	Cell Centered Database
CHM	:	Cascaded Hierarchical Model
cryoET	:	Cryotomography
DBSCAN	:	Density-Based Spatial Clustering of Applications with Noise
DSC	:	Dice Similarity Coefficient
EMT	:	Electron Microscope Tomography
ER	:	Endoplasmic Reticulum
HFREM	:	High Frequency Ridge Energy Map
kNN	:	k-Nearest Neighbor
LFREM	:	Low Frequency Ridge Energy Map
MSBE	:	Median Symmetric Boundary Error
NCMIR	:	National Center for Microscopy and Imaging Research
SBFSEM	:	Serial Block-Face Scanning Electron Microscopy
SEM	:	Scanning Electron Microscopy
SNR	:	Signal-to-Noise Ratio
SV	:	Synaptic Vesicle
SVM	:	Support Vector Machine
TEM	:	Transmission Electron Microscopy

CHAPTER 1

INTRODUCTION

This study presents an investigation for computerized detection and segmentation of mitochondria from electron tomography. The introduction section encapsulates notable morphological properties of mitochondria and highlights imaging techniques which are used to visualize subcellular structures in detail. Motivating factors, aims and scope of this study are described in the following sections. A comprehensive review of studies published in related areas is additionally introduced.

1.1. Mitochondrion

A mitochondrion is a subcellular structure that mainly controls the synthesis of adenosine-triphosphate used as the source of energy. It has substantial responsibility in organization of several cellular activities and actions such as cell division cycle, cellular differentiation, cell signaling, cell growth and programmed cell death which is also known as apoptosis [1], [2]. Correlation of mitochondrial structure and its function is receiving remarkable attention as the link between mitochondrial function and degenerative disorders associated to aging such as Parkinson's and Alzheimer's diseases is emphasized by recent studies [3]–[5].

Mitochondria are pleomorphic and have a distorted ellipsoid shape with different size depending on cell type, tissue type and the physical connection of other sub-cellular structures. The cell may contain many mitochondria that are close or even touching to each other. Mitochondria have double membranes: an outer membrane which surrounds the whole mitochondrion and an inner membrane which extends along the inner side of the outer membrane. Mitochondria have also crista structures inside [6]. Crista structures and inner membrane are connected by small tubular structures called crista junctions. Morphological deformation in the mitochondrial structure may occur with the presence of a disorder or a disease in the functions of mitochondria [7], [8].

The diameter of majority of mitochondria is usually 0.25 μm or larger. It is an unusual case for mitochondria to have the width (the size of the smallest cross-section) larger than 2 μm. However, the length (the size of the largest cross-section) of mitochondria can be 20 μm or longer. Typical mitochondrial membrane thickness for different cell types is in 4–6 nm range [9]. The mitochondrial inner and outer membrane separation
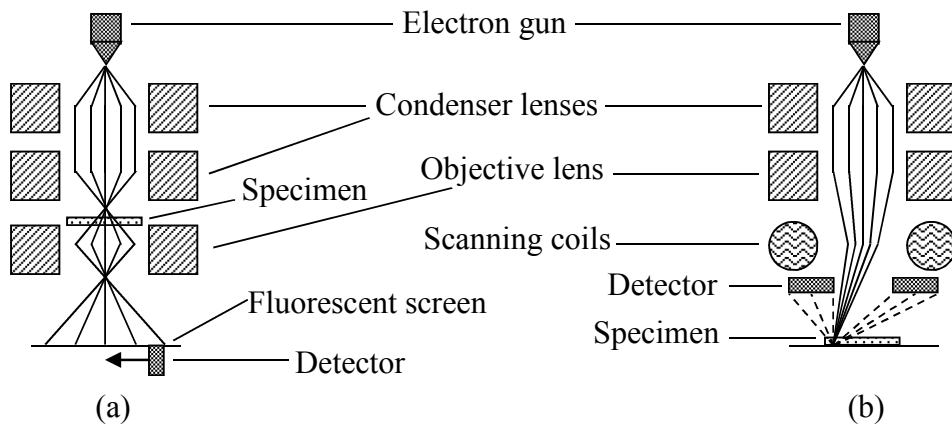
Figure 1: Schematics for (a) Transmission Electron Microscopy and (b) Scanning Electron Microscopy.

is mostly uniform in healthy cells. This separation is roughly in the range of 10–36 nm (mean ± two standard deviation) for the majority of cell types [10]–[13].

Mitochondria are commonly visualized by several imaging techniques based on electron microscope tomography (EMT). In tomographic images, the mitochondria appear as mostly elliptical structures and the cristae appear as small circular or elongated structures according to the orientation of slices. Membrane structures and separation of inner and outer membrane of mitochondria are also visualized in tomographic images.

1.2.   Imaging Techniques

EMT facilitates effective analysis of subcellular structures. Three dimensional (3D) visualization of mitochondria has a vital importance since the detailed investigation of high-resolution morphological deformations in mitochondria is necessary to expose mitochondrial function-disease correlations [14], [15]. The resolution of the tomographic volume and structural integrity of the sample affect visualization details. In order to segment mitochondria in detail from such volumes, both peripheral and cristae should be visualized in high contrast with respect to the image background.

EMT images can be obtained by several electron microscopy techniques. Two popular techniques to obtain electron microscope images are Transmission Electron Microscopy (TEM) and Scanning Electron Microscopy (SEM). These techniques are briefly described in the following subsections.

1.2.1. Transmission Electron Microscopy

In TEM technique [16], [17], an electron beam is produced by an electron gun and projected by electric field that is generated by condenser and objective lenses (see
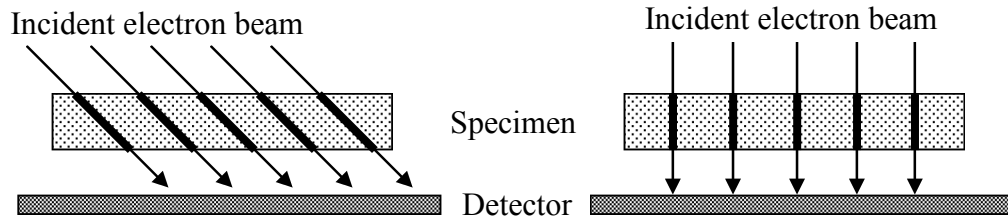
Figure 2: Projection and detection of tilted electron beams with different angles in Transmission Electron Microscopy Tomography (TEM).

Figure 1a). The electron beam creates an image on the fluorescent screen after it penetrates through an ultra-thin specimen. The intensity on this image is proportional to the projected electron density and it is measured by a detector. The projected electron density depends on the amount of electron absorption by the tissue that yields the total density on the path where the electron beam passes through. The detector scans the projected image to obtain projection data. This process is then repeated for different tilt angles of the electron beams or the specimen. Thus, projection data which correspond to the density sums on different paths are obtained as illustrated in Figure 2. Back-projection techniques in spatial or in Fourier domain may be applied to the projection data to obtain 3D reconstructed image [18]. The tilt angles are physically limited to a typical range of ±70°. The angular separation of each consecutive projection is typically 1°-2°. These limitations cause some reconstruction artifacts such that particles may appear elongated in the direction normal to the surface of the specimen. Another limitation is the thickness of the specimen that must allow sufficient penetration. The visualization of microscopic structures is possible in a resolution of down to a few nm by TEM tomography [19], [20]. The 3D image obtained by this technique is typically large in two dimensions (x and y axes) but thin in the third dimension (z axis). Therefore, entire mitochondrion may not be visualized in TEM tomography. But a detailed 3D membrane and crista structures can be reconstructed. TEM tomography exposes the peripheral and crista membrane heavy-metal staining and provides a clear imaging of the double membrane structure of mitochondria and cristae as well as other subcellular structures such as synaptic vesicles (SV) and the endoplasmic reticulum (ER).

1.2.2. Scanning Electron Microscopy

In SEM technique, the surface of specimen is visualized in two dimension (2D). The electron beam is focused on the specimen and deflected by the electric field which is generated by the scanning coils (see Figure 1b). The electrons hit the surface of specimen and scatter. The intensity of electrons back-scattered from the surface is measured by a detector. In order to obtain a 2D image, electron beams are deflected onto different locations to scan the whole surface. The acquisition of a 3D volume can be achieved by utilizing a special type of SEM technique which is called Serial Block-Face Scanning Electron Microscopy (SBFSEM). In SBFSEM technique [21], a stack

3
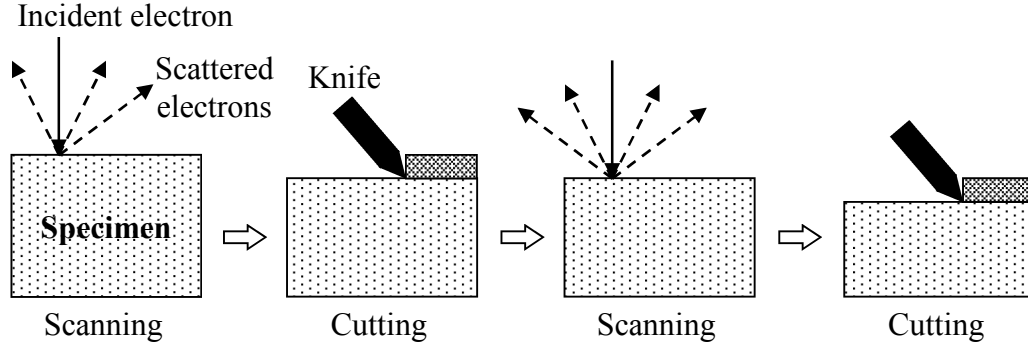
Figure 3: Scanning and cutting phases in Serial Block-Face Scanning Electron Microscopy (SBFSEM).

of 2D images are obtained by cutting ultra-thin sections from the surface using a diamond knife and then imaging by SEM (see Figure 3). This technique supplies 3D volumetric data formed by a series of 2D images each associated to a single slice. But, there is no limitation for the number of slices and specimen thickness. Typical image size of 3D datasets provided by this modality is $5 - 10$ nm in x- and y-axes and $20 - 80$ nm in z-axis [22], [23]. On the contrary to TEM tomography, the slice thickness can be much higher than the lateral resolution.

1.3. Motivation

Mitochondria segmentation of renders possible to study mitochondrial morphology and to perform computerized analysis and diagnosis. A manual segmentation by utilizing specialized software tools such as IMOD [24] and Amira is currently necessary to visually investigate tomographic volumes of mitochondria. However, flawed results may be obtained by hand segmentation of features of a volume due to human error even with highly trained experts. Moreover, considering that the size of mitochondria changes between 0.3 and 10 μm, large 3D tomographic volumes are frequently required to analyze the physical structure of entire mitochondria [2]. Because mitochondria appear in many different forms due to its pleomorphic structure depending on cell type, preparation process of the sample, respiration or disease state, a flawless automated mitochondrion segmentation is still an unsolved problem.

Perkins and colleagues [13] hypothesized that various structural features pertaining to mitochondria including the membrane thickness of the peripheral inner and outer membranes and cristae, the number of crista segments, junctions and contact site diameters have potential effect on the function of mitochondria. The motivation of this study originates from the need for the cristae segmentation which entails the development of an automatized segmentation algorithm for the peripheral membrane of mitochondria to be used in TEM tomography.

4

(a) (b)
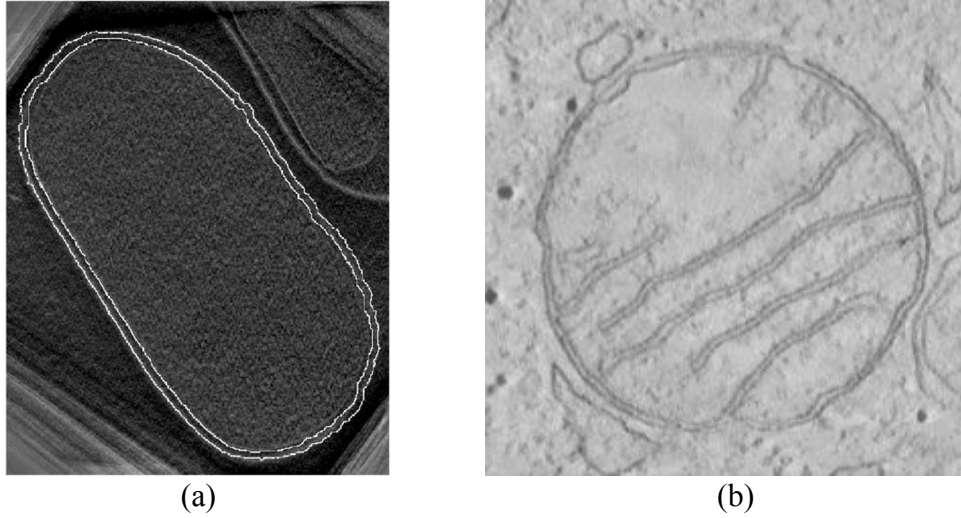
Figure 4: Tested mitochondrion images in the study of (a) Nguyen and Ji [25] and (b) Bazán et al. [27].

1.4. Aims and Scope

This dissertation covers the development of automatized algorithms for detection and segmentation of mitochondria from TEM tomography and realization of a quantitative performance evaluation. The detection procedure involves the localization of both full and partially seen mitochondria from a set of tomograms. The segmentation is limited to the determination of peripheral membrane of the detected mitochondria. The performance measurement includes testing the behavior of detection and segmentation algorithms for several mitochondria having various sizes and shapes.

1.5. Literature Review

Current studies on the segmentation of the cell or sub-cellular structures such as mitochondria are mostly based on the detecting membrane-like structures and distinguishing them from the background on the images acquired by TEM or SEM imaging techniques. The importance of processing high throughput data with minimal user interaction is being emphasized in these studies. Although the segmentation methods covered in this section were applied on mitochondria or neurons, they are generally not organelle or cell specific algorithms.

In a study by Nguyen and Ji [25], a proposed watersnake model expresses the classic watershed segmentation problem as the minimization of an energy function including smoothness and a prior shape term. The prior shape term regulates the energy with respect to the similarity between the current shape and reference shapes. Reference shapes are the previously segmented sample shapes of the structures which are to be segmented. The watershed energy term typically depends on the gradient of the image

5

and has the minimum value on the edges in the image. The watershed segmentation method requires initial markers outside and inside the region to be segmented. The 3D extension to the algorithm is additionally presented in the study. The algorithm requires an exhaustive search to solve the minimization problem so that adaptation of the algorithm to 3D makes the model even more complicated. The study demonstrates a result of the 2D version of the algorithm for the slice images of a mitochondrion without any salient crista membrane (see Figure 4a). However, the edges of cristae can create local minima on the watershed energy term which utilizes gradient based features. No discussion or result about the effect of cristae to the performance of the algorithm is provided. Nevertheless, the study attracts attention to active contour models which are practical for segmentation of sub-cellular structures.

A segmentation approach for sub-cellular structures proposed by Narasimha et al. [26] involves texton-based classification in which some isotropic and anisotropic texture features are utilized. The method adopts a training phase of a texton dictionary for mitochondria by determining cluster centers in the feature space for both background and mitochondrial structure classes. The study comprises training of the classifier with SEM images and comparison of k-Nearest Neighbor (kNN), Support Vector Machines (SVM) and Adaptive Boosting (AdaBoost) classification methods. A 3D segmentation is achieved by applying the segmentation method slice-by-slice basis. The method is able to distinguish mitochondria membranes and cristae from the background. However, any membrane-like structure would also be classified as a mitochondrion membrane since they appear very similar. A manual elimination of segmented structures is necessary to clean up the result. The algorithm provides promising results for cristae segmentation when the mitochondrial regions are already known.

A method by Bazán et al. [27] incorporates the confidence connected and the level set method for 2D segmentation of mitochondria (see Figure 4b). Anisotropic nonlinear diffusion [28]–[30] and bilateral filtering [31]–[34] are recommended methods for denoising of electron microscopy images. The algorithm entails the initialization of the confidence connected method with some seed points provided by the user in order to produce connected components which are associated to mitochondrial regions. The approach requires a manual elimination of undesired connected components to initialize the level set method with the remaining connected components. The signed distance function of the level set employs a gradient based edge indicator function. The study demonstrates a successful segmentation of peripheral membranes and cristae of a mitochondrion. Although the level set is a robust method, the initialization of the signed distance function requires a careful manual work for the segmentation of complicated structures such as mitochondria.

In a study by Macke et al. [35], a probabilistic framework for the level set segmentation method is established to segment neurons from 2D SBFSEM images using prior information of segmentation of previous neighboring slice. In this framework, each pixel has a probability of pertaining to a class (neuron or background) depending on a distribution of the pixel intensities and previous segmentation. The signed distance

function is updated by a probabilistic approach such that minimizing energy function leads to minimization of the classification error. Exceptionally, the first slice has to be segmented using without any prior information and the segmentation of the first slice is achieved by utilizing only pixel intensity distribution. The intensity distribution is determined by the user interaction. Instead of using only intensity distribution, texture information can also be included to create a feature space for the segmentation of mitochondria. The study encourages to use prior segmentation to segment remaining slices. In this context, pseudo-3D (or two-and-half dimensional (2.5D)) approaches can be taken into consideration in segmentation problem of mitochondria.

A study by Jurrus et al. [36] presents an investigation of boundary tracking of neuron axons through SBFSEM slices. The study introduces a 2.5D scheme in which a Kalman filter [37] fed by active contours and optical flow is used. The very first slice is segmented by manually initialized watershed segmentation. Next slices are automatically traced by Kalman filter. The method is able to track and segment up to about 30 axons successfully through 100 slices of a neuron. It fails to track the correct axon when the tracked axon is not visible for too many slices. Although the algorithm was actually designed to follow the axon center, it can be modified to follow the points on mitochondrion membranes. Considering that the sub-cellular membranes appear ridge-like structures in EMT images, the algorithm can be modified to track ridge features instead of edge features.

A graph theoretical approach adopted by Turaga et al. [38] performs a segmentation of neuron from a 3D volume of SBFSEM images. In this approach, a convolutional network is responsible to create affinity graph by processing a raw 3D image without requiring any pre-processing. Manually prepared affinity graphs are necessary for training phase. It is shown that a convolutional network is able to create an affinity graph that can be easily segmented into connected components successfully by using a simple threshold. The algorithm achieves an accuracy close to manual segmentation. Although it is difficult to analyze and manipulate the features acquired by the system that remains hidden in the convolutional network, this study reveals that the graph theoretical approaches worth studying for the segmentation of mitochondrial structures. An affinity or cost graph specialized for mitochondrion can be arranged to recognize membrane patterns. Template matching methods are another way to construct such graphs. The graph search methods can be utilized to follow membranes and cristae structures in a graph and find an optimal path or surface which covers entire mitochondrion.

The intensity distribution in mitochondrial regions and differentiation from background are basically used features in mitochondria segmentation methods which are based on contour pairs and classification of random forest patches [39], supervoxel segmentation [40], [41] and spectral clustering approaches [42]. However, these methods are not capable of segmenting specimens prepared for especially cristae investigation since the intensity differentiation is markedly lost in the preparation stage of the sample. In another study [43], 2D mitochondrion images were segmented based

on algebraic curves which is useful to trace the mitochondrial boundary. However, the segmentation is effected by cristae and it is not able to separate multiple mitochondria from each other.

Segmentation of membrane-like thin structures from electron tomography are carried out by several generic methods. Hessian-based ridge detection methods was proposed to extract membrane-like structures such as mitochondria boundary, SV and ER [44]– [46]. Bartesaghi et al. [47] utilized closed geodesic curves with minimal surface to develop a semi-automated 3D segmentation procedure. Another approach was introduced by Sandberg and Brega [48] in which line and orientation filter transforms were utilized to extract local features for a contour tracing mechanism. Pantelic et al. [32] presented a bilateral edge filtering method for 2D segmentation of noisy electron microscopy and cryo-electron microscopy [49] images. Ali et al. later proposed a 3D extension for this method [50]. Seyedhosseini et al. [43] asserted a cascaded hierarchical model (CHM) which was used to segment membranes in SBFSEM and TEM tomography images and produced promising results. Page et al. [51] established another intriguing semi-automated method to perform cell segmentation which is based on watershed segmentation utilizing the diversification of structures located inside and outside of the cell. In spite of acquisition of substantial results, these procedures are not able to separate mitochondria from each other or from membranes of other subcellular structures.

The second chapter of this dissertation, a preliminary study [52] is presented in which kernel pairs are utilized to detect double membranes and 2D detection and separation of mitochondria are achieved by an ellipse fitting mechanism. Then, 2D accurate segmentation of mitochondria are performed by active contour models and a modified livewire method. The proposed algorithm depends on the successful removal of cristae in the detection step to properly locate the peripheral mitochondrial membranes.

The third chapter describes a better approach to separate peripheral membranes from cristae membranes which is based on extraction of parabolic arcs. 2D detection method involves a membrane detection process for mitochondria which is based on active contours. In this new framework [53], "an active contour model driven by a curve energy image" is used to extract candidate mitochondrial regions. As a final step, a validator function filters false detections by utilizing several features obtained from boundary continuity, curvature and signature characteristics and curve energy of the internal region. Instead of eliminating cristae (as in the preliminary study), a mechanism which uses presence of cristae as an indication of mitochondria is adopted considering that crista structures are only possessed by mitochondrion inside a cell.

The fourth chapter introduces datasets that are used for testing the proposed work. Detection and segmentation accuracy of both 2D and 3D approaches are compared and discussed. In the fifth section, a further discussion is presented. Limitations of the study and future work are additionally described.

CHAPTER 2

PRELIMINARY STUDY

Although the segmentation of mitochondria has been studied moderately, these studies suffer the lack of proper detection of mitochondria or distinguishing mitochondrial structures from other sub-cellular structures in high resolution EMT images. The aforementioned methods in the literature require hand manipulation in order to extract mitochondrial membrane from other membrane-like structures. Most of these approaches are not mitochondrion-specific and not interested in distinguishing mitochondria from other structures. Nevertheless, they emphasize that computerized segmentation is essential in order to process and prepare high amount of data for further processes such as data-mining.

The problem of automatic detection and contour extraction from large images (see Figure 5) revealing multiple mitochondria and cristae structures remains unsolved. A robust detector requires the use of information regarding mitochondrial features such as shape, internal arrangement and boundary properties. The purpose of this preliminary work is to form a basis for better understanding of mitochondria in order to develop computer algorithms to detect and segment both fully and partially seen mitochondria on EMT images by using such mitochondrial features. Minimizing user interaction is essential to provide processing of high throughput data. In this chapter, the preliminary study which involves a 2D detection and segmentation of mitochondria is summarized.

Challenging aspects of the problem can be summarized as follows:

   i.   A simple model for mitochondria is not sufficient due to the pleomorphic structure of mitochondria. Peripheral and cristae membranes appear differently in the images depending on the orientations of cross-sections. Mitochondrial shape also differs with respect to the cell type.

   ii.   Various non-mitochondrial sub-cellular structures appear together with mitochondria.

  iii.   Many mitochondria appear (even in touching to each other) in a single image.

  iv.   Cristae show different patterns (circular or elongated).

   v.   EMT provides noisy images which affect appearance of the double membrane and crista structures.
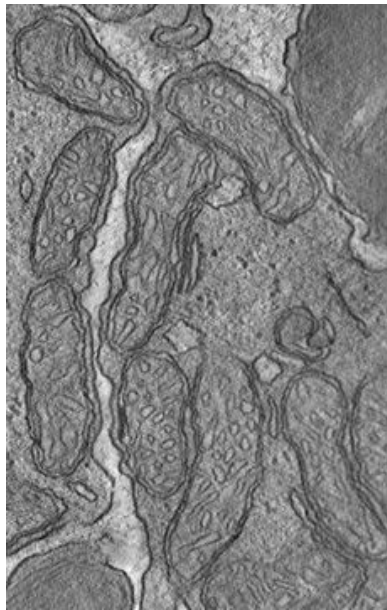
Figure 5: TEM images showing mitochondria used in the preliminary study.

In this chapter, 2D detection and segmentation of mitochondria are realized considering the following features of mitochondria:

i. Double membrane and cristae patterns are exhibited by all mitochondria.
ii. Cristae show up as elongated or small circular structures.
iii. The most of mitochondria have globular or elongated shapes (similar to ellipsoid). The diameter of the most of the mitochondrial is in the range of 0.25 μm – 2 μm in general.

2.1. Methods

The system consists of pre-processing, feature extraction, mitochondria detection and segmentation steps. These steps are summarized below:

i. **Preprocessing:** In order to facilitate optimization of parameters presented in algorithms, the image resolution is fixed to 2 nm by using interpolation. Such a resolution is sufficient to clearly identify double membrane and crista structures. Gaussian smoothing [54] is applied to the interpolated image for denoising purposes. Mitochondrial structures in a tomogram appear as ridge-like structures with a particular thickness. In order to strengthen ridges while suppressing plain regions, mean difference filter and contrast adjustment are applied to the smoothed image. Sample images are provided in Figure 6(a), (b) and (c) respectively.

ii. **Feature extraction:** In this step, a double ridge detector is employed to detect peripheral membranes of mitochondria and to provide features associated to double membranes such as strength of double membrane, membrane thickness, separation of membranes and direction. A double ridge energy image (see Figure 6(d)) is obtained from the output of the detector. Although the double ridge detector is insensitive to single ridges, it is affected by the existence of cristae and noise. In order to facilitate the mitochondria detection and segmentation, the system employs an algorithm that suppresses non-double membrane structures based on morphological and connected component analysis. In the first step, the smoothed image is normalized and thresholded to obtain a binary image (Figure 7(a)). Small particles are removed by a connected component filtering (Figure 7(b)). Then, morphological closing followed by opening is applied (Figure 7(c)). Finally, small connected components are removed again (Figure 7(d)). This algorithm removes circular shaped cristae and thin single ridges by preserving double membranes and thus it creates a template image which indicates a rough approximation of double membrane locations. In subsequent steps, the detection of double membranes are strengthened by combining the double ridge energy image with the template image created by the morphological and connected component analysis.

11
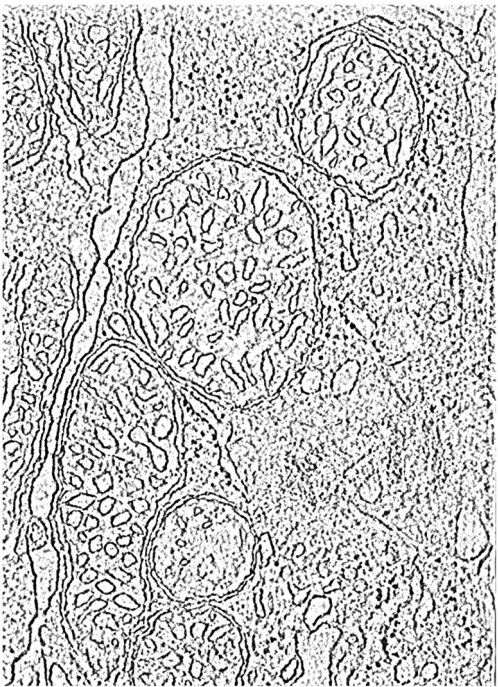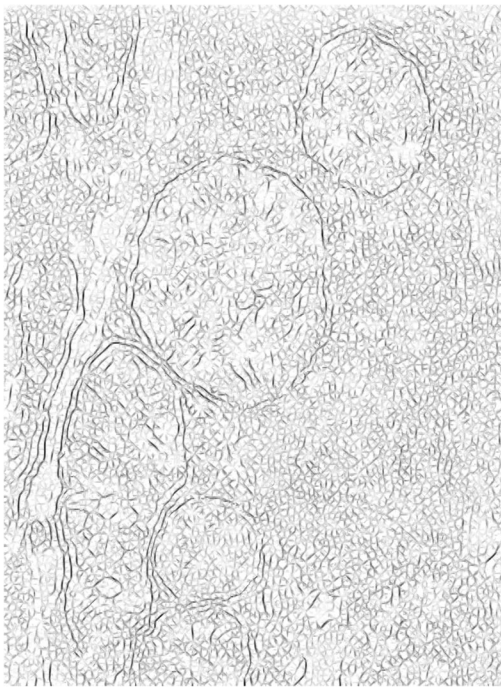
Figure 6: (a) Smoothed image; (b) mean-difference image; (c) contrast adjusted image and (d) double ridge energy image.

12

iii. **Mitochondria detection**: This step involves a mitochondria detection scheme based on the detection of ellipses. A 2D cross-section of a mitochondrion can be roughly expressed as an ellipse or the superposition of ellipses. An ellipse fitting algorithm searches candidate ellipses with different size, location and orientation. The double ridge energy image and template image prepared in the previous step is multiplied to combine both features and to increase the accuracy of double membrane detection. The image is then down-sampled to speed up the mitochondria detection step. In down-sampling process, the image is separated into blocks as shown in Figure 8. A total double ridge energy for each ridge direction is individually computed within each block. Hence, the down-sampled image contains total double ridge energy for each pair of ridge direction and block. For all boundary points of each candidate ellipse, the sum of total energy of the blocks which are associated to the angle of ellipse tangential direction is computed. Boundaries of candidate ellipses are expected to pass through the blocks with high double ridge energy. Since the shape of mitochondrion is not exactly an ellipse, neighboring blocks are also considered in evaluating ellipses as illustrated in Figure 9(a) and (b). A double membrane structure should not exist inside the ellipse. Therefore, a score is assigned to each candidate ellipse such that presence of a double ridge on the boundary gives positive contribution whereas a double ridge inside the ellipse gives negative contribution to the score. Depending on the search parameters, structure and distribution of mitochondria, false positive ellipses may be detected along with the correctly detected ellipses (see Figure 9(c)). A user interaction is necessary in this intermediate step to manually eliminate such ellipses in this preliminary study. The other detected ellipses were merged or split with respect to the amount of overlapping area. Hence, a rough detection of mitochondria is achieved as illustrated in Figure 9(d).

iv. **Mitochondria segmentation:** In segmentation step, an active contour model is used to obtain more precise boundary which improves accuracy of the segmentation. A balloon snake [55] is employed as an active contour model. Each detected ellipse is first shrunk and then inflated outwards. The boundary is iteratively updated by a direction vector which is determined by internal and external energy terms (see Figure 10(a) and (b)). The internal energy term regulates the smoothness of the boundary whereas the external energy term fits the model to the object relying on double ridges which are perpendicular to the direction vector. Snake-based extraction methods are explained in detail in *Section 3.1.6*. The active contour model supplies a set of points indicating the boundary of each mitochondrion as depicted in Figure 10(c). The model may produce an incorrect boundary due to false positive or false negative detection of double membrane. In the final step, the boundary is refined by employing a modified live-wire algorithm [56] in which the boundary points of the balloon snakes are used as seed points. The live-wire algorithm is based on Dijkstra's
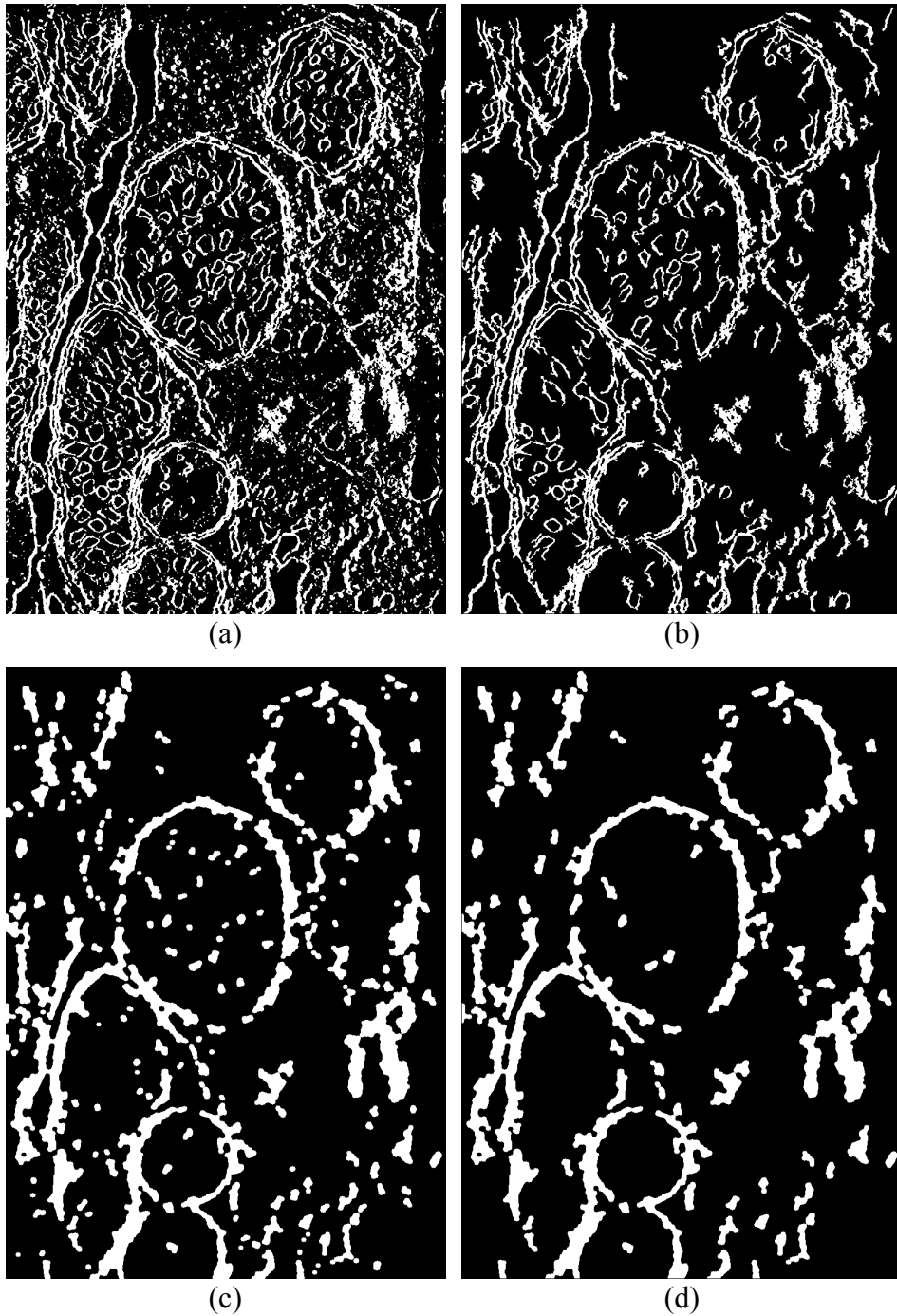
Figure 7: Images associated to the intermediate steps of morphological and connected component analysis after (a) thresholding; (b) the first connected component filtering; (c) morphological closing followed by opening and (d) the second connected component filtering (template image).
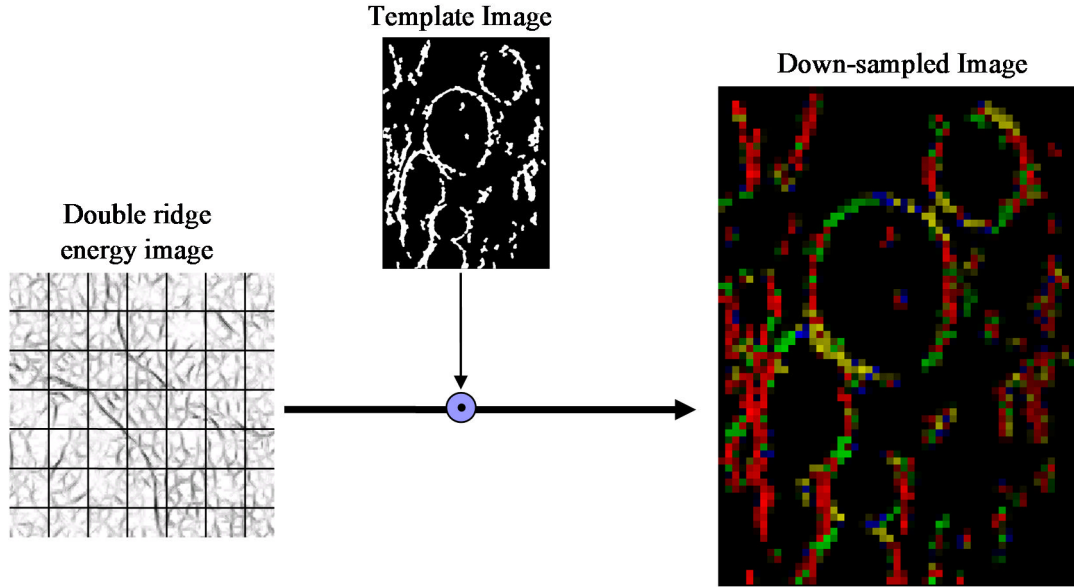
Figure 8: The down-sapling process in which the double ridge energy image is multiplied by template image and separated into blocks where the total double ridge energy for each direction is computed.

graph-searching algorithm [57] and used to find an optimal path between two seed points on the image. In order to operate the live-wire algorithm, a local cost function that determines the cost between neighboring pixels is required. In the proposed system, the local cost function relies on a linear combination of the template and double ridge energy images. An automatic seed point selection algorithm is additionally employed. The algorithm starts with the strongest seed point and finds another seed point that maximizes the ratio of total cost of the path (extracted by live-wire) to the squared length of the path. Then, this operation is repeated for remaining seed points that are not covered by the current path until no seed point is remained. Such a treatment tends to select the farthest seed point that provides an optimal contour encircling the boundary of the mitochondrion and passing between the inner and outer membranes.

2.2. Results and Discussion

Preliminary study includes three evaluation categories for the detection and segmentation algorithms applied on four TEM tomograms depicted in Figure 5:
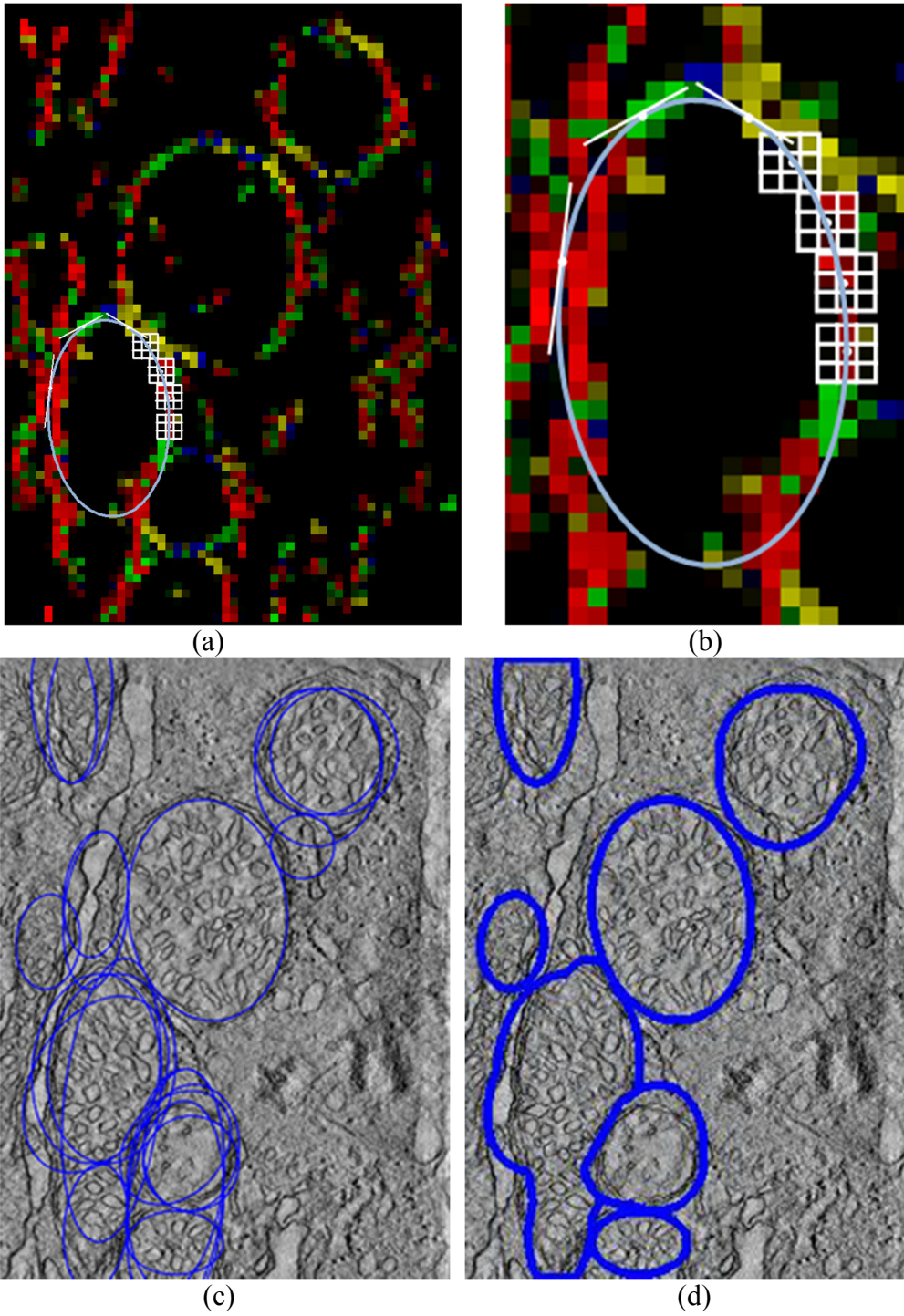
Figure 9: (a) Down-sampled double ridge energy image; (b) evaluation of a candidate ellipse; (c) extracted ellipses and (d) detected mitochondria after merging and separation of ellipses.
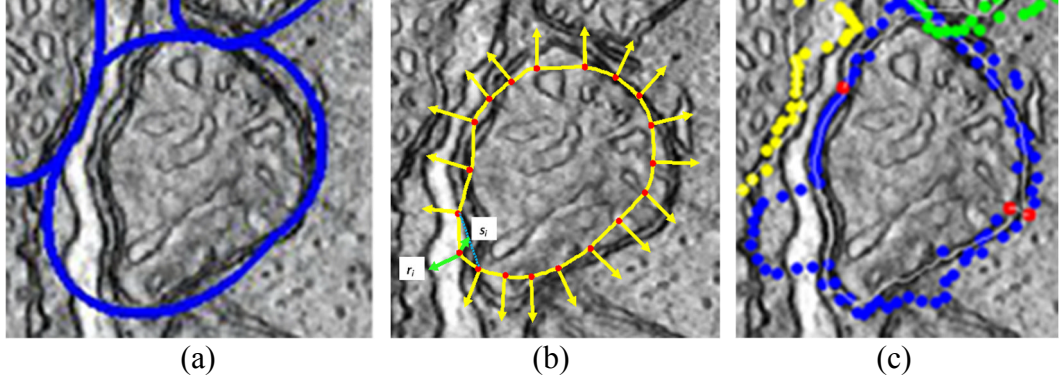
Figure 10: (a) The boundary of a detected mitochondrion; (b) direction vectors inflating the active contour model; (c) snake boundary (blue/red dots), used seed points (red dots), live-wire output (white).

i. **Evaluating ellipse detection:** The detected ellipse is considered a true positive detection if at least 70% of the area of the detected ellipse is part of a single mitochondrion, otherwise it is assumed as a false positive. A false positive detection happens when a significant part of the region is not inside a single mitochondrion. Experimental analysis exhibits an extraction of 52 ellipses of which 42 is true and 10 is false detections (i.e. ~80% precision).

ii. **Evaluating mitochondria detection:** The method achieves a successful detection of 14 out of 15 fully seen mitochondria and four out of seven partially seen mitochondria after a manual elimination process of false positive ellipses.

iii. **Evaluating segmentation performance:** The segmentation performance is exposed by the measurement of two metrics: Dice similarity coefficient (DSC) and median symmetric boundary error (MSBE). Experimental results reveals a DSC value of 91% and MSBE of 4.9 nm on average when compared with a trained reader. The measurement metrics are described in detail in *Section 4.2*.

Experiments show that the live-wire algorithm utilizes only a few seed points in order to achieve a successful segmentation. Although the system produces the seed points automatically (after the manual elimination of ellipses), it additionally supports an easy and fast manual segmentation of mitochondria. The user is allowed to specify the seed points through an interactive segmentation. In live-wire segmentation process, the algorithm is initiated with a seed point supplied by the user. Then, the user specifies another seed point by observing the contour drawn to the previous seed point in real-time. The procedure is repeated until the entire boundary is extracted.

The features provided by the double ridge detector is also useful for segmentation of the inner and outer membranes. The local separation, direction and thickness of inner
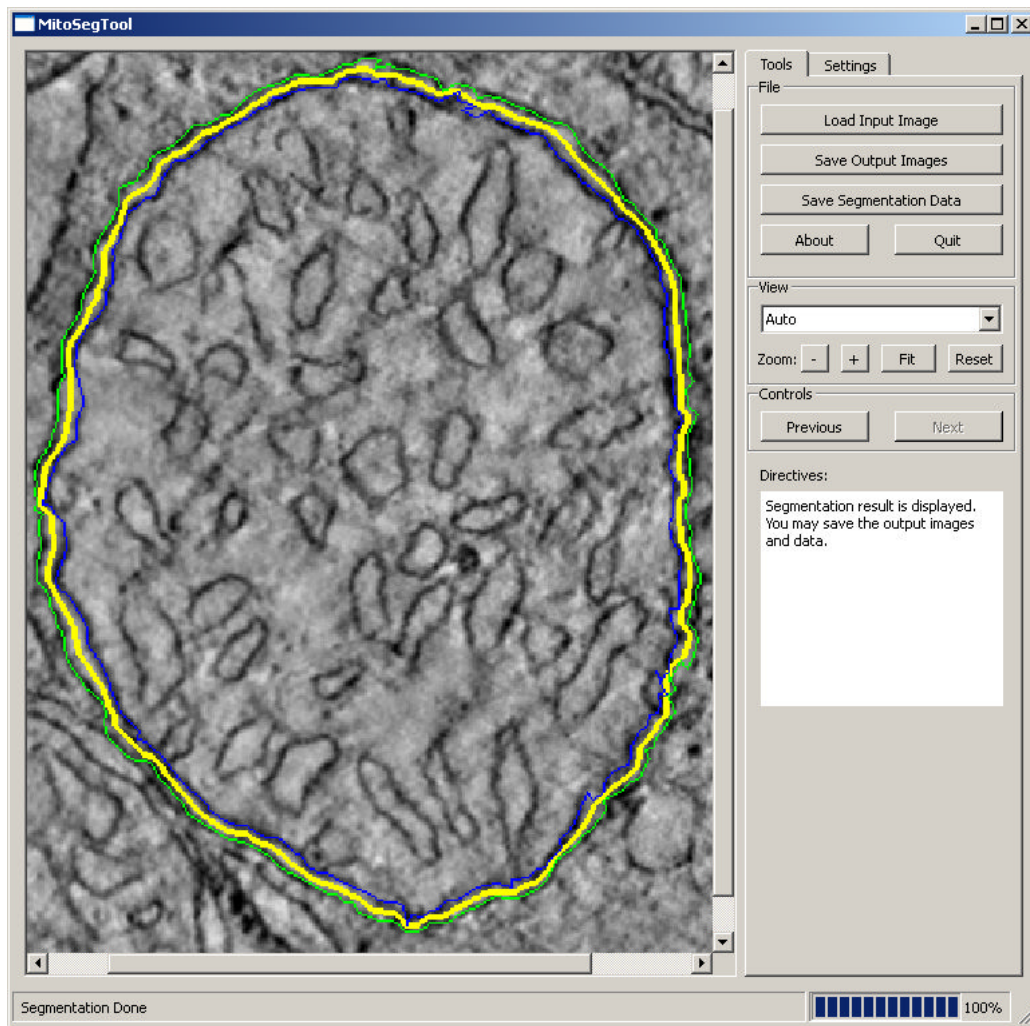
Figure 11: A snapshot from the mitochondrion segmentation tool showing extracted mitochondrial boundary (yellow: livewire output, blue and green: inner and outer membranes indicated by the double ridge detector.

and outer membranes directly locates the peripheral membranes. The preliminary study covers the implementation of a mitochondrion segmentation tool with a graphical interface that lets the user change the input parameters and run the detection and segmentation algorithms. Figure 11 illustrates a snapshot of the program in which a sample run providing the segmentation of both peripheral membranes is shown. The tool supports manual segmentation in addition. The segmentation data can be stored in various image formats or in text files containing pixel locations of the extracted contour.

The detection and segmentation accuracy achieved in this preliminary study substantially depends on the successful detection of double membranes and removal of cristae. In many cases, cristae structures are locally very similar to double

18

membranes so that the elimination of such cristae by morphological and connect component analysis is not successful. Discontinuities in peripheral membranes and ineffectively performed cristae elimination in the feature extraction step arise a major problem in the ellipse detection process since the candidate ellipses are evaluated based on the integral of a local descriptor over the boundary and the internal region of the ellipse.

Ellipse detection is not convenient for detection of mitochondria which have a significantly distorted elliptical shape. In such cases, candidate ellipses are assigned to a low score due to a large amount of gap. Another remarkable problem arises due to lack of double membrane detection since it is an essential feature for both detection and segmentation. In low resolution images, the separation between inner and outer peripheral membranes may not be clear or a mitochondrion does not exhibit a double membrane pattern in rare cases.

The observation realized in the preliminary study point to the following evidences:

- The features relying on a local intensity distribution usually causes misleading interpretations.
- Ellipse-based model does not suitably fit to the whole mitochondrion in distorted cases.
- Mitochondria can be represented by the unification of multiple morphological models.
- Semi-automatic tools are useful to achieve fast and accurate segmentation of mitochondria.

Further information is available for this preliminary study in a publication by Mumcuoglu et al. [52]. The next chapter describes the proposed work of the thesis in which those evidences have been taken into consideration in order to accomplish the detection and segmentation of mitochondria from more challenging TEM datasets.

CHAPTER 3

PROPOSED WORK

This section describes a novel detection and segmentation approach based on a validated active contour method which is driven by a parabolic arc model [53], [58]. In *Section 3.1*, the methods developed for the detection and segmentation in two dimension are presented. The extension of 2D algorithms to three dimensions are provided in *Section 3.2*.

3.1. Detection and Segmentation in Two Dimensions

The proposed method for detection and segmentation of mitochondria is composed of preprocessing, ridge detection, energy mapping, curve fitting and filtering, snake-based shape extraction, validation and post-processing steps. Figure 12 illustrates a flowchart of the algorithm and sample images related to the output of intermediate steps. The proposed 2D method is described by the following subsections.

3.1.1. Preprocessing

The preprocessing step removes the potential effect of weak membrane strength and contrast problems of the input image on the output of other steps. Noise of TEM images are additionally handled in this step. Moreover, difficulty in parameter tuning process which is originating from the pixel size differences of the datasets is dissipated. Figure 12(a) and Figure 12(b) show a sample image before and after processing respectively. The preprocessing step comprises three parts as described below:

i. **Auto-contrast adjustment:** Extreme values may be contained in reconstructed EMT images due to artifacts caused by the utilized gold markers or X-rays and charge-coupled device (CCD) camera flaws. The contrast is skewed by those extreme low or high values. The image contrast is substantially degraded by the normalization of gray values in such datasets. Assuming that the distribution in gray values has some extreme points, gray values of pixels in the image are re-normalized into a certain range (such as 0-1 or 0-255) by auto-contrast adjustment. A small fraction (e.g. 0.5%) from the lowest and highest gray values in the histogram are set to the minimum and the maximum gray value (i.e. 0 and 255) respectively. Auto-contrast adjustment step realizes the normalization by scaling the other pixel values linearly among
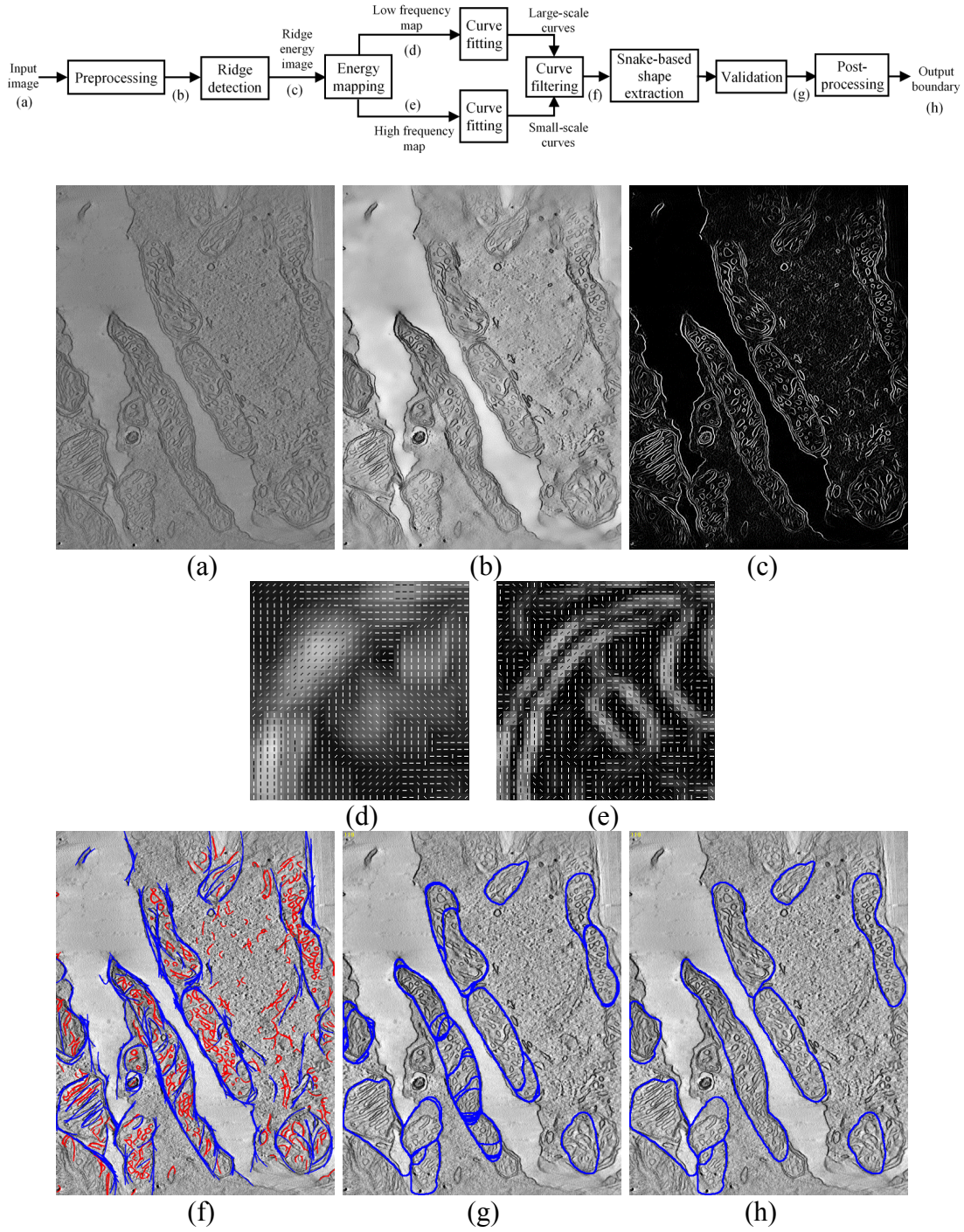
Figure 12: Flowchart of the mitochondria detection and segmentation algorithm (top) and sample images (a-g) showing the output of intermediate steps: (a) Input image; (b) Preprocessed and (c) Ridge energy image; (d) Low frequency ridge energy map (LFREM) image and (e) High frequency ridge energy map (HFREM) image for the region indicated by the red square shown in (c); (f) Detected curves after filtering (blue: large-scale curves, red: small-scale curves); (g) Validated snake output; (h) Output boundary after post-processing. Reprinted from [58].
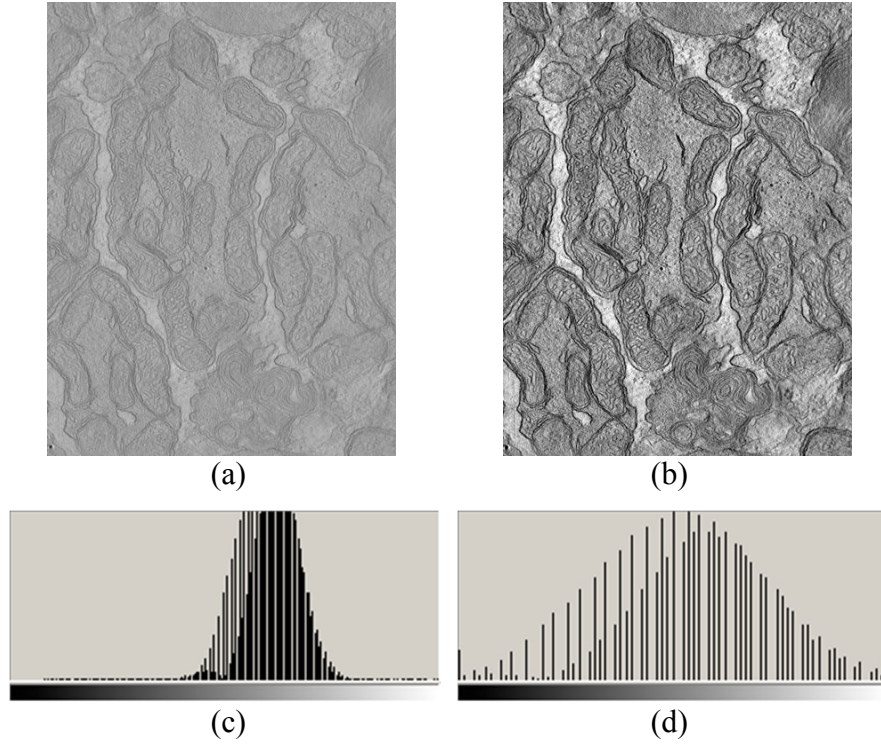
Figure 13: (a) An original TEM tomography image; (b) Auto-contrast adjusted image; (c) Histogram of original image shown in (a) and (d) Histogram of the auto-contrast adjusted image shown in (b).

these maximum and minimum values. A sample TEM tomogram and the corresponding auto-contrast adjusted image are shown in Figure 13(a) and (b) respectively. The histograms of the original and processed images are illustrated in Figure 13 (c) and (d).

ii. **Resampling:** In this step, a resampled image with a fixed pixel size is obtained by interpolation in order to ease the parameter tuning. Interpolation of the image to 2 nm pixel size does not produce data loss issues on mitochondrial membranes as justified in the preliminary study since the membrane thickness in a typical mitochondria is in the range of 4–6 nm [9], [52].

iii. **Smoothing:** Bilateral filtering [31] is recommended smoothing technique for electron microscopy since it is an edge-preserving filtering method which is applied as a noise removing procedure [27], [34]. In bilateral filtering, the contribution of each pixel depends on both the spatial proximity and differences in the gray values of pixels in a neighborhood as formulated below:

$$I_f(x) = \int I(p) G_r(|I(p) - I(x)|) G_s(\|p - x\|) dp \qquad \text{(Equation 1)}$$

23
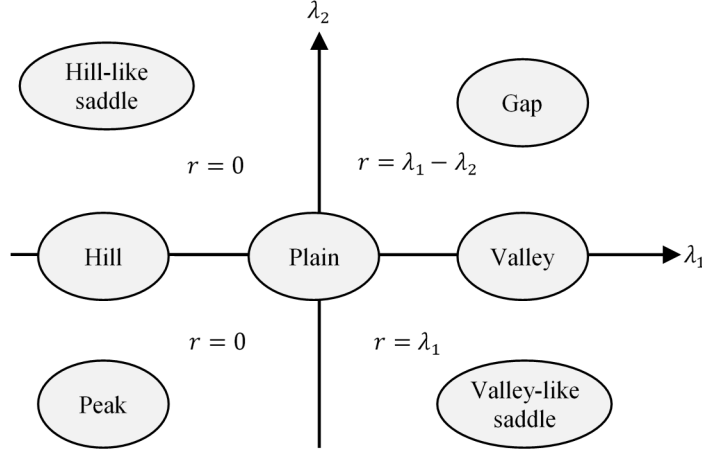
Figure 14: Topographic shapes to be detected with respect to eigenvalues of Hessian matrix and assigned ridge energy. Reprinted from [58].

where I and I_f denote the input and the filtered image; the terms G_r and G_s are the weights of gray value differences and spatial proximity respectively. These weights are usually chosen as a Gaussian distribution with zero mean:

$$G(x) = \frac{1}{\sigma\sqrt{2\pi}}e^{-\frac{x^2}{2\sigma^2}}$$
(Equation 2)

where σ parameter controls the amount of contribution of each neighboring pixel with respect to the distance to the smoothed pixel (for G_r) and the difference in gray value (for G_s). The effects of the noise and the non-membrane-like structures are reduced whereas membranes are preserved by this technique.

3.1.2. Ridge Detection

The ridge detection step extracts membrane-like structures. Membranes reside at the locations where intensity increases in opposite directions and remains constant in tangential direction since membrane profile shows bright-dark-bright transition. A Hessian-based ridge detector which is sensitive to valley-like shapes is constructed and applied to the preprocessed image in order to detect membranes. Let λ_1 and λ_2 be eigenvalues of Hessian matrix defined as:

$$H = \begin{bmatrix} G_{xx} & G_{xy} \\ G_{yx} & G_{yy} \end{bmatrix}$$
(Equation 3)

where the eigenvalues satisfy $|\lambda_1| \geq |\lambda_2|$ and G_{xx}, G_{yy}, G_{xy} and G_{yx} are the second order Gaussian derivatives of the image with respect to the axis indicated by the

24

subscript. As illustrated in Figure 14, a valley is obtained at a location where $\lambda_1 \gg |\lambda_2|$. When $\lambda_1 \approx \lambda_2 \gg 0$ on the other hand, it turns into a gap (i.e. a dark blob-like object) as in the first quadrant of the coordinate system in Figure 14. A saddle point on a valley which is interpreted as a relatively weak point on a membrane is obtained in the fourth quadrant when $\lambda_1 \gg 0$ and $\lambda_2 \ll 0$. Considering membranes have some discontinuities, the ridge energy is defined as:

$$r(\lambda_1, \lambda_2) = \begin{cases} \lambda_1 - \lambda_2 & \text{if } \lambda_1 > 0 \text{ and } \lambda_2 > 0 \\ \lambda_1 & \text{if } \lambda_1 > 0 \text{ and } \lambda_2 < 0 \\ 0 & \text{otherwise} \end{cases} \qquad \text{(Equation 4)}$$

According to Equation 4, the ridge energy depends on the difference between λ_1 and λ_2 when both eigenvalues are positive. A discontinuity or a weak point exists on the membrane when λ_2 is negative and the ridge energy depends on only the first eigenvalue (λ_1) which indicates the depth of valley. Hence, it detects objects which are in the shape of elongated dark stripes. Since hill-like (i.e. bright) structures are not in interest, the ridge energy is equal to zero in the second and third quadrants. Figure 12(c) illustrates a sample ridge image where bright pixels indicate high ridge energy where peripheral and crista membranes are located. Additionally, the second eigenvector provides the ridge direction which is normal to the membrane.

3.1.3. Energy Mapping

Although the ridge strength formulation detects membrane-like structures, it only stores local information and is not capable of classifying peripheral and cristae membranes of mitochondria. Therefore, a ridge energy map which carries features associated to the "*big picture*" [58] is constituted assuming that peripheral membranes of mitochondria are longer and have relatively low curvature in most cases.

The ridge image is scanned within a sliding window with a size ω in order to analyze distribution of ridge intensity over a large region instead of relying on local information. To increase computation efficiency and supply smoothness to ridge points having extreme curvature, the ridge direction is binned to four angles such that the intervals $(-\pi/8, \pi/8)$ and $(7\pi/8, 9\pi/8)$ correspond to 0; $(\pi/8, 3\pi/8)$ and $(-5\pi/8, -7\pi/8)$ correspond to $\pi/4$; $(3\pi/8, 5\pi/8)$ and $(-3\pi/8, -5\pi/8)$ correspond to $\pi/2$ and finally the intervals $(5\pi/8, 7\pi/8)$ and $(-\pi/8, -3\pi/8)$ correspond to $3\pi/4$. The total ridge energy is given by the summation of ridge energy of the points within the window having the same ridge angle. This total energy is computed for all four angles individually. The window is passed over the entire image to obtain an energy map $e_\theta(s)$ that accumulates the total ridge energy for the angle θ around the point s.

Figure 12(d) and (e) show sample ridge energy map images for the same portion of the ridge image by setting the window size ω to 30 nm and 8 nm respectively. The major
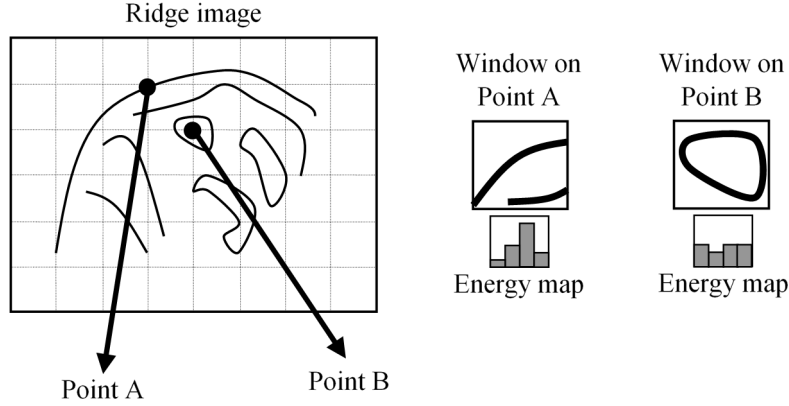
Figure 15: Sample points A and B on the ridge image (left); corresponding windows placed on A and B (right); energy maps ($e_\theta(A)$ and $e_\theta(B)$) (bottom-right). Each point on the energy map corresponds to a histogram indicating the total ridge energy with respect to each ridge angle within the window. Reprinted from [58].

direction (having the highest energy) is indicated by dashes. High frequency information (subtle detail) is obtained by using a small value of ω whereas low frequency information (rough detail) are supplied by a large value of ω. The detail of both cristae and mitochondrion boundary is preserved in the high frequency ridge energy map (HFREM) (see Figure 12(e)). On the other hand, cristae detail is mostly filtered because of the large window used in the low frequency ridge energy map (LFREM) (see Figure 12(d)). However, LFREM preserves mitochondrial boundary on the contrary. These two cases are depicted in Figure 15 by sampling two points to demonstrate the energy map histogram. In LFREM, the histogram is expected to have more uniform distribution for crista structures compared to mitochondrion boundary.

3.1.4. Parabolic Arc Model

Composition of curve segments can be used to represent the peripheral and cristae membranes of mitochondria. In general, the peripheral membranes are composed of smooth and long curve segments whereas cristae are in forms of relatively short curves with higher curvature relative to peripheral membranes. Figure 16 delineates a 2D parabolic arc model utilized to detect membrane-like patterns by using the ridge energy maps, LFREM and HFREM. This model is denoted by two tip points (x_1, y_1), (x_2, y_2) and a sagitta length (height) h.

A parabolic arc having a chord length (width) R and a sagitta length h which pass through the origin of the kt-plane is given by:

$$k = at^2 + bt, \quad 0 \le t \le R \qquad \text{(Equation 5)}$$

26
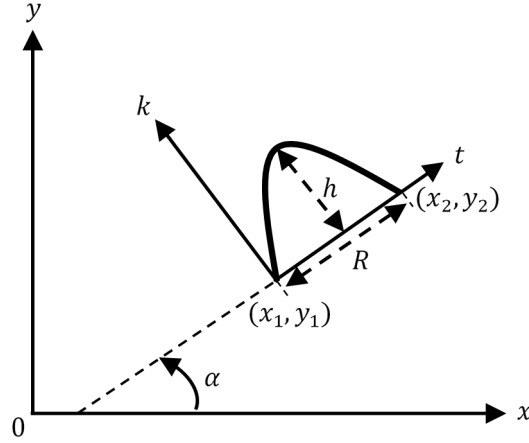
Figure 16: A parabolic arc model represented by two tip points (x_1, y_1), (x_2, y_2) and height h. Reprinted from [58].

where $b = \frac{4h}{R}$, $a = -\frac{b}{R}$ and $R = \sqrt{\Delta x^2 + \Delta y^2}$ with

$$\Delta x = x_2 - x_1 \qquad \text{(Equation 6)}$$

and

$$\Delta y = y_2 - y_1 \qquad \text{(Equation 7)}$$

Then, a point s on the rotated parabolic arc in xy-plane is given by:

$$s = \begin{bmatrix} x \\ y \end{bmatrix} = \begin{bmatrix} \cos\alpha & -\sin\alpha \\ \sin\alpha & \cos\alpha \end{bmatrix} \begin{bmatrix} t \\ k \end{bmatrix} + \begin{bmatrix} x_1 \\ y_1 \end{bmatrix} \qquad \text{(Equation 8)}$$

where $\cos\alpha = \frac{\Delta x}{R}$ and $\sin\alpha = \frac{\Delta y}{R}$. The tangential angle φ_s of the parabola on the point s is approximated as:

$$\varphi_s = \arctan\frac{y(t - \Delta t) - y(t + \Delta t)}{x(t - \Delta t) - x(t + \Delta t)} \qquad \text{(Equation 9)}$$

where the step size on the t-axis is specified by Δt that can be adjusted to locate the equidistant points on the parabolic arc. A smoother curve is obtained by a smaller step size by acceding the increase in computation time. A dynamic step size is used to achieve the identical smoothness for arcs with different scale (see Appendix A):

$$\Delta t = \frac{S}{\sqrt{1 + (2at + b)^2}} \qquad \text{(Equation 10)}$$

27

where S denotes the distance between each neighboring point on the arc (e.g. 1 pixel size). Additionally, a scale invariant curvature measurement for the parabolic arc model is defined as:

$$\kappa = \frac{|h|}{R} \qquad \text{(Equation 11)}$$

The next section describes the curve fitting algorithm developed for the parabolic arc model.

3.1.5. Curve Fitting and Filtering

The curve fitting step involves the extraction of membrane-like structures by utilizing ridge energy maps (LFREM and HFREM) and the parabolic arc model explained in the previous sections. The energy function of the curve segment is given by:

$$E(\Omega) = \sum_{s \in \Omega} \sum_{\theta} w(\varphi_s, \theta) e_\theta(s) \qquad \text{(Equation 12)}$$

where Ω denotes the set of points on the curve segment generated by Equation 8. The tangential angle of the curve at the point s is represented by φ_s (see Figure 17(a)). The term w is the weight function defined as:

$$w(\phi_1, \phi_2) = \cos\big(2(\phi_1 - \phi_2)\big) \qquad \text{(Equation 13)}$$

Equation 12 involves a weight coefficient that controls the contribution of the energy on the point s by considering difference in tangential angle of the curve (φ_s) and the ridge direction (θ). The maximum contribution is allowed if these two angles are similar (i.e. if the difference between φ_s and θ is close to zero) since the weight coefficient is close to one. If the angles are different (i.e. the difference is close to $\pm\pi/2$), it gets closer to minus one and provides a negative contribution. Hence, the parabolic arc is expected to pass through points where strong ridges with suitable angles are available in order to accumulate high energy. This framework enforces the maximization of the curve energy. Hence, an iterative curve fitting algorithm is employed in which the parabolic arcs are initialized as single points on local maxima of the ridge energy maps having the total ridge energy for the major direction is adequately high (i.e. $\max_\theta e_\theta(s) > T_{\text{map}}$ where T_{map} is a threshold).

The curve fitting algorithm [58] is described below:

I. **Initialization:** Initialize a parabolic arc as a single point s on each local maximum point of $\max_\theta e_\theta(s)$ (as illustrated in Figure 17(b)) that satisfies $\max_\theta e_\theta(s) > T_{\text{map}}$ such that $(x_1, y_1) = (x_2, y_2) = s$; $h = 0$.

28
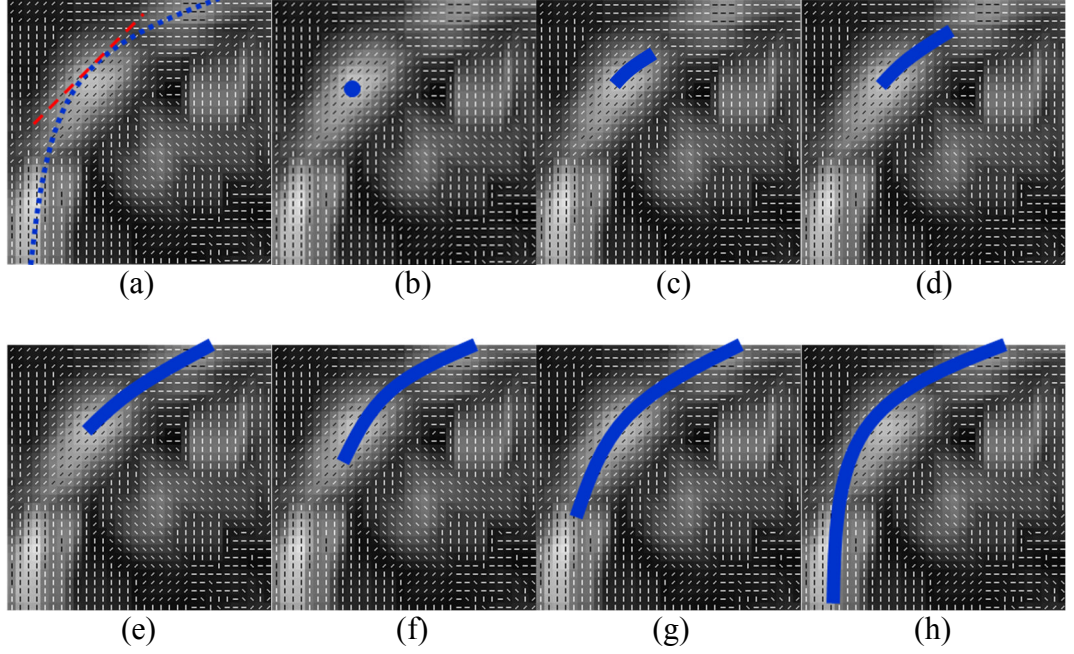
Figure 17: The energy map $(e_\theta(s))$ and growing curve: (a) a parabolic arc (blue) and the tangent line (red); (b) the curve fitting algorithm initialized by a point on a local maximum; (c-e) the first growing phase; (f-h) the second growing phase.

II.   **Growing phase 1:** Figure 17(c-e) depicts the growing phase which is summarized below:

    i.   Let $\left(x_1^{(0)}, y_1^{(0)}\right) = (x_1, y_1)$; $h^{(0)} = h$ and $i = 0$.

    ii.   Compute $E(\Omega)$ for each parameter set candidate by using Equation 12:

$$\left(x_1^{(i+1)}, y_1^{(i+1)}\right) \in \left\{x \middle| x_1^{(i)} - \tau_x \le x \le x_1^{(i)} + \tau_x\right\}$$
$$\times \left\{y \middle| y_1^{(i)} - \tau_y \le y \le y_1^{(i)} + \tau_y\right\}$$

and height $h^{(i+1)} \in \left\{a \middle| h^{(i)} - \tau_h \le a \le h^{(i)} + \tau_h\right\}$ where the set of curve points Ω is generated by using Equation 8 for the current values of parameters $(x_1^{(i+1)}, y_1^{(i+1)}, x_2, y_2, h^{(i+1)})$ and $t = 0, \Delta t, 2\Delta t, 3\Delta t, \dots, R$. Select the parameter set which maximizes $E(\Omega)$.

    iii. If $\left(x_1^{(i)}, y_1^{(i)}, h^{(i)}\right) \ne \left(x_1^{(i+1)}, y_1^{(i+1)}, h^{(i+1)}\right)$, increment i and go to step ii.

    iv. Set $(x_1, y_1) = \left(x_1^{(i)}, y_1^{(i)}\right)$ and $h = h^{(i)}$.

III.   **Growing phase 2:** Repeat the first growing phase by changing the parameters (x_2, y_2, h) and keeping (x_1, y_1) fixed (see Figure 17(f-h)).

The terms τ_x, τ_y and τ_h are the update parameters which specify the size of searching region at each iteration and adjust growing speed. Model parameters (x_1, y_1), (x_2, y_2) and h are evolved within the interval determined by the update parameters to maximize the curve energy iteratively.
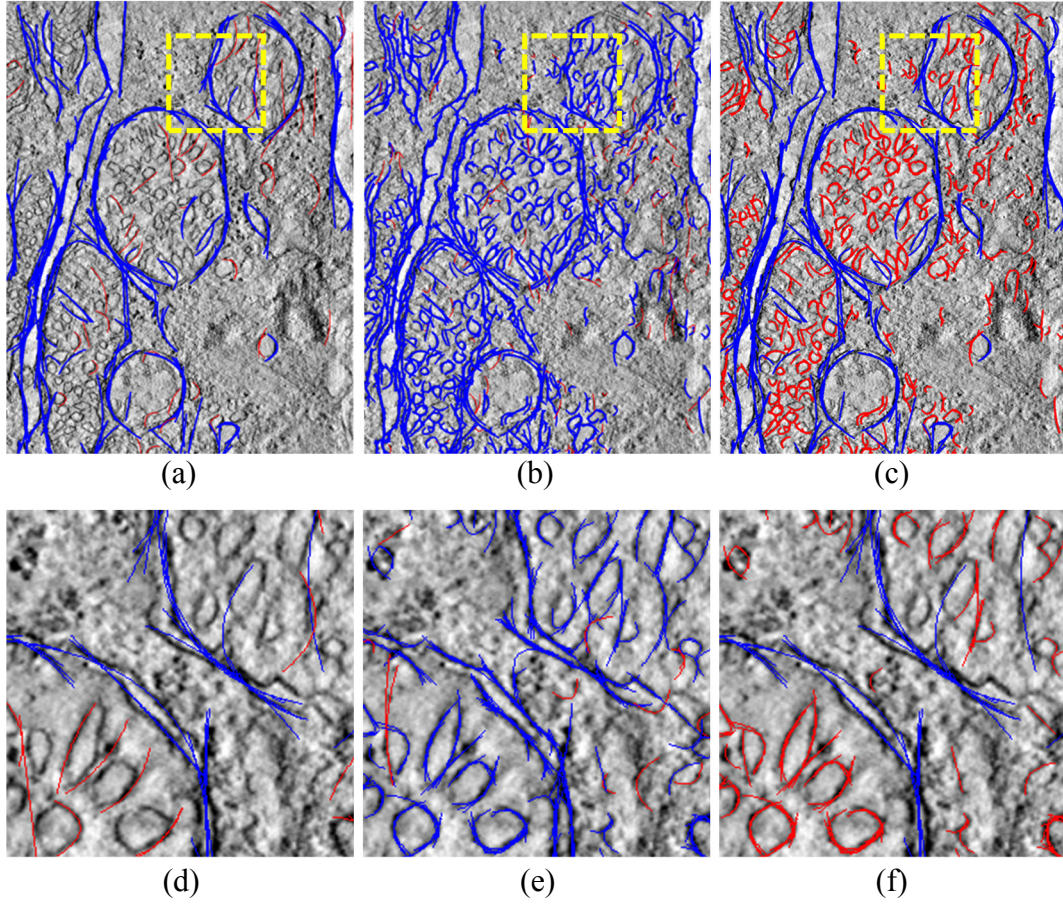
Figure 18: Curve segments obtained by using low frequency energy map (a); high frequency energy map (b) and filtered curves (c). In (a) and (b), blue curves show successful detections and red curves are eliminated curves due to weakness and shortness. In (c), blue and red curves show the accepted detections in (a) and the obtained curves from (b) respectively after the elimination and filtering process are applied; (d), (e) and (f) are close-up images taken from the yellow region placed on (a), (b) and (c) respectively. Reprinted from [58].

The curve fitting algorithm described above is repeated for two different adjustment of window size ω utilized in the energy mapping step. Therefore, two different sets of parabolic arc are extracted. The extracted arcs are shown in blue in Figure 18(a) and (b) by utilizing LFREM ($\omega = 30$ nm) and HFREM ($\omega = 8$ nm) respectively. Generally, HFREM provides shorter curve segments since a parabolic arc cannot suitably fit in large-scales to HFREM. They are called "*small-scale curves*" [58] throughout this work. These small-scale curves can be acquired on all membrane-like structures (peripheral membrane, cristae, etc.). On the other hand, LFREM provides longer parabolic arcs which have relatively high energy. The curves mostly appear on the mitochondrion boundary and endoplasmic reticulum when LFREM is used and they are called "*large-scale curves*" [58].

Unreliable curves are considered as false detections and thus removed in the subsequent filtering step. Parabolic arcs with an excessive height can be detected although the curve does not reasonably fit into the membrane of mitochondria. Therefore, a curve is removed if the curvature is unexpectedly high (i.e. $\kappa > 1$ which implies $|h| > R$ such that a sharp bend occurs at the sagitta point of the parabola). The parabolic arc initialized at irrelevant locations (e.g. cytoplasm) are not expected to grow and gather high energy ($E(\Omega)$). Therefore, the arcs that are not sufficiently long and strong are also removed. In this filtering step, the large- and small- scale curves having an arc-length shorter than 100 nm and 20 nm respectively or having an average curve energy less than 30% of the maximum of the energy map were eliminated in the conducted experiments presented in *Chapter 4*. The eliminated curves are delineated in red in Figure 18(a) and (b).

Figure 18(b)) clearly indicates that the set of points on small-scale curves covers the set of points on large-scale curves (Figure 18(a)). As a final process in the curve filtering step, both curve sets are combined on a single image by eliminating small-scale curves which overlaps a large-scale curve. A large-scale curve is overlapped by a small-scale curve if 70% of the latter resides within ω neighborhood of the former (here ω is the window size used for curve fitting on LFREM).

Figure 18(c) and Figure 12(f) illustrates large-scale curves as blue curves which were extracted from LFREM. These curves are mostly extracted on mitochondrial boundary of long membrane-like structures. The curve segments in red are the detected curves in only HFREM and generally extracted on small scale membrane-like structures such as cristae.

3.1.6. Snake-Based Shape Extraction

Employing only a curve fitting process is not sufficient for mitochondria segmentation since membranes may not seem to fully surround the mitochondria. Moreover, a weakness in the appearance of membrane may lead to a failure in curve fitting process due to insufficient ridge detection. Multiple mitochondria located close to each other may be overlapped by a single curve segment. Therefore, further processing is necessary to separate mitochondrial regions considering that mitochondria are polymorphic.

To deal with the segmentation difficulties in this problem, a variant of the active contour model called the balloon snake method is utilized. Active contour models render possible the segmentation of irregular shapes and are able to compensate boundary discontinuities [59]. An additional inflation property is integrated in balloon snakes in order to start segmentation by approaching from the internal region of the object. The balloon snakes show a remarkable stability when they are initialized far from contours in a plain region [55].

The snake model is evolved by the minimization of snake energy formulated as:

$$E_{\text{snake}}(v) = \int \left(E_{\text{int}}(v) + E_{\text{ext}}(v) + E_{\text{inf}}(v) \right) dt \qquad \text{(Equation 14)}$$

where v denotes the boundary of the object (i.e. mitochondrion) to be segmented that is represented by x and y coordinates of the snake contour along a trajectory t. E_{int} is a smoothness term that consists of the first and second order derivatives of v:

$$E_{\text{int}} = \frac{1}{2}\left(w_a \left\| \frac{dv}{dt} \right\|^2 + w_b \left\| \frac{d^2v}{dt^2} \right\|^2 \right) \qquad \text{(Equation 15)}$$

where w_a and w_b are the weight parameters which control the tension and the curvature on the contour generated by the first derivative and the second derivative respectively. The external energy term E_{ext} pulls the snake boundary towards the desired contour and an inflation force is created outwards by E_{inf}. In the proposed snake-based shape extraction approach, boundary of the snake is controlled by a curve energy image which is formed by a curve energy function $E(\Omega)$ based on average curve energy:

$$E_{\text{curve}}(x, p) = \begin{cases} \dfrac{E(\Omega_p)}{|\Omega_p|} & \text{if } x \in \Omega_p \\ 0 & \text{otherwise} \end{cases} \qquad \text{(Equation 16)}$$

where p is a large-scale curve segment, Ω_p is the set of points on p and x is a point on the image. The cardinality term $|\Omega_p|$ is equal to the number of points on p. Then, the external energy term E_{ext} is given by the summation of curve energy images:

$$E_{\text{ext}}(x) = -w_c \sum_{p \in C_L} E_{\text{curve}}(x, p) \qquad \text{(Equation 17)}$$

where w_c regulates how much the snake contour is affected by curves and C_L is the set of large-scale curves. Since the snake is converged by the minimization of energy, the negative valued energy function is presented in Equation 17. Hence, the boundary should evolve towards the curve points. Moreover, overlapping curve segments form a stronger contour since the energy is based on accumulation of all detected curves.

The minimization of the snake energy (Equation 14) is carried out iteratively by altering the snake contour until it is converged. The snake is initialized near to the vertex of a parabola as a unit circle. The initialization process of snakes is discussed in detail in *Section 3.2.2.* The snake contour is updated by the equation defined as:

$$v_{i+1} = v_i - \gamma \nabla E_{\text{snake}}(v_i) \qquad \text{(Equation 18)}$$

where γ is step size and generally set to a dynamic value (i.e. $1/|\nabla E_{snake}|$) in order to provide a feasible speed to the snake to catch the mitochondrion boundary. The neighboring points on the snake contour may align unequally during evolution of snake due to the vector field created by $\nabla E_{snake}(v_i)$. In order to solve this problem, an equidistant correction mechanism is employed in addition to the presented model [60]. The term ∇E_{snake} is given by:

$$\nabla E_{snake} = \nabla E_{int} + \nabla E_{ext} + \nabla E_{inf} \qquad \text{(Equation 19)}$$

where the internal energy update term ∇E_{int} is given by (see Appendix B):

$$\nabla E_{int}(v) = -w_a \frac{\partial^2 v}{\partial t^2} + w_b \frac{\partial^4 v}{\partial t^4} \qquad \text{(Equation 20)}$$

Five neighboring points on the snake boundary are used to compute Equation 20 numerically. On the other hand, the term ∇E_{ext} is obtained by the derivative of the image provided by E_{ext} with respect to the x and y axes individually. The gradients of internal and external energy terms are the forces that move the snake contour towards the object to be segmented and can be thought as inversely oriented vectors. Accordingly, ∇E_{inf} is constructed as the negatively weighted outwards normal vector:

$$\nabla E_{inf}(v) = -w_d \vec{N}_v \qquad \text{(Equation 21)}$$

where $\vec{N}_v$ is the unit normal vector at the snake boundary v and w_d controls the strength of the inflation. This creates a force pulling the boundary outwards and prevents the boundary from shrinking in case of weak external forces. Therefore, the snake boundary will inflate when it is placed on a plain region far from curves. Besides, after the boundary grows a while, the forces regarding the internal and inflation energy will cancel out each other and the snake will stop growing since the internal force is increased. The snake is enforced to grow by using a strong inflation force when internal and external forces acting on the snake are weaker. In this respect, convergence of the snake depends on the size of the region and the strength of curves around the region. In order to segment a small mitochondrion, a small value of w_d is adequate. A higher value of w_d is necessary in case of a larger mitochondrion. If w_d is too high, the boundary of the mitochondrion may not stop inflation of the snake due to presence of weak curves. On the other hand, considering the potential false-positive detections of large-scale curves on cristae, w_d should be set to a high value.

The following algorithm is designed to extract candidate regions considering different boundary strength, cristae detections and mitochondrion size.
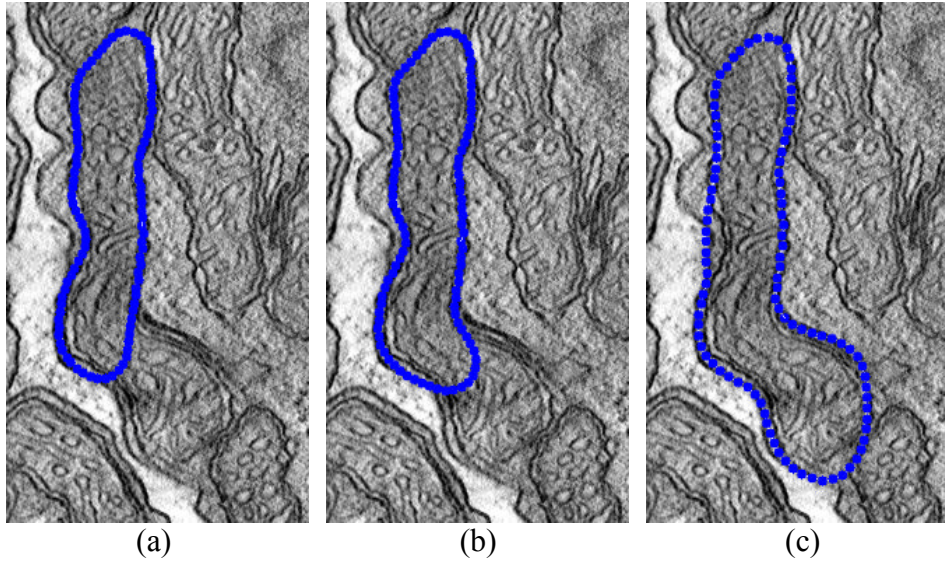
Figure 19: Sample output of the shape extraction algorithm: (a) 1st iteration; (b) 2nd iteration and (c) 3rd iteration. Reprinted from [58].

For each curve segment, repeat the following steps:

i. Set w_d to a small value.
ii. Initialize the snake as a unit circle near to a curve segment.
iii. Run the snake algorithm.
iv. If the obtained boundary is different, save the snake boundary v_i.
v. Increase w_d.
vi. If w_d is less than a threshold (T_{inf}), go to step ii.

The snake boundaries are obtained iteratively by using ascending values of w_d by algorithm described above. A sample output of the algorithm for different iterations is depicted in Figure 19. The algorithm is executed for each curve segment located on different locations to scan the entire image. Since misleading snake initializations would occur due to false curve detections, weak parabolic arcs are ignored as stated in the preceding curve filtering step. A non-mitochondrial region may be extracted by this process if the snake is initialized outside a mitochondrion and the snake coincides curve segments that surround the snake. Therefore, validation procedure is employed in the subsequent step to discard irrelevant or awkward segmentations.

3.1.7. Validation

A mitochondrion is separated from the background by a surrounding membrane and presence of cristae structures inside. Although a particular shape cannot strictly represent the mitochondria, the most of mitochondria appear in the form of "distorted,
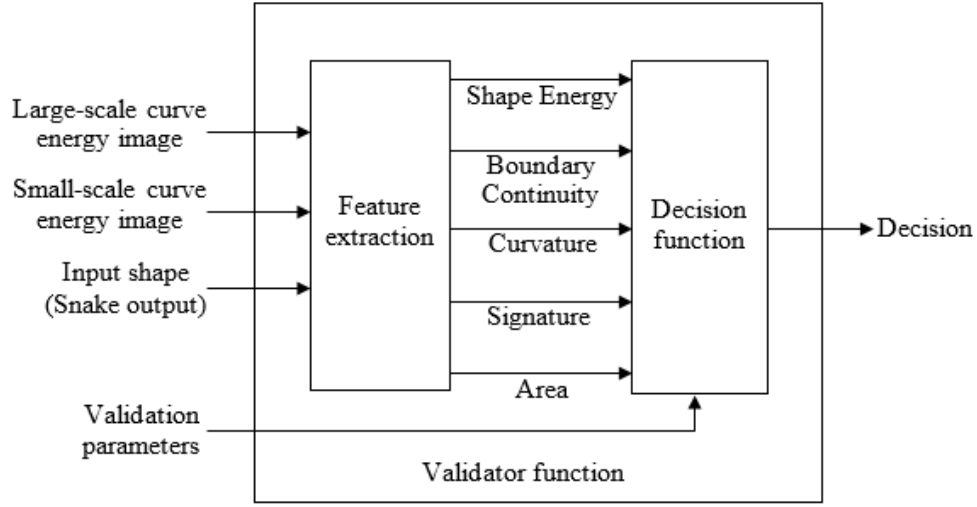
Figure 20: Internal structure of validator function.

bended or laterally compressed form of an ellipsoid" [53] (see Figure 21). Candidate shapes detected in the previous step are subjected to a validation process to filter out potential false positives. This validation scheme employs a binary valued validator function $F(v)$ that decides the acceptance or rejection of the shape v. The validator function verifies a set of descriptor-condition pairs as depicted in Figure 20. If all of the conditions are met, a decision is given towards acceptance of the shape v as a correct mitochondrial detection. The circumference and area of the candidate shape denoted by **C** and **A** respectively are utilized to ensure the scale-invariance property by normalizing quantities in the equations given in this section. The descriptors computed in $F(v)$ are described in five categories below:

i.   **Energy:** The presence of a mitochondrion is partially indicated by strong curves on the boundary and cristae inside the shape. The average boundary energy of the shape v is formulated as:

$$E_{\text{boundary}}(v) = \frac{1}{\mathbf{C}} \sum_t \sum_{p \in C_L} E_{\text{curve}}(v(t), p) \qquad \text{(Equation 22)}$$

where C_L is the set of the large-scale curves. The average energy which corresponds to internal region of the shape is calculated by arranging Equation 22 to work on the small-scale curves. Hence, the formulation of the average region energy is as follows:

$$E_{\text{crista}}(v) = \frac{1}{\mathbf{A}} \sum_{q \in S_v} \sum_{p \in C_S} E_{\text{curve}}(q, p) \qquad \text{(Equation 23)}$$

35

Note that S_v denotes the set of points inside the closed region constructed by v and C_S is the set of small-scale curves. Hence, the acceptance criteria pertaining to the shape energy comprises $E_{\text{boundary}} > T_{\text{energy\_b}}$ and $E_{\text{crista}} > T_{\text{energy\_c}}$ where right-hand side terms are the energy thresholds adjusted for boundary and crista respectively.

ii. **Area:** The area is utilized to specify if the size of the shape is within the acceptable limits. Hence, this quantity is expected to be in a range determined by the physical limitations. Note that the area of cross-sectional region of a mitochondrion may be close to zero depending on location and orientation of the cross-section. However, excessively small slices of mitochondria may not be dependable. Thus, the criterion for acceptance is defined as:

$T_{\text{area\_min}} < \text{A} < T_{\text{area\_max}}$.

iii. **Discontinuity:** The snake model has a gap compensating property that may cause incorrect segmentation such that boundary of the shape has significant portions with too weak boundary energy. For such cases, reliability of the shape must be checked. Since the cross-sectional region of a mitochondrion may appear as roughly closed, the candidate boundary is allowed to have a gap. Moreover, it may be seen partially on the image border. Nevertheless, the false positive rate would increase by allowing shapes with extreme gaps. Hence, a gap detection process is applied to filter the shape with respect to the gap length. A gap exists on the boundary point t if the boundary energy term $\sum_{p \in C_L} E_{\text{curve}}(t, p)$ is less than a threshold $T_{\text{gap\_energy}}$. The other gap descriptors are the total gap length ($L_{\text{gap\_total}}$), the maximum gap length ($L_{\text{gap\_max}}$), the ratio of $L_{\text{gap\_total}}$ to C ($L_{\text{gap\_ratio}}$) and the ratio of the total gap length on the image border to C ($L_{\text{gap\_border}}$). Thus, four acceptance criteria related to the continuity descriptors of boundary are determined by allowing an upper bound for each descriptor:

(1) $L_{\text{gap\_total}} < T_{\text{gap\_total}}$,
(2) $L_{\text{gap\_max}} < T_{\text{gap\_max}}$,
(3) $L_{\text{gap\_ratio}} < T_{\text{gap\_ratio}}$
(4) $L_{\text{gap\_border}} < T_{\text{gap\_border}}$.

Therefore, if one of the gap descriptors reveals an excessive discontinuity on the boundary, the shape is rejected.

iv. **Curvature:** A correct detection is expected to have a reasonably smooth shape boundary. Therefore, average and local curvature on the boundary is inspected in this category. A shape is accepted if the curvature is suitable for the contour of a mitochondrion. If the change in direction of the boundary path is frequent or sharp, then the shape is inadmissible. The local curvature is given by [61]:

$$\kappa = \left\| \frac{d\vec{T}}{dl} \right\| \qquad \text{(Equation 24)}$$

where $\vec{T}$ denotes the unit tangent vector and l is the arc length. The local curvature at a sample point of $v(t)$ in the discrete case can be approximated by utilizing the formulation below (see Appendix C):

$$\kappa_L(t) \cong \frac{2}{\|d(t)\| + \|d(t+1)\|} \left\| \frac{d(t)}{\|d(t)\|} - \frac{d(t-1)}{\|d(t-1)\|} \right\| \qquad \text{(Equation 25)}$$

where $d(t) = v(t+1) - v(t)$. Calculating the average of Equation 25 over entire boundary yields the average curvature which is formulated as:

$$\kappa_A(v) = \frac{1}{n} \sum_t \kappa_L(t) \qquad \text{(Equation 26)}$$

where n denotes the number of sample points on the boundary. The acceptance criteria associated to curvature descriptors are given by $\max_t \kappa_L(t) < T_{\text{curv\_max}}$ and $\kappa_A(v) < T_{\text{curv\_ave}}$. Restricting the maximum local curvature and average curvature ensures that every point has satisfactory smoothness and tortuosity is precluded.

v. **Signature:** The cross-sections of mitochondria frequently appear as "circular, elliptical or elongated patterns" [53]. Figure 21(c) demonstrates an example for an elongated region. On the other hand, an asterisk shape is an unusual case for a mitochondrion in tomographic images (see Figure 21(d)). Signature functions reserve indicative features which expose such morphologic properties. The signature function of the boundary point j of shape v relative to a reference point i is the distance between i and j as depicted in Figure 21(b) which is given by:

$$S_i(j) = \|v(j) - v(i)\| \qquad \text{(Equation 27)}$$

The "*extension count*" [53] of the object is a useful feature which is determined by the local extrema count N_i of the signature function. The quantity N_i measured within a single period of $S_i(j)$ is proportional to the extension count (e.g. $N_i \leq 2$ and $N_i \leq 4$ is satisfied for a circular object and an elliptic object respectively) as illustrated in Fig 7(c-d). N_i is found to be equal to 6 for the shape given in Figure 21(d). The location of reference point affects the number of local extrema and it should be tested for each boundary point of the shape

in the proposed system. Hence, the condition $\max_i N_i \leq 4$ must be checked in order to accept the candidate shape.

Another useful descriptor is the minimum cross-sectional thickness $L_{\min}$ (see Figure 21(a)) which can be calculated from $S_i(j)$. $L_{\min}$ is given by the least local extrema of the signature function:

$$L_{\min} = \min_{i,k} S_i(m_k) , i \neq m_k \qquad \text{(Equation 28)}$$

where local extrema points are denoted by m_k. In the validation mechanism, too short $L_{\min}$ is not allowed. Hence, the candidate shape must satisfy the condition $L_{\min} > T_{\text{sig\_min}}$. Two additional descriptors are obtained by the length of major and minor axes. The length of major axis (L_{major}) is provided by $\max_{i,j} S_i(j)$. The width of the bounding rectangle aligned with the major axis determines the length of minor axis (L_{minor}) as depicted in Figure 21(a). The descriptors L_{major} and L_{minor} are utilized to check if the candidate shapes does not violate the physical limitations of mitochondria. Therefore, acceptance criteria for major and minor axes' lengths are designated as $L_{\text{major}} < T_{\text{major}}$ and $L_{\text{minor}} > T_{\text{minor}}$.

3.1.8. Post-processing

A competent segmentation of mitochondria may not be achieved by performing a single snake initialization due to the mitochondrial shape and false-positive curves extracted on cristae. For instance, strong internal forces are caused by curvy and

narrow mitochondria and prevents the snake from locating the real boundary. In the proposed approach, multiple initialization is performed for all the curves which surround the same mitochondrion in order solve this problem. A different portion of the mitochondrial region is expected to be covered by each snake as it can be seen from validated shapes shown in Figure 12(g). If the ratio of overlapping area is greater than a threshold, the validated shapes are merged to achieve a better result. The merged contours in Figure 12(h) were obtained by joining shapes continually while the intersectional area with another contour is greater than 30% of the area of the whole shape. Such an automatized merging scheme has a major drawback: it may merge multiple mitochondria together erroneously when an over-inflated snake overlapping more than one mitochondrion is accepted as valid. Nonetheless, this approach can be useful when utilized by semi-automatic systems.

3.2. Extension of the Method to Three-Dimensions

The evolution of 2D snake models are based on the forces created by internal, external and inflation energy acting on 2D vertices. The model is extended to 3D by redefining
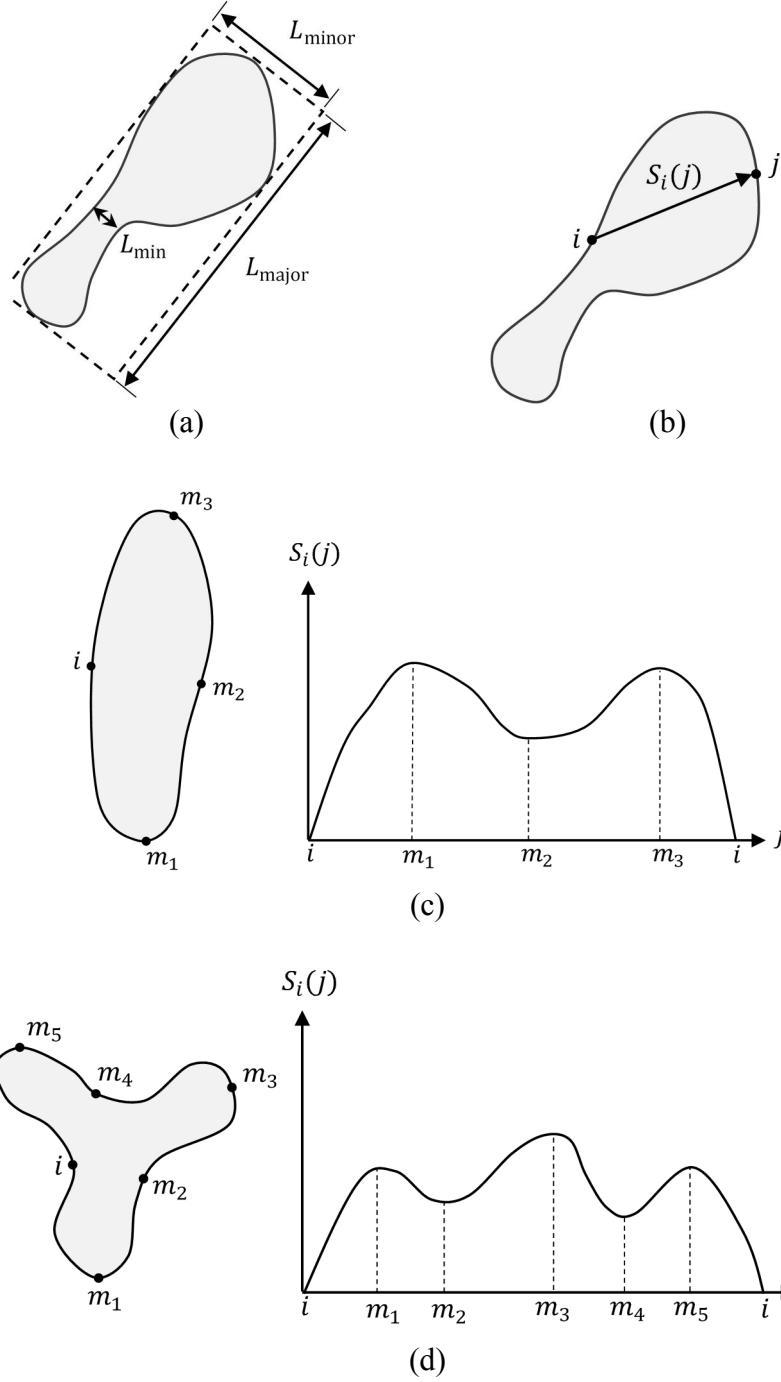
Figure 21: (a) Major axis length (L_{major}), minor axis length (L_{minor}) of a shape and the minimum thickness (L_{min}); (b) Signature function $S_i(j)$ from the reference point i to boundary point j; (c-d) The reference point i and local extremum points m_j on the shape boundary and sketch of corresponding signature function. Adapted from [58].
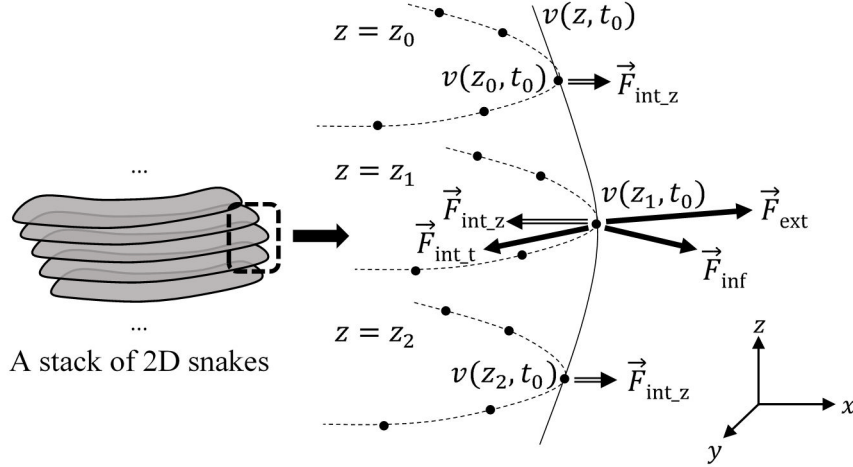
Figure 22: A stack of snakes and acting forces on a vertex of the snake. Reprinted from [58].

vertices as points (x, y, z) in 3D space and arranging the forces as vectors computed along the boundary path on xy-plane and also z-axis [62]. This formulation creates forces which move the vertices in three dimensions and let the snake contour evolve along the z-axis as well as on the xy-plane.

In the proposed system, the 2D balloon snake method employs external forces provided by the large-scale curves which are detected on peripheral membranes of mitochondria. As a drawback, a curve cannot be detected and no force can be created for membranes which are parallel to the xy-plane since such membranes do not show ridge-like pattern in the tomogram. Hence, the 3D extended model cannot be directly integrated to the proposed 2D system. Instead, a pseudo-3D (also known as 2.5D) mechanism is introduced in which a stack of 2D snakes are utilized to build a model in 3D space. Figure 22 depicts internal forces influenced by vertices on the neighboring slices, but acting on their own slice. In this scheme, z-coordinates of vertices does not change. As described in the 2D model, the external and inflation forces are still based on 2D features in this pseudo-3D approach.

3.2.1. A Pseudo Three-Dimensional Snake Approach

Let $v(z, t) = (x_{z,t}, y_{z,t})$ denote the snake boundary as a 2D point on z-level. The internal energy term is extended as follows:

$$E_{\text{int}} = \frac{1}{2}\left(w_{\text{at}}\left\|\frac{\partial v}{\partial t}\right\|^2 + w_{\text{bt}}\left\|\frac{\partial^2 v}{\partial t^2}\right\|^2 + w_{\text{az}}\left\|\frac{\partial v}{\partial z}\right\|^2 + w_{\text{bz}}\left\|\frac{\partial^2 v}{\partial z^2}\right\|^2 \right) \quad \text{(Equation 29)}$$

The weight parameters w_{at} and w_{az} controls the tension on the xy-plane and along the z-axis respectively. Similarly, the weights w_{bt} and w_{bz} controls the amount of curvature. Therefore, minimization of the internal energy is realized by the new update vector as given below:

$$\nabla E_{int} = -w_{at} \frac{\partial^2 v}{\partial t^2} + w_{bt} \frac{\partial^4 v}{\partial t^4} - w_{az} \frac{\partial^2 v}{\partial z^2} + w_{bz} \frac{\partial^4 v}{\partial z^4} \qquad \text{(Equation 30)}$$

Note that a 2D vector is produced by Equation 30 since the vertex v denotes a 2D point. Therefore, 2.5D snake can be considered as the composition of 2D snakes which evolve on their own z-level. The snake update equation can be rewritten by adding external and inflation energy terms:

$$\nabla E_{snake} = \nabla E_{int} + \nabla E_{ext}^{(z)} + \nabla E_{inf} \qquad \text{(Equation 31)}$$

where $\nabla E_{ext}^{(z)}$ is the gradient of external energy image obtained for slice z and ∇E_{inf} is update term for the inflation energy which is acquired in a 2D manner on a slice-by-slice basis. Figure 22 visualizes the update terms as the forces acting on vertices generated by inversely oriented update vectors (i.e. $\vec{F} = -\nabla E$). $\vec{F}_{int\_t}$ and $\vec{F}_{int\_z}$ are internal forces illustrated in Figure 22 that originates from the first two and the last two terms given in Equation 30 respectively. The internal force $\vec{F}_{int\_z}$ obtained by the derivation over z-axis endeavors to align the vertices along z-axis. Therefore, the snake boundary indirectly evolves in 3D via the interaction of forces while the energy is minimized considering neighboring slices.

3.2.2. Snake Initialization

The 2D algorithm implies the initialization of snakes as small circles (e.g. unit circle) near to the large-scale curves which have sufficiently high energy indicating the presence of mitochondrion. Although this approach can be used to scan the entire image to detect mitochondria, it is problematic for 3D segmentation since the snakes may be initialized differently since the curves can be displaced for other slices. Moreover, the validator function individually evaluates resulting snakes in slice-by-slice basis. As a result, obtained contours can be inconsistent depending on initialization and validation of snakes for each slice. Hence, a smooth 3D mesh cannot be generated by a 2D system. However, the inconsistency problems can be reduced by utilizing a better initialization approach in which large-scale curves extracted from multiple slices are used considering that the potential displacement of membranes and diversity in membrane detection along z-axis. In this approach, a modified version of Density-Based Spatial Clustering of Applications with Noise (DBSCAN) [63] algorithm is used to determine the initial locations of snakes.

41
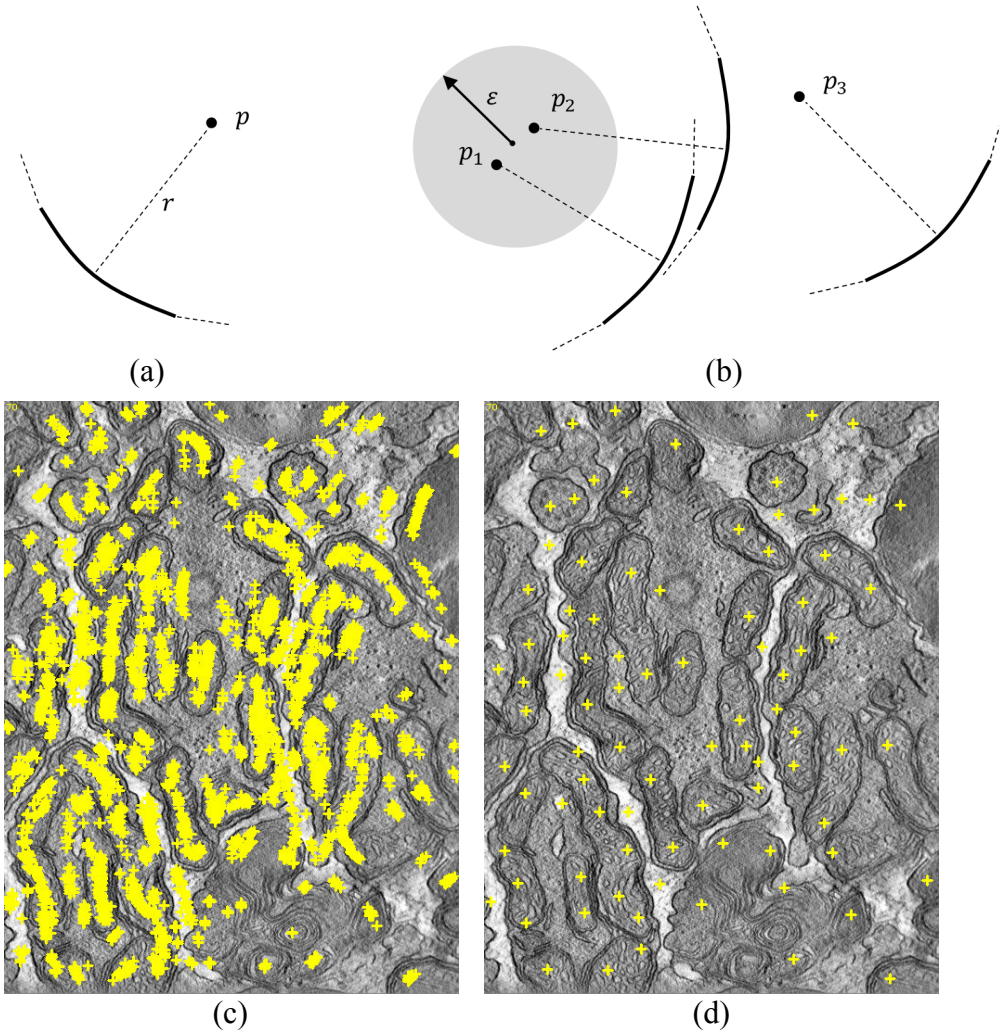
Figure 23: (a) A cue point p of a curve segment and (b) a cluster formed by the cue points; (c) Cue points extracted from the dataset "od_sub" (slice range: 70–89) and (d) corresponding cluster centers. Reprinted from [58].

The *cue point* of a curve segment is defined as the point located in the perpendicular direction to the vertex point with distance r in the concave side of the parabolic arc as illustrated in Figure 23(a). Cue points residing in a certain neighborhood support each other if they are located in the concave sides of the curve segments. For instance, the points p_1 and p_2 support each other whereas p_3 is blackballed as illustrated in Figure 23(b). The actual initial points are determined by the center of clusters which are formed by the adequately populated supportive cue points located in a neighborhood. Hence, snakes are initiated as a cylinder (or a circle in the 2D case) on the cluster centers. The distance parameter r and cylinder diameter should be adjusted to a value less than the expected minimum cross-sectional thickness for the mitochondrion in order to ensure that the mitochondrion boundary is caught by the snake boundary. On the other hand, z-thickness of the cylinder should be adjusted according to the height

of the mitochondrion visualized in 3D volume. A better surface is expected to be extracted when z-thickness is high since more information is utilized. However, a snake cannot successfully converge if z-thickness is longer than the size of the mitochondria. The clusters which are not sufficiently populated by cue points are neglected in order to perform a reliable snake initialization. Thus, false positive detections are reduced.

The initialization of snakes is carried out by the following algorithm:

  i. Determine a cue point for each curve detected in a given z-range.
 ii. Find all supportive cue points within ε neighborhood for every cue point.
iii. Create a cluster for each neighborhood if sufficient number of cue points are available in the cluster.
 iv. Initialize snakes as cylinders at cluster centers (i.e. the center of mass populated by the cue points in the cluster).

Multiple curve segments overlapping each other can be detected on a strong membrane. Similarly, the curves detected on a strong membrane are expected to have neighboring curves at close-range along the z-axis. Therefore, the neighboring cue points along z-axis may also support each other based on the proximity on xy-plane. Cue points extracted from 20 slices of a dataset and corresponding cluster centers are displayed in Figure 23(c) and Figure 23(d) respectively. Since a range of tomograms are utilized for the initialization process, mechanism is a robust against noise and false detections.

The original version of DBSCAN algorithm forms dense clusters in which each point is within a neighborhood of at least one point in the cluster. Such an approach makes the cluster as wide as possible by covering a pervasive distribution in a single cluster. However, this is not a desired property in the proposed system since attempting multiple initializations inside the mitochondrion could lead to a better segmentation. In the proposed modified algorithm, the extent of clusters is bounded by ε neighborhood such that centers of created clusters are located at least 2ε distant.

3.2.3. Adaptation of the Validator Function

A given 2D snake is accepted or rejected by the validator function in the 2D method. Formally, the validator function is defined as $F: v \rightarrow \{0,1\}$ where v denotes a 2D shape. Hence, the function returns 0 in case of rejection and returns 1 in case of acceptance. The 2.5D snakes are validated by a validity measurement which utilizes 2D validator function and is formulated as:

$$V(v) = \frac{1}{k} \sum_{z=1}^{k} F(v_z) \qquad \text{(Equation 32)}$$
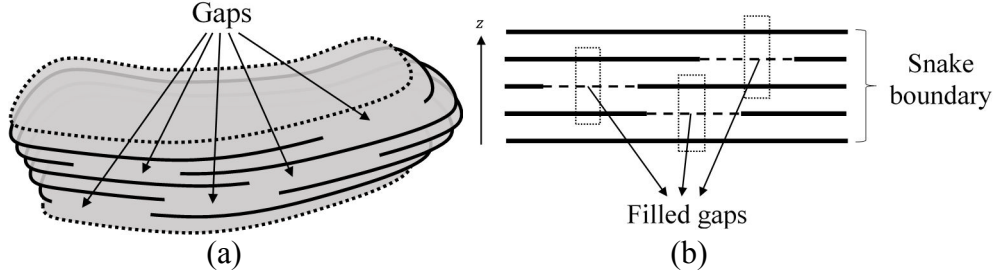
Figure 24: (a) A 2.5D snake is assumed to have gaps where boundary energy is weak; (b) gap filling mechanism. Reprinted from [58].

where v_z denotes a 2D cross section of snake v at z-level and k denotes the z-thickness of the snake such that $1 \leq z \leq k$. The validity measurement V is a real-valued function ranging over $[0,1]$ indicating the probability of the shape being correct. In a sense, a voting process is applied for the validity measurement that produces the acceptance ratio over all voters. Hence, if the validity value $V(v)$ is greater than a threshold (T_V), the snake v is accepted. Otherwise it is rejected.

The 2.5D model has gap-filling property along both t- and z-axis by means of internal energy gained by neighboring slices despite the lack of external energy. In such cases, some of cross-sections of snake may appear invalid due to a large amount of gaps in different z-levels. This problem leads to unexpectedly low validity value although a successful segmentation is obtained. An explanatory example is depicted in Figure 24(a) in which each snake slice has significant gaps which results in the rejection of the 2D cross-sectional shape. Therefore, the validity value of the entire shape is found to be very low. This problem can be solved by applying median filter to the boundary energy measurement $\sum_{p \in C_L} E_{\mathrm{curve}}(t, p)$ within the window placed along z-axis as shown in Figure 24(b). A vertex point on the snake is assumed to be a gap if this measurement is below a threshold. Thus, the filtering operation artificially fills the gap if there exists sufficient neighbors with high boundary energy. Conversely, if there is no sufficiently strong neighborhood along the z-axis, the vertex point is considered a false detection and becomes a gap.

3.2.4. Adaptation of the Post-Processing

The merging operation is performed by considering overlapping volumes of extracted regions in the 3D case. In this manner, validated 2.5D snakes are iteratively joined together until there exist no region such that the ratio of the overlapping volume to the whole volume is greater than the threshold (i.e. 70% of the entire volume of the shape).

CHAPTER 4

RESULTS

This chapter presents properties of the datasets utilized in the experiments, evaluation and comparison of the algorithms described in *Chapter 3*. Both 2D and 2.5D algorithms were tested on eight datasets listed in Table 1. The parameter sets used in the experiment are listed in Table 2. The validation process were exerted to the candidate detections attained from the 2.5D snake algorithm by both enabling and disabling the gap filling mechanism (as described in *Section 3.2.3*).

The test range for parameters and experimental setup is given below:

- The size of gap filling window (W_{gap}) was set to 3, 5, 7 and 9.
- The z-thickness (k) was separately adjusted as 10, 20, 30 and full (i.e. dataset thickness) for the 2.5D snake model.
- Each dataset has been divided into sub-sections such that k consecutive slices are contained in each sub-section. For instance, a dataset composed of 100 slices was divided into five sections for $k = 20$. Then, the snakes were initialized and executed individually for each sub-section.
- In post-processing step, obtained regions have been merged if the overlapping area (or volume in 3D case) was larger than to 30% of the whole region.
- The entire test procedure was repeated by adjusting gap parameters to three individual settings presented in Table 2.

Figure 25 illustrates the convergence comparison of 2D and 2.5D snakes. Figure 25(a) demonstrates that 2D snake encounters over-inflation problems caused by inadequate curve detection on peripheral membranes. Figure 25(b), on the other hand, shows the capability of the 2.5D model compensating false-negative error. Similarly, the presence of false-positive curves on cristae prevents the balloon from inflating properly in 2D approach whereas 2.5D model managed to cope with this problem by means of neighboring slices. Instability problems were also encountered in the 2D model such that false-positive and false-negative error is significantly visible neighboring slices. On the contrary, 2.5D model exhibits a robust behavior when compared to the 2D model.

Figure 26(a) illustrates a sample segmentation of sub-sections of a mitochondrion for the snake thickness $k = 20$. The segmentation of the same mitochondrion with full z-

thickness (i.e. dataset thickness) is shown in Figure 26(b). Figure 26(c) illustrates the segmentation results for several mitochondria acquired by using the full z-thickness. Figure 27 demonstrates sample tomograms delineating the boundary of segmentation chosen from each dataset.

4.1. Dataset

The datasets used for the experiments in this study were gathered from the Cell Centered Database (CCDB) supported by the National Center for Microscopy and Imaging Research (NCMIR) [64]–[66]. Eight TEM datasets were chosen which show variety in image contrast and mitochondrial membrane and crista patterns. Mitochondria appear in different shapes and sizes in the dataset collection. Table 1 lists some attributes of the datasets such as voxel size, dataset thickness and image size.

The dataset collection comprises a total of 622 slices and 96 mitochondria. Ground truth was obtained by specifying the outer membranes of mitochondria via a manual segmentation process using IMOD software [24]. The tomograms pertaining to the very top and bottom slices of the datasets are very blurry and useless. Therefore, those parts were neglected in ground truth. It is notable to stress that preparing such a ground truth database necessitates significant amount of manual exertion. It is obvious that such a process consumes a considerable amount of time justifying that computerized detection and segmentation is essential to accelerate analysis of electron tomography.

Table 1: Properties of datasets used in the experiments.

Dataset basename	Accession number	Image size (width × height)	Number of slices used	Voxel size (nm) ($X \times Y \times Z$)
6_22.sub	5274878	1960 × 2560	91	1.1 × 1.1 × 1.1
bclpb-d.sub	5274930	720 × 878	61	2.4 × 2.4 × 2.4
cone.sub	54	736 × 1010	97	2.4 × 2.4 × 2.4
gap18_sub	8747	350 × 600	54	2.2 × 2.2 × 2.2
mac_serial_sub	5274996	907 × 1172	111	2.4 × 2.4 × 2.4
od.sub	8752	1960 × 2560	91	1.1 × 1.1 × 1.1
pedicle	5274970	950 × 1280	31	2.4 × 2.4 × 2.4
spherule24mos1	8495	1996 × 1996	86	1.67 × 1.67 × 1.67

Table 2: List of parameters and settings used in the proposed system.

Parameter description	Used setting		
Preprocessing parameters			
Auto-contrast histogram cut	0.5%		
Resampling pixel-size	2 nm		
Bilateral filtering spatial kernel size	60 nm		
Bilateral filtering gray deviation	0.2		
Ridge detection parameters			
Gaussian derivative sigma	3 nm		
Energy mapping parameter			
Window size (ω)	30 nm (LFREM)		
	8 nm (HFREM)		
Curve fitting parameters			
Threshold energy (T_{map}) for initialization	40% of max $e_\theta(s)$		
Curve update parameters (τ_x, τ_y, τ_h)	8 nm		
Curve filtering parameters			
Max. allowed value for curvature (κ)	1		
Min. arc length	100 nm (large-scale curves)		
	20 nm (small-scale curves)		
Min. average energy	30% of max $e_\theta(s)$		
Shape extraction / snake initialization parameters			
Tension weight ($w_{\mathrm{a}}, w_{\mathrm{at}}$)	1.0		
Curvature weight ($w_{\mathrm{b}}, w_{\mathrm{bt}}$)	200		
External energy weight (w_{c})	0.5 (2D)		
	1.0 (2.5D)		
Inflation weights (w_{d})	0.5, 1.0, 1.5 … 3.0		
Tension weight along z-axis (w_{az})	5.0		
Curvature weight along z-axis (w_{bz})	5.0		
z-thickness (k)	1 (2D), 10, 20, 30, max.		
Distance to the vertex point of arc (r)	40 nm		
Cluster neighborhood (ε)	100 nm		
Min. cluster size	$\lfloor$1.5 x z-thickness$\rfloor$		
Validator function parameters			
Min. average boundary energy ($T_{\mathrm{energy\_b}}$)	20		
Min. average region energy ($T_{\mathrm{energy\_c}}$)	0.1		
Max. local curvature ($T_{\mathrm{curv\_max}}$)	1/45 nm^{-1}		
Max. average curvature ($T_{\mathrm{curv\_ave}}$)	1/180 nm^{-1}		
Max. local extrema count ($\max_i N_i$)	4		
Min. thickness ($T_{\mathrm{sig\_min}}$)	70 nm		
Max. major axis length (T_{major})	2000 nm		
Min. minor axis length (T_{minor})	140 nm		
Min. area ($T_{\mathrm{area\_min}}$)	0.02 μm^2		
Max. area ($T_{\mathrm{area\_max}}$)	0.7 μm^2		
Gap-filling window size (W_{gap})	3, 5, 7, 9		
	1st setting	**2nd setting**	**3rd setting**
Boundary energy measurement threshold ($T_{\mathrm{gap\_energy}}$)	5	10	15
Total gap length ($T_{\mathrm{gap\_total}}$)	500 nm	500 nm	600 nm
Max. gap length ($T_{\mathrm{gap\_max}}$)	400 nm	400 nm	600 nm
Max. gap ratio ($T_{\mathrm{gap\_ratio}}$)	0.4	0.4	0.4
Max. gap ratio on border ($T_{\mathrm{gap\_border}}$)	0.3	0.3	0.4
Post-processing parameter			
Merging threshold	30% of area (or volume) overlapped		
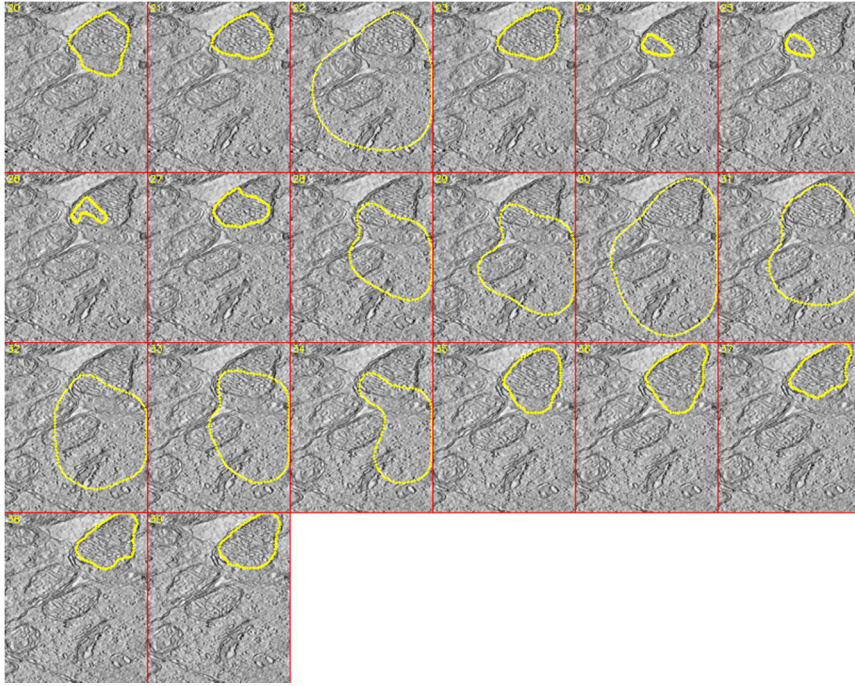
(a)
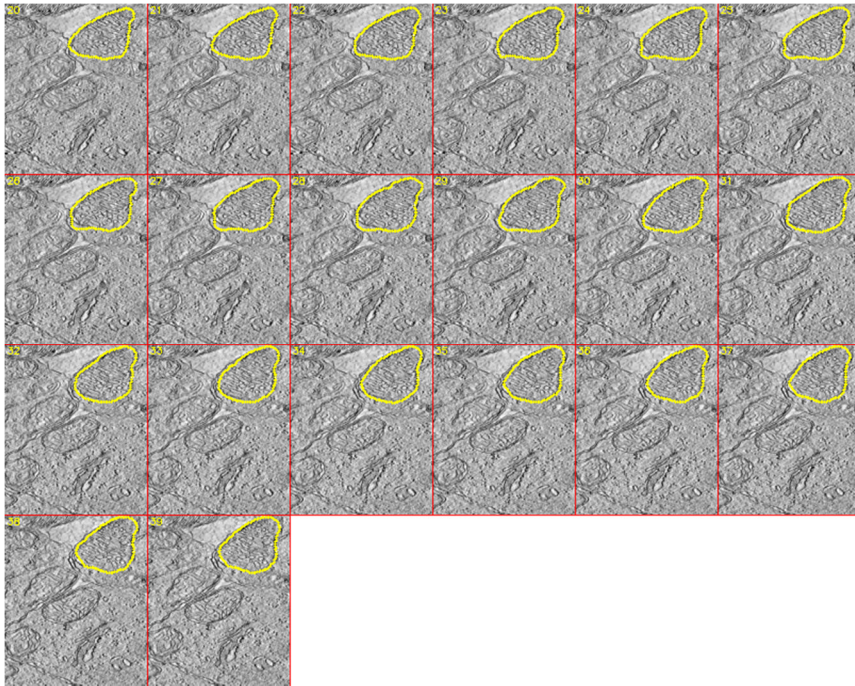
(b)

Figure 25: Boundary of an identically initialized (a) 2D snake output (performed in slice-by-slice manner) and (b) 2.5D snake output for the dataset "bclpb-d.sub" (slice range: 20–39). Adapted from [58].
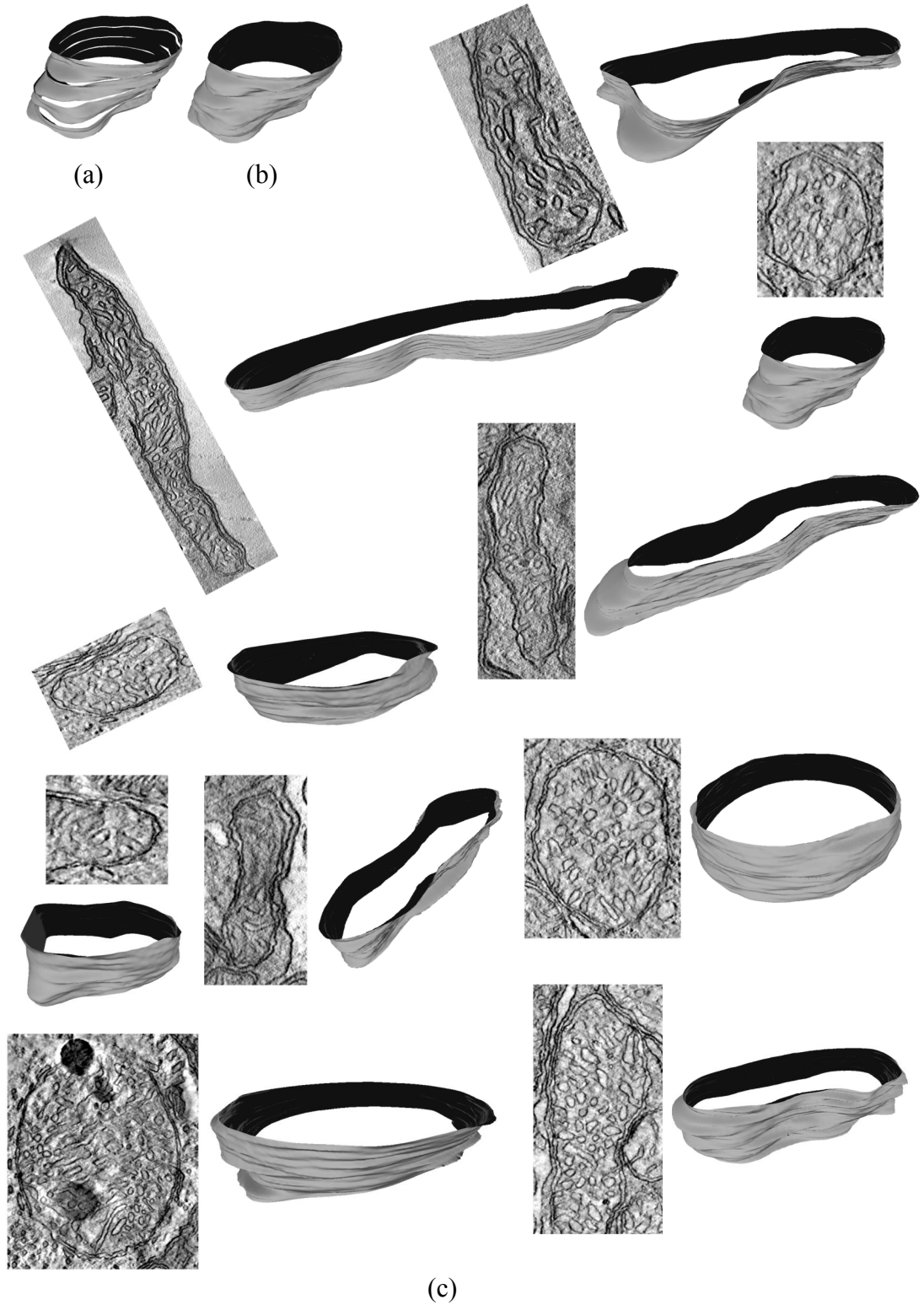
Figure 26: A sample merged shape with (a) $k = 20$ and (b) $k = 80$; (c) Merged shape samples for maximum valid n. The outputs were visualized by MeshLab tool [72]. Adapted from [58].
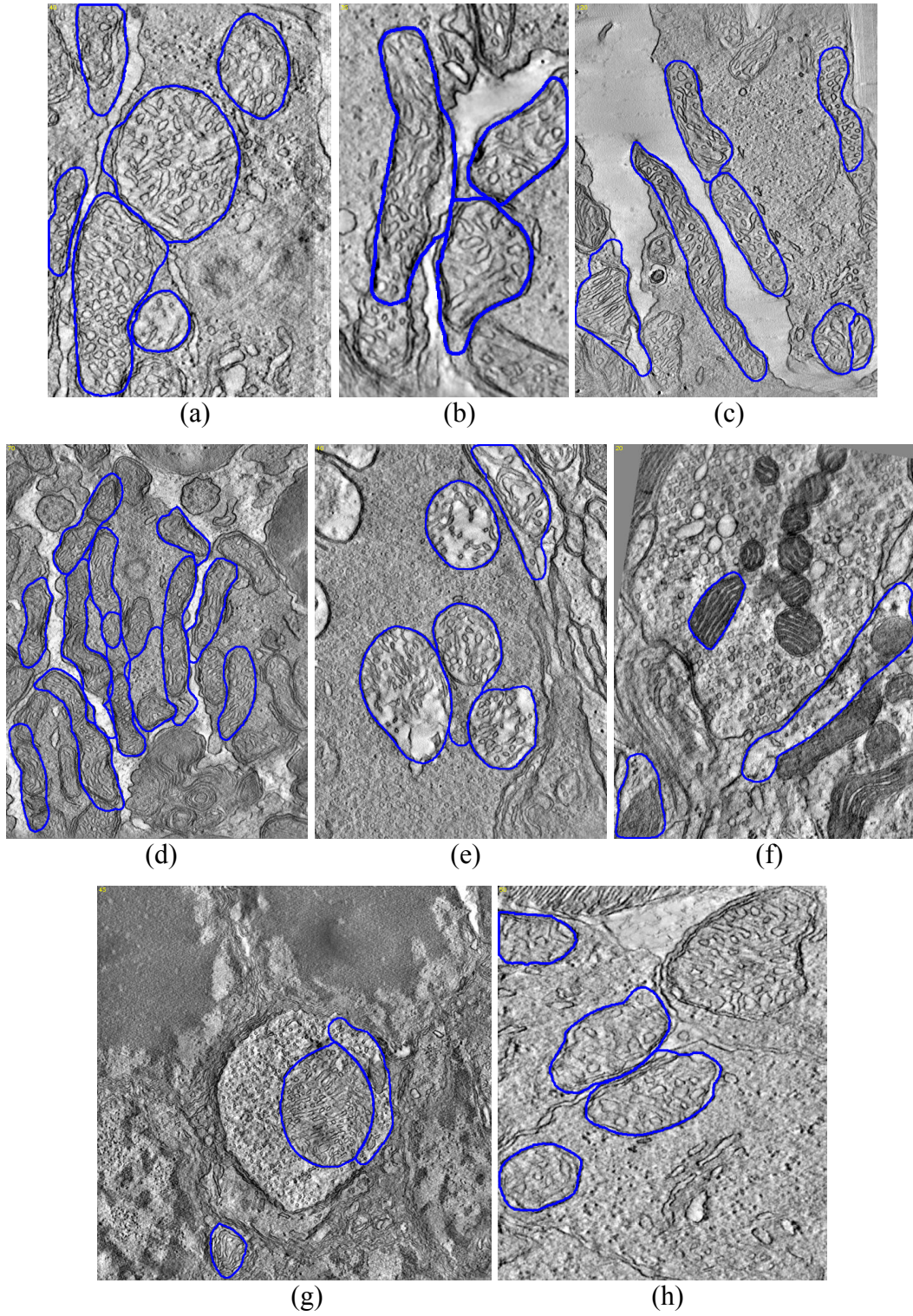
Figure 27: Mitochondria segmentation results (Image basename and slice number): (a) cone.sub (slice #: 40); (b) gap18_sub (slice #: 35); (c) 6_22.sub (slice #: 120); (d) od.sub (slice #: 70); (e) pedicle (slice #: 40); (f) mac_serial_sub (slice #: 20); (g) spherule24mos1 (slice #: 45); (h) bclpb-d.sub (slice #: 50). Adapted from [58].
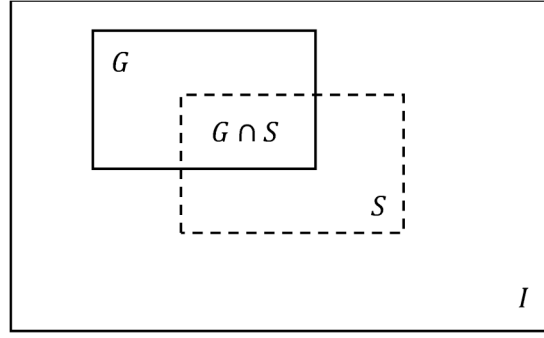
Figure 28: An image I, a region G to be segmented and the region S segmented by the algorithm.

4.2. Performance Evaluation

Two fundamental indicators for algorithm performance are precision and recall that are frequently used to measure the detection accuracy. Precision is equal to the ratio of the correct detections to all detections (*true positives/all positives*). Recall equals to ratio of correct detections to all true elements (*true positives/all true elements*). For an image I (see Figure 28), formal definitions of precision and recall are as follows:

$$\text{Precision} = \frac{|G \cap S|}{|S|} \qquad \text{(Equation 33)}$$

$$\text{Recall} = \frac{|G \cap S|}{|G|} \qquad \text{(Equation 34)}$$

where G denotes the actual region to be segmented and S denotes the region which is segmented by the algorithm. The definitions of precision and recall are generally adapted to image segmentation problems by using the pixels as the elements to be detected. Thus, precision is measured by the ratio of the size (i.e. area in 2D or volume in 3D domain) of correctly detected regions to the total size of all extracted regions whereas recall is measured by the ratio of the size of correctly detected regions to the total size of all true regions in accordance with formal definitions. However, these definitions can be altered due to the problem domain, interpretation and expectations from the results.

In the preliminary study (described in *Chapter 2*) [52], a detection was assumed to be correct if at least 70% of the extracted region belongs to a single mitochondrion. Then, precision and recall were measured by calculating the number of correct regions (not the area of regions). This approach ensures an accuracy evaluation for each extracted region considering whether one region only segments a single mitochondrion or not. However, this definition also implies that an extracted region is assumed as correct

even if it corresponds to only a small fragment of the mitochondrion. In other words, the entire mitochondrion is accepted as successfully detected even if the most part of the mitochondrion is not segmented. Indeed, even a small segmented region entails a successful detection of entire mitochondrion. In order to dissipate this drawback, a new procedure has been followed to measure precision and recall in the proposed study (described in *Chapter 3*) by considering potential regions produced by algorithm. In the first step, each extracted region is matched to a single mitochondrion which maximizes the Dice Similarity Coefficient (DSC). The DSC is given by:

$$\text{DSC}(G,S) = \frac{2|G \cap S|}{|G| + |S|}$$
(Equation 35)

where G and S denote the ground truth and the extracted region produced by the algorithm respectively. The cardinality operator $|\cdot|$ expresses the area (or volume in 3D case) of the region. Let S_i be the ith extracted region and G_i be the ground truth corresponding to the ith mitochondrion and let G_i' be the matched ground truth for S_i. The measurement of precision and recall are formulated as below:

$$\text{Precision} = \frac{|\bigcup_i G_i' \cap S_i|}{|\bigcup_i S_i|}$$
(Equation 36)

$$\text{Recall} = \frac{|\bigcup_i G_i' \cap S_i|}{|\bigcup_i G_i|}$$
(Equation 37)

Note that the union of intersections of each shape with the matched ground truth is involved in the numerator of the fractions in Equation 36 and Equation 37. Therefore, the detection accuracy is evaluated based on integrity of segmentation while a single mitochondrion is allowed to be segmented by a union of regions. Since the measurement of area (or volume in 3D case) is involved in recall and precision formulation, reasonable values are obtained. Segmentation accuracy has been additionally measured by using two metrics:

i. **Dice Similarity Coefficient (DSC):** The average DSC (see Equation 35) over all matched ground truth has been computed.

ii. **Median Symmetric Boundary Error (MSBE):** MSBE is equal to the median of Euclidean distances from each point on snake boundary to mitochondrion boundary and from each point on mitochondrion boundary to snake boundary. This quantity may be formulated as:

$$\text{MSBE}(\hat{G}, \hat{S}) = \text{median} \left(\left\{ d \,\middle|\, d = \min_j \|\hat{S}(i) - \hat{G}(j)\|, i = 1,2, \dots, N \right\} \right.$$
$$\left. \cup \left\{ d \,\middle|\, d = \min_i \|\hat{S}(i) - \hat{G}(j)\|, j = 1,2, \dots, M \right\} \right)$$
(Equation 38)

where $\hat{G}(j)$ and $\hat{S}(i)$ are boundary points, N and M are the number of points on the boundary of ground truth and snake output respectively.

4.3. Quantitative Results

The precision and recall have been measured for all possible validity threshold values (T_V). The recall has been individually calculated for both fully seen and all available mitochondria. DSC and MSBE have been calculated for both original and merged extracted regions. Additionally, F-score metric (harmonic mean of precision and recall) has been utilized to facilitate the comparison of algorithm performance since it performs a balanced evaluation depending on precision and recall [67].

Table 3 lists average precision and recall values corresponding to snake thickness and several validation parameters which maximize F-score. 2D method has a precision value of 0.71 whereas it goes up to 0.81 for 2.5D method. Recall was also slightly improved for fully seen mitochondria. It was found as 0.84 and 0.87 for 2D and 2.5D methods respectively. The best results were attained for the snake thickness $k = 20$ and the validity threshold $T_V = 0.75$. Henceforth, the best-case outcomes of the 2D and 2.5D snakes with respect to k and T_V are presented and discussed below unless stated otherwise.

Table 3: The best achievements of the algorithms and corresponding parameters.

Snake thickness (k)	Gap window (W_{gap})	Gap setting	Validity threshold (T_V)	Precision	Recall Fully seen	Recall All	F-Score Fully seen	F-Score All
1 (2D)	N/A	2nd	N/A	0.71	0.84	0.71	0.77	0.71
10 (2.5D)	5	1st	0.5	0.74	0.87	0.76	0.80	0.75
20 (2.5D)	5	3rd	0.75	0.81	0.87	0.71	0.84	0.76
30 (2.5D)	5	3rd	0.7	0.80	0.86	0.69	0.82	0.74
Full (2.5D)	3	3rd	0.6	0.79	0.87	0.71	0.83	0.75

The precision and recall graph versus T_V is exhibited in Figure 29(a). While T_V is increasing, the precision increases and the recall decreases. In other words, when a stronger consensus is achieved, the more reliable voting process is attained. However, some of the correct detections are lost for precise decisions (false negative error). The F-score versus T_V graph is illustrated in Figure 29(b) indicating the performance of the 2D method. According to the figure, 2.5D method performed better than 2D method for a wide range of T_V.

Table 4 shows a comparison between the detection achievements of 2D and 2.5D methods for eight datasets. Since the mitochondria boundaries do not appear as ridge-like structures in the dataset "mac_serial_sub", both methods are unsuccessful for this particular dataset due to inaccurate ridge detection. Although the outer membrane is
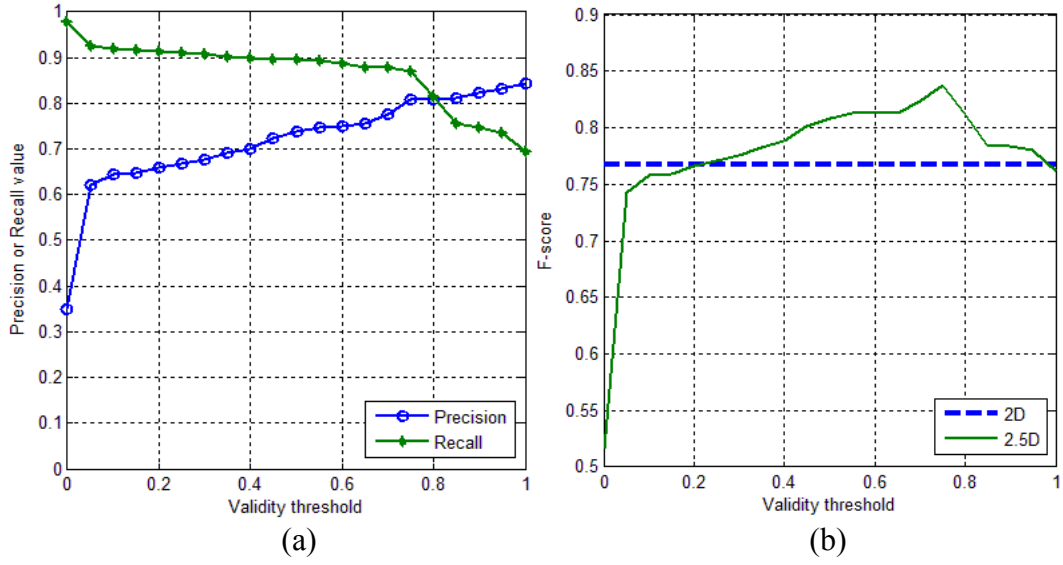
Figure 29: (a) The detection performance of 2.5D snake ($k = 20$; $W_{gap} = 5$; gap setting: 3rd) and comparison with 2D snake (gap setting: 2nd): (a) Precision-recall (fully seen) vs. validity threshold (T_V) graph; (b) F-score (fully seen) vs. validity threshold (T_V) graph. Reprinted from [58].

Table 4: The detection performance of 2.5D snake ($k = 20$; $W_{gap} = 5$; gap setting: 3rd; $T_V = 0.75$) and 2D snake (gap setting: 2nd) algorithms for eight datasets.

Dataset basename	2D			2.5D		
	Precision	Recall		Precision	Recall	
		Fully seen	All		Fully seen	All
6_22.sub	0.76	0.86	0.65	0.84	0.80	0.58
bclpb-d.sub	0.82	0.73	0.59	0.88	0.95	0.57
cone.sub	0.87	0.93	0.73	0.92	0.93	0.81
gap18_sub	0.79	0.79	0.60	0.85	0.84	0.60
mac_serial_sub	0.31	0.23	0.20	0.45	0.06	0.11
od.sub	0.60	0.75	0.64	0.65	0.62	0.52
pedicle	0.68	0.86	0.83	0.90	0.95	0.92
spherule24mos1	0.43	0.95	0.95	0.62	0.99	0.99
Average	**0.66**	**0.76**	**0.65**	**0.76**	**0.77**	**0.64**
Average (excluding mac_serial_sub)	**0.71**	**0.84**	**0.71**	**0.81**	**0.87**	**0.71**

visible, the cristae and inner boundary membranes are not apparently observable since condensed mitochondria are populated in this dataset. Although this is not an exceptional case, a high contrast between membranes and background is expected in order to perform a cristae segmentation. Therefore, the average performance is individually presented by including and excluding the problematic dataset. When it is ignored, precision and recall for 2.5D approach are improved by 14% and 1% respectively relative to 2D performance. Apparently, 2D method achieves a better recall value compared to the 2.5D in the datasets "od_sub" and "6_22.sub". Note that 2D algorithm performance was evaluated on a slice-by-slice basis since the segmentation is individually accomplished for each particular slice.

The effect of gap filling mechanism to algorithm performance with respect to the window size (W_{gap}) is presented in Table 5. This process leads to a decrease in precision but an increase in recall. Specifically, a larger window induces a greater decrease in precision but a greater increase in recall. Activating this mechanism is reasonable, since the loss in precision is less than the gain in recall. Experiments show that adjusting $W_{\text{gap}} = 5$ (in terms of the number of tomograms) is generally feasible.

Table 5: The detection performance of 2.5D snake ($k = 20$; gap setting: 3rd; $T_V = 0.75$) with respect to different values of gap window size (W_{gap}).

Gap window size (W_{gap})	Precision	Recall		F-Score	
		Fully seen	All	Fully seen	All
Disabled	0.82	0.75	0.59	0.78	0.68
3	0.81	0.82	0.66	0.82	0.73
5	0.81	0.87	0.71	0.84	0.76
7	0.78	0.87	0.71	0.82	0.75
9	0.77	0.88	0.72	0.82	0.75

The segmentation accuracy of algorithms evaluated by two metrics (DSC and MSBE) according to the snake thickness (k) is given in Table 6. MSBE values are presented in terms of nanometers. Assessment results of the original and merged versions of extracted regions are exhibited separately. The best achievements have been attained by using the 2nd gap setting for 2D snakes. 2.5D snakes have performed best when $k = 20$, $W_{\text{gap}} = 5$ and $T_V = 0.75$ with the 3rd gap setting (the entire list for parameter adjustments is given in Table 2). The average DSC was found as 0.79 and 0.84 for the 2D and 2.5D method respectively. A finer segmentation has been usually achieved by the merged regions since some of the mitochondria are represented by the union of regions. However, merging operation may accidentally merge more than one mitochondrion causing a false detection. Segmentation accuracy of merged snakes were measured by removing such falsely merged regions. The average of MSBE was

Table 6: Segmentation accuracy of 2D snake (gap setting: 2nd) and 2.5D snake ($k = 20$; $W_{gap} = 5$; gap setting: 3rd; $T_V = 0.75$) algorithms for different thickness values and datasets.

Metric	DSC									
Snake state	Original					Merged				
	Snake thickness (k)					Snake thickness (k)				
Dataset	1 (2D)	10	20	30	Full	1 (2D)	10	20	30	Full
6_22.sub	0.68	0.68	0.72	0.74	0.73	0.72	0.76	0.75	0.77	0.82
bclpb-d.sub	0.85	0.89	0.92	0.92	0.91	0.86	0.90	0.91	0.91	0.89
cone.sub	0.86	0.86	0.93	0.93	0.94	0.88	0.87	0.90	0.90	0.90
gap18_sub	0.82	0.84	0.82	0.82	0.85	0.85	0.89	0.87	0.86	0.87
mac_serial_sub	0.68	0.71	0.73	0.77	0.35	0.65	0.69	0.70	0.77	0.35
od.sub	0.75	0.77	0.78	0.78	0.75	0.70	0.73	0.77	0.76	0.72
pedicle	0.73	0.72	0.79	0.77	0.74	0.78	0.78	0.91	0.83	0.84
spherule24mos1_	0.85	0.82	0.92	0.87	0.98	0.92	0.95	0.97	0.97	0.97
Average	**0.78**	**0.79**	**0.83**	**0.82**	**0.78**	**0.79**	**0.82**	**0.85**	**0.85**	**0.80**
Average (excluding mac_serial_sub)	**0.79**	**0.80**	**0.84**	**0.83**	**0.84**	**0.81**	**0.84**	**0.87**	**0.86**	**0.86**
Metric	MSBE (in nanometers)									
Snake state	Original					Merged				
	Snake thickness (k)					Snake thickness (k)				
Dataset	1 (2D)	10	20	30	Full	1 (2D)	10	20	30	Full
6_22.sub	33	30	24	24	18	32	23	32	34	14
bclpb-d.sub	16	11	8	10	9	17	11	9	11	9
cone.sub	18	17	10	10	9	14	14	10	10	10
gap18_sub	12	9	9	8	9	12	9	9	9	10
mac_serial_sub	26	19	28	21	110	31	23	42	21	110
od.sub	20	19	18	18	22	31	26	22	24	31
pedicle	48	49	41	49	50	32	32	11	21	21
spherule24mos1_	30	31	18	28	8	15	9	7	7	8
Average	**25**	**23**	**20**	**21**	**29**	**23**	**18**	**18**	**17**	**27**
Average (excluding mac_serial_sub)	**25**	**24**	**18**	**21**	**18**	**22**	**18**	**14**	**17**	**15**

Table 7: Average execution time of major steps in the system.

Step name	Scale	Duration (sec)
Preprocessing	Per slice	0.6
Curve detection	Per slice	18.1
Snake algorithm (2D)	Per slice	293.7
	Per snake-slice	0.5
Snake algorithm (2.5D)	Per slice	194.1
	Per snake-slice	0.5

found as 14 nm for the best-case. The segmentation is not so precise compared to the preliminary study [52]. This is an expected consequence since the accurate double membrane extraction step has not been employed. Nonetheless, it is adequate to specify rough annotations considering that the total double membrane thickness of most of mitochondria is between 18 and 48 nm.

Table 7 exhibits average computation times for major steps in the proposed system. All computations were accomplished by a single thread on a computer running on Intel Core 2.4 GHz microprocessor. The entire system was implemented in C++ programming language by using OpenCV library. CPU utilization was approximately 33% less for 2.5D snake algorithm with respect to the 2D method since the proposed initialization process precipitates even better segmentation by generating 33% less initial points. Although 2.5D method involves relatively complex computation, no significant increase in CPU time per snake slice was measured.

The signal-to-noise ratio (SNR) robustness of the system was tested by using a mitochondrion phantom (see Figure 30) taken from Figure 7 in the study by Fernández, J.J. [68]. Although the phantom was not adequately realistic in order to assess the entire system, the algorithm was executed to observe the curve fitting and the snake segmentation behavior on synthetic peripheral membrane. The phantom was subjected to additive Gaussian noise. Figure 31 depicts a sample tomogram with different SNR values (∞, 20, 10, 4, 2, 1.33, 1.0, 0.80, 0.66 and 0.5). The curve fitting results are shown in Figure 32. No small-scale curve (shown in red) was obtained for SNR $\geq$ 4 since the phantom does not possess realistic curvy cristae patterns. Some false-positive curves were obtained for SNR $\leq$ 2. The whole boundary was covered by large-scale curves (show in blue) in all tomograms for SNR $\geq$ 0.80. However, small-scale curves were too sparse to validate the candidate regions. Hence, the average region energy threshold (T_{energy_c}) was lowered to zero (i.e. disabled) in order to observe the final results. Other parameters were left unchanged. The boundary was partially covered for SNR = 0.66. Since ridges are remarkably weakened for SNR = 0.5, large-scale curves were mostly mislaid. Initial points of snakes were depicted in Figure 33. All initial points were discovered inside of the mitochondrion. The algorithm was not successful for SNR = 0.5 due to insufficient large-scale curves detection. Figure 34 exhibits the
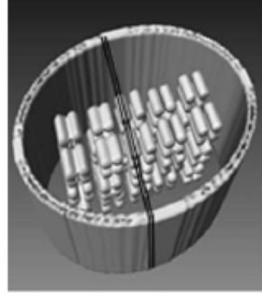
Figure 30: A mitochondrion phantom taken from Figure 7 in the study by Fernández, J.J. et al. in [68].
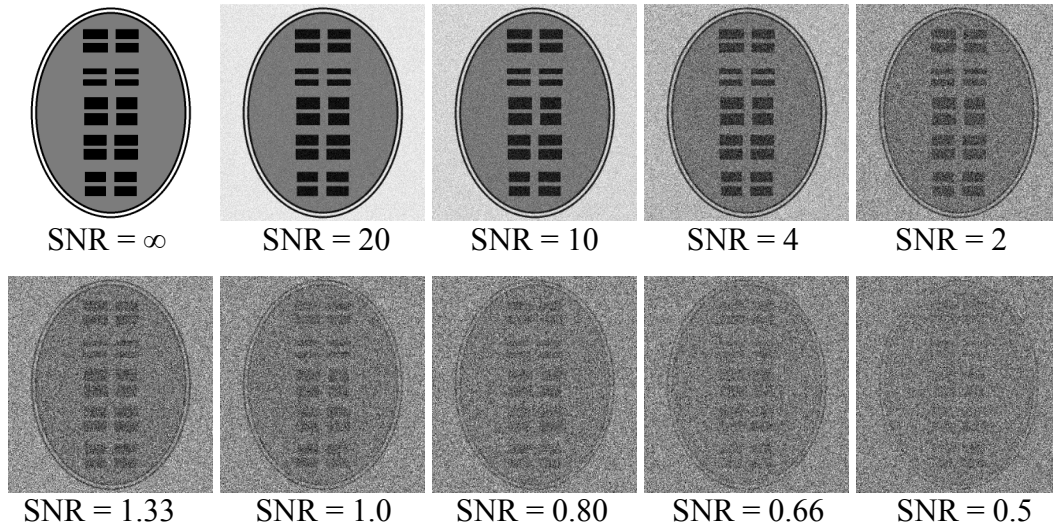
Figure 31: Additive Gaussian noised cross-section of phantom with respect to different SNR values. Reprinted from [58].

segmentation results. Although satisfactory results have been obtained for SNR ≥ 0.80, small amount (a few pixels) of fluctuation was observed on the segmentation boundary along the z-axis for SNR ≤ 1. Although all snakes were invalidated by the validator function for SNR = 0.66, a candidate snake extracted from the phantom is still useful as illustrated in Figure 35.

Although the proposed algorithms are designed for the detection of mitochondria, it employs a Hessian-based ridge detector which is comparable to generic methods proposed for membrane detection (aforementioned in *Section 1*). According to the initial experiments, the utilized Hessian ridge detector (Equation 4) exhibits remarkable success compared to generic methods. Moreover, subsequent steps can be integrated to more sophisticated membrane detectors in order to enhance the accuracy.

The algorithm was additionally applied to a cryotomography (cryoET) dataset (ID: 6471) taken from EMDataBank [69]. This large dataset has very low SNR. Small

58

snippets (composed of 500 x 500 x 20 voxels) were cropped from the entire dataset. A sample tomogram (slice #: 310) from the dataset is illustrated in Figure 36.

Figure 37(a) depicts the initial snake locations and Figure 37(b) illustrates obtained large- (blue) and small-scale (red) curves. The final segmentation is shown in Figure 37(c). The method was able to detect and segment the mitochondrion by using the same parameter set given in Table 2. Figure 38 illustrates a segmentation example such that a successfully extracted region was eliminated by the validator function due to lack of small-scale curves inside the extracted shape (low E_{crista}).

SNR = ∞	SNR = 20	SNR = 10	SNR = 4	SNR = 2

SNR = 1.33	SNR = 1.0	SNR = 0.80	SNR = 0.66	SNR = 0.5
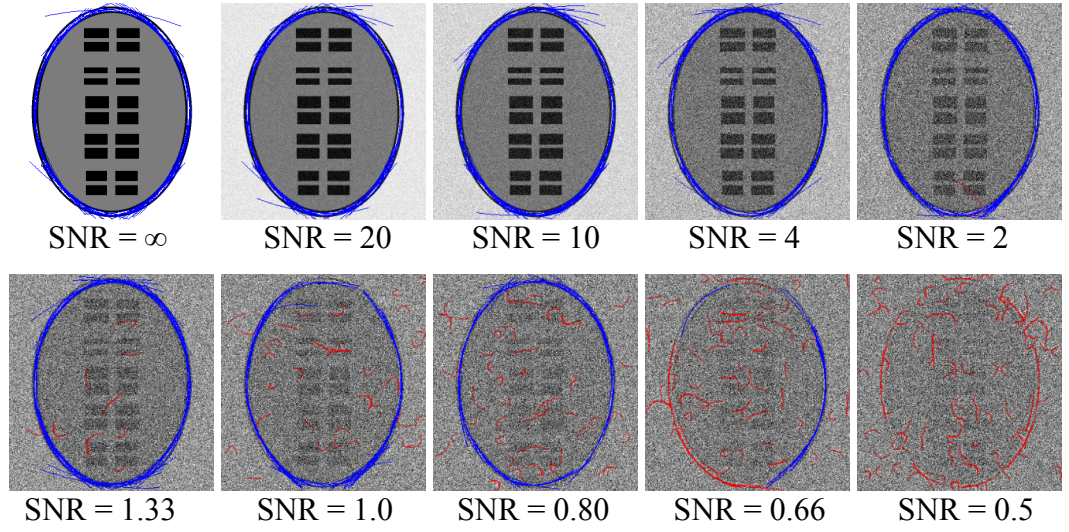
Figure 32: Curve fitting results extracted from LFREM (blue) and HFREM (red). Reprinted from [58].

SNR = ∞	SNR = 20	SNR = 10	SNR = 4	SNR = 2

SNR = 1.33	SNR = 1.0	SNR = 0.80	SNR = 0.66
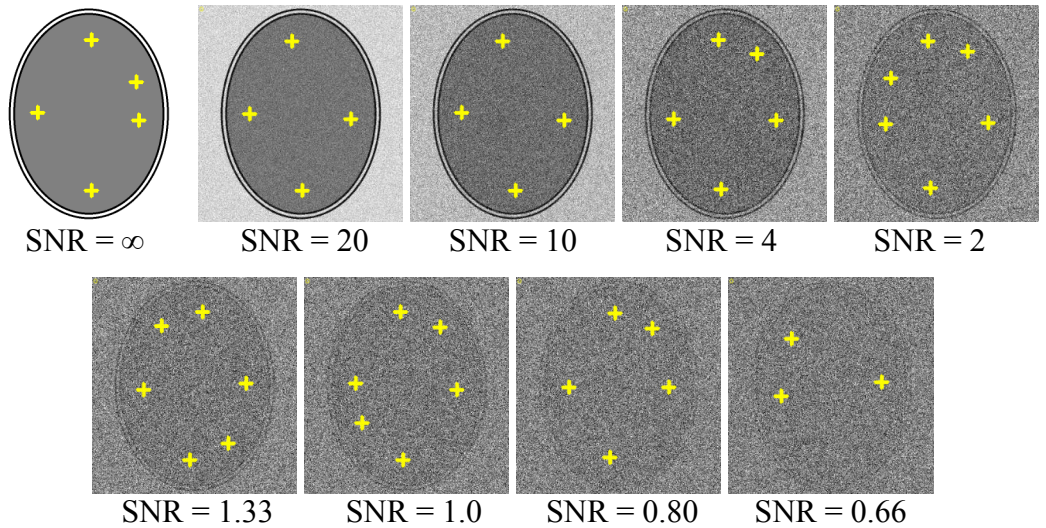
Figure 33: Auto-generated snake initial points (failed for SNR ≤ 0.5). Reprinted from [58].
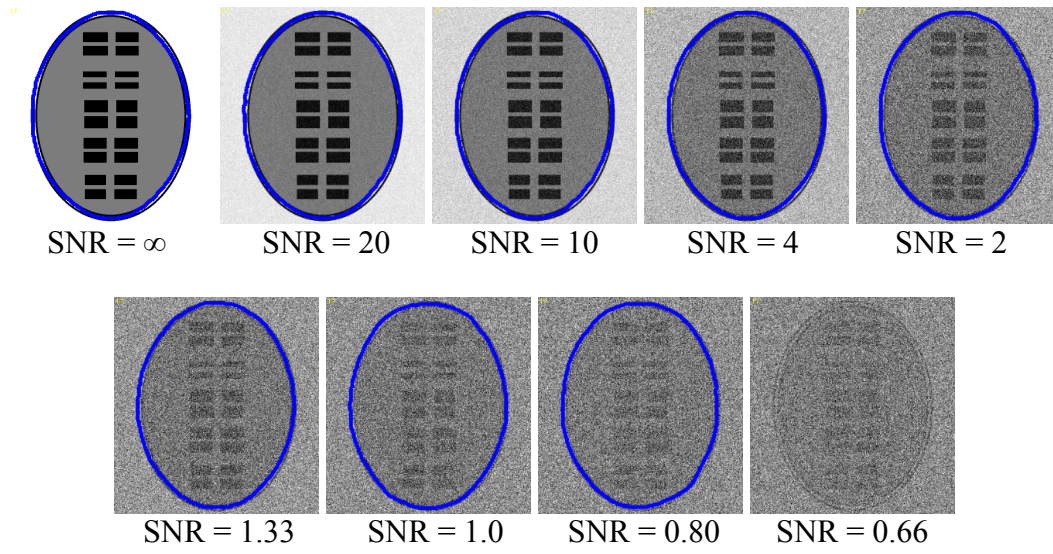
Figure 34: Segmentation results (Candidate contour for SNR = 0.66 was filtered by validator function due to weak boundary energy). Reprinted from [58].
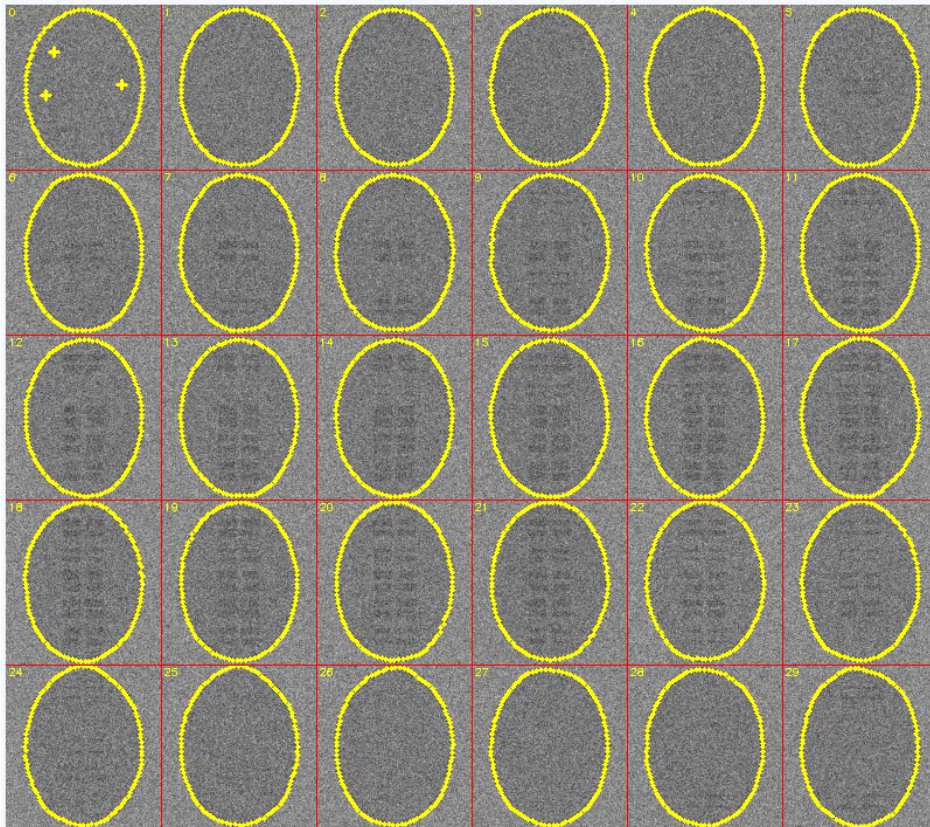
Figure 35: A candidate snake extracted from a 30 slice-range of the phantom (SNR = 0.66). Reprinted from [58].
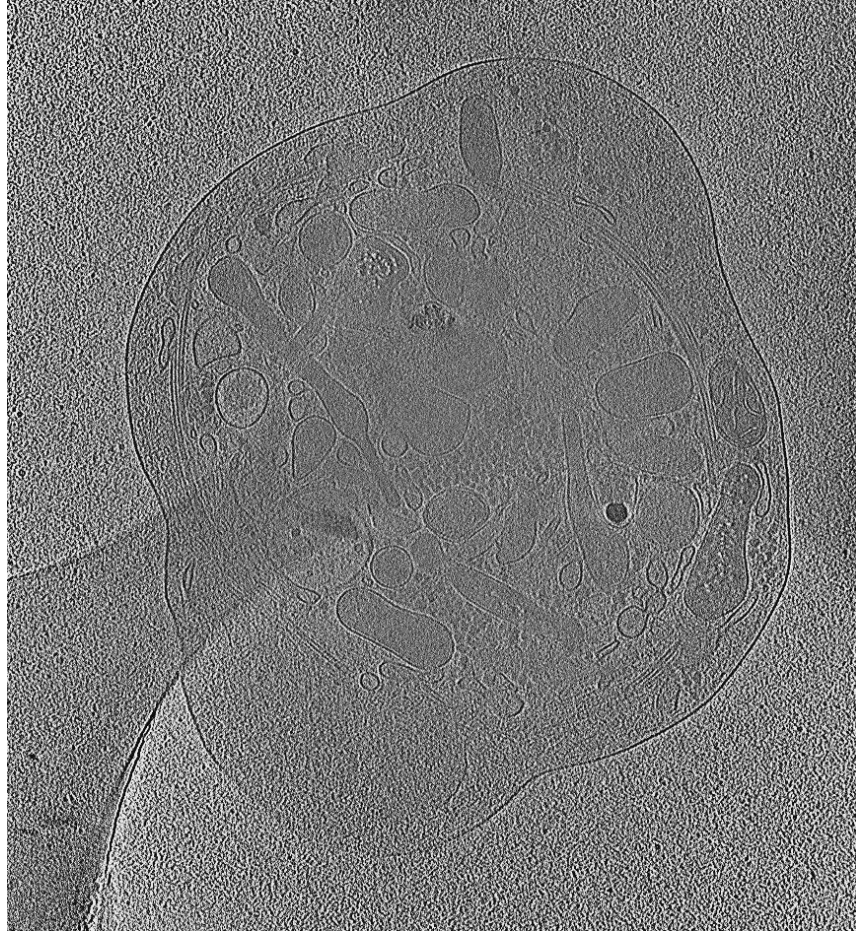
Figure 36: A tomogram (slice #: 310) from a cryotomography dataset
(EMDataBank ID: 6471)

(a)	(b)	(c)
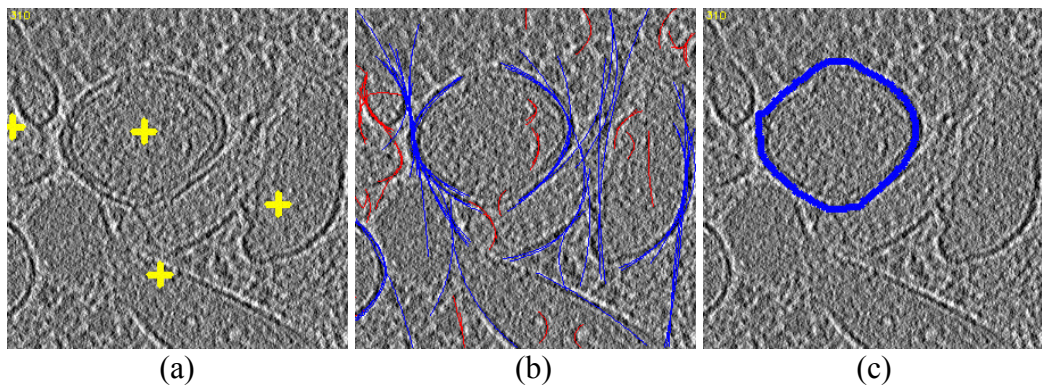
Figure 37: (a) A cropped section from the dataset referred to in Figure 36 showing
the snake initial points; (b) Curve fitting results obtained from LFREM (blue) and
HFREM (red); (c) Final segmentation result. Reprinted from [58].
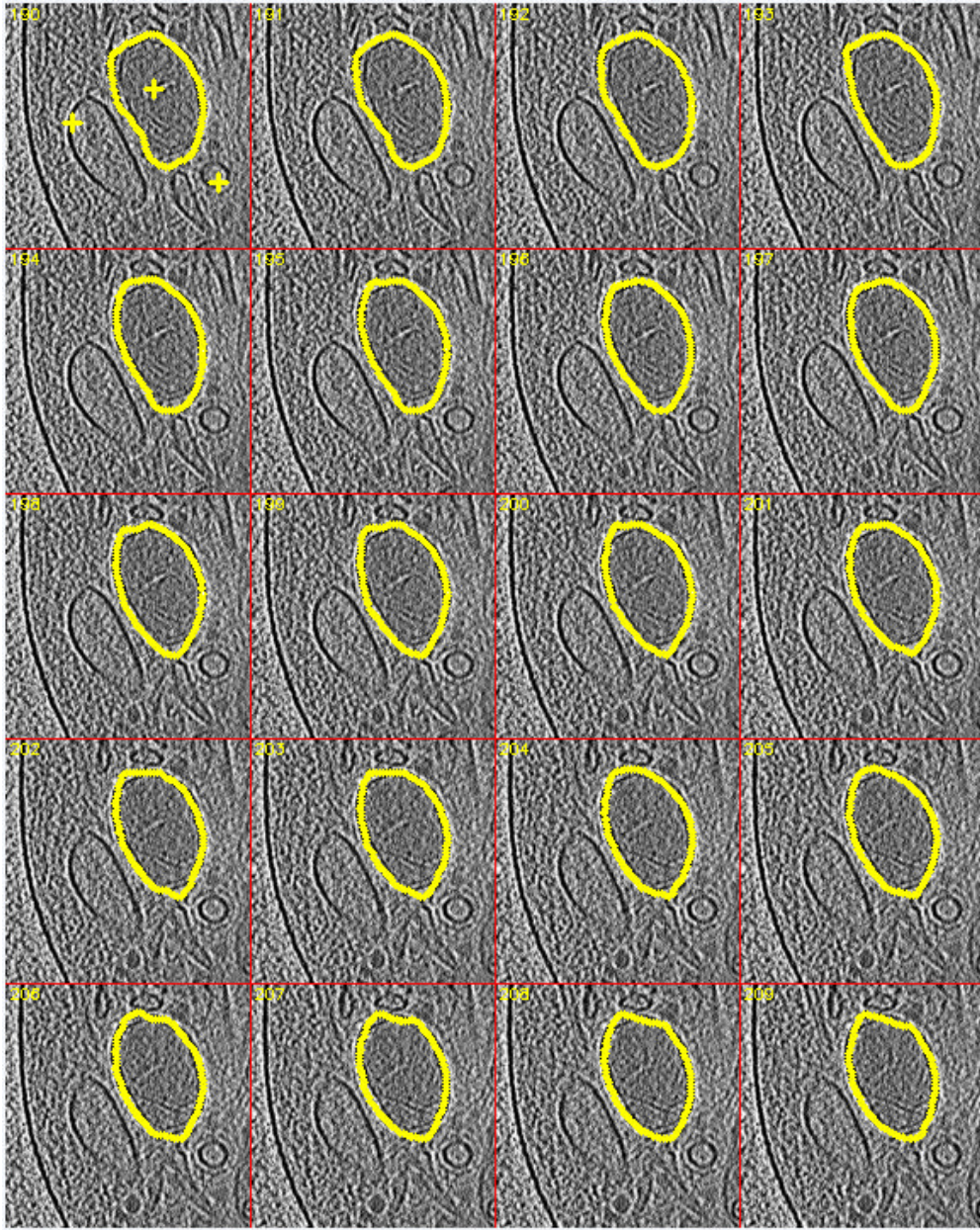
Figure 38: A candidate snake extracted from 20 slices taken from the dataset. The top-left picture shows the snake initial points. The extracted shape was refused by the validator function due to weak region (crista) energy (E_{crista}). Reprinted from [58].

CHAPTER 5

CONCLUSION AND DISCUSSION

5.1. Summary

In this study, 2D and 3D detection and segmentation of both fully and partially seen mitochondria from TEM datasets were investigated. The proposed method aims to extract mitochondrial peripheral membrane. The algorithm starts with the preprocessing step. In this step, resampling, smoothing and auto-contrast adjustment are applied to the input image. Then, a Hessian-based ridge detector evaluates membrane strength. The summation of local energy within two windows with different size is calculated to generate energy maps. The subsequent step is the parabolic arc fitting operation in which the energy maps are used to determine the segments of mitochondrial peripheral membranes and cristae. Then, the obtained curves are utilized in a snake algorithm which extracts candidate segmentation regions. Finally, the results are refined by a validator function.

5.2. Discussion

Although there are several attempts for computerized segmentation of mitochondria, this problem has not been solved satisfactorily yet due to multifarious appearance of mitochondria based on the preparation of specimens, cell type, and health condition. In this study, challenging datasets having a cluttered arrangement of mitochondrial membranes (boundary membranes and cristae) were preferred since the main problem is high throughput automatic and accurate cristae segmentation. It is worthy of note that automatic segmentation of images for other types (in which mitochondrial regions show dark blob-like patterns) is a much simpler problem since intensity-based features can be distinctive as addressed by the previous studies.

The non-mitochondrion specific studies in literature require hand manipulation in intermediate steps such as initialization of algorithm or manual filtering. Under such conditions, it was shown that these methods can be successful at the segmentation of peripheral and crista membranes of mitochondria. However, a low level intervention is not desired since the user needs experience to know the behavior of image processing algorithms. The mitochondrion specific methods in the literature are designed to work on condensed mitochondria and thus, they are not competent at segmenting peripheral membranes from the images as in the datasets collected for this study. On the other hand, generic membrane segmentation methods are used to extract

all kind of membrane-like objects and do not provide separation and recognition of sub-cellular structures.

In order to accomplish a successful segmentation, the proposed method are equipped with several procedures which utilize both low- and mid-level features. Without building such a sophisticated mechanism, it is not reasonable to expect a spectacular performance from a single step procedure involving a basic segmentation algorithm. Indeed, each step of the proposed system has a positive contribution to the performance. Hence, simple variants of segmentation methods such as watershed, Hough transform or even snakes utilized in the system are also inadequate to achieve a good segmentation quality. Snakes were preferred in this study because of their gap-compensating property. However, performance of snakes or watersheds based on the gradient of input image (as applied in standard usage) is fairly poor since the model is highly attracted by cristae arrangements. Hough transform, on the other hand, is useful (as employed in the preliminary study) but requires an eligible model to detect mitochondria. The ellipse model is proficient to a certain extent since not all mitochondria are in ellipse-shape. The 3D detection is also another challenging issue due to the number of model parameters which may be infeasible from the computation perspective.

The 2.5D snake model achieves a significant increase in precision while keeping recall stable. Moreover, detection accuracy of 2D model does not guarantee the convenience of 3D segmentation. In some cases, 2D snake boundaries extracted from the neighboring tomograms appears valid but discordant so that the segmentation is not stable along the z-direction. For 2.5D snakes, on the other hand, an appreciable number of acceptable slices must be achieved to assume that a 2.5D snake is valid. Otherwise, the validator function would refuse the whole shape. Hence, 2D snakes which perform better whereas 2.5D method fails causes an illusory upswing in recall. Note that a high recall in the 2D model does not mean a proper 3D segmentation. On the other hand, the recall performance of 2.5D model can be increased by tuning the algorithm the T_V parameter (see Figure 29(a)).

Snake initialization process described in *Section 3.2.2* utilizes parabolic arcs as an indication to the presence of mitochondria. Since large-scale curves are obtained mostly on elongated membranes such as peripheral membranes, snakes are initialized near such curves. This approach is expected to decrease false positive rates as well as computation time compared to random initialization strategy. Although the validator function aims to eliminate false positives, it is reasonable to input false detections to the validator function at low rates.

Specifying z-thickness (k) of the snake is another remarkable issue. The curves pertaining to different slices is not effectively utilized if the snake is not sufficiently thick (i.e. contains only a few slices). On the other hand, the snake partially converges if it is too thick such that the z-range of the snake exceeds the length of the target

mitochondrion. Hence, the segmentation may be refused by the validator function in this case. Segmentation can be performed in all slices by repeating the whole process for consecutive sections of dataset by adjusting a moderate thickness even if the mitochondrion is longer than the snake thickness. Figure 26(a) exhibits an example for resulting four snakes for $k = 20$. As a drawback, transitions between the bottom and top slices of the sections may not be smooth in some cases. To solve this problem, the snake algorithm can be re-executed with total z-thickness to segment the entire mitochondrion as shown in Figure 26(b).

The evaluation technique for the detection accuracy described in *Section 4.2* aims to reveal the ability of the algorithm to detect and separate mitochondria from each other. Figure 39 illustrates potential segmentation boundaries. The detected shape obtained by the snake method and ground truth boundary of mitochondria are illustrated as dashed and solid lines respectively. Contributions of these regions to precision and recall are discussed in Table 8.

The parameter set given in Table 2 may require a revision for low SNR conditions. For example, the validator function rejected all candidate shapes for SNR = 0.66 due to insufficient boundary energy. Nevertheless, the extracted contour was indeed useful as shown in Figure 35. In order to handle such cases, the user may be prompted to use alternative parameter sets arranged to deal with low SNR conditions in semi-automatic systems. A further discussion for system parameters is available in *Section 5.3*.

The cryoET datasets rarely inhabited by mitochondria may necessitate an improved preprocessing step that emphasizes the double membranes in order to achieve a good precision performance. The validation process rejects the most of the segmented regions due to weak boundary and region energy for the current parameter set. Hence, revision of the parameter set is another choice for cryoET datasets.

5.3.   Parameter Analysis

The effect of different parameter values to the behavior of the proposed system to were analyzed and discussed for each step of the algorithm below:

i.   **Preprocessing:** The preprocessing parameter values presented in Table 2 were experimented for both high and low contrast images. Good and enduring outcomes were attained. In order to remove only extreme intensity values, the histogram cut parameter of auto-contrast adjustment step should be lowered as small as possible since high threshold may lead to data loss. Many parameters of the system (especially validation parameters) are defined in terms of spatial distance. Hence, the resampling process is useful to ease parameter tuning by converting the pixel size to a fixed value. A pixel size of 2 nm appears to be sufficient to visualize membranes in detail. In the conducted experiments, the

— Ground truth
----- Detected shape

(a)   (b)   (c)   (d)   (e)   (f)   (g)   (h)
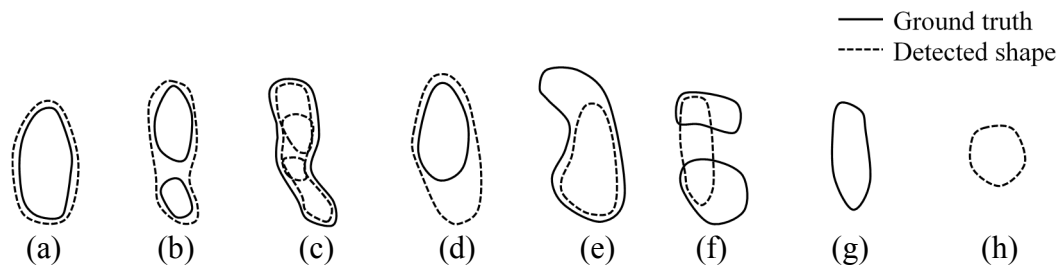
Figure 39: Potential segmentation and mitochondria boundaries.

Table 8: Description of the shapes given in Figure 39 and the corresponding contributions to precision and recall.

Shape	Description	Contribution
Figure 39(a)	Mitochondrion is segmented by a single snake.	The contribution to precision and recall depends on segmentation accuracy.
Figure 39(b)	A single snake surrounds multiple mitochondria.	Recall is contributed by the area of intersection of the best match mitochondrion. Precision is weakly contributed due to size of snake.
Figure 39(c)	Mitochondrion is segmented by multiple snakes in collaboration.	The contribution to precision and recall depends on segmentation accuracy of the region obtained by union of snakes.
Figure 39(d)	Mitochondrion is covered by a large snake.	Maximum contribution to recall. Precision is weakly contributed due to size of snake.
Figure 39(e)	Mitochondrion is partially segmented.	Maximum contribution to precision. Recall is weakly contributed due to size of snake.
Figure 39(f)	An awkward segmentation of multiple mitochondria by a single snake.	Recall is weakly contributed due to small intersection of the best match. Contribution to precision is expected to be even weaker since the rest of snake is outside of the best match.
Figure 39(g)	No snake on mitochondrion (false negative)	No contribution to precision or recall.
Figure 39(h)	Snake segments some region other than mitochondria (false positive).	No contribution to precision or recall.

effect of ridges associated to non-membrane structures were reduced by the bilateral filtering. This process was able to dilute the noise without removing weak membrane when the size parameter of spatial filtering kernel was between 30 and 60 nm. However, values lower than 30 nm triggered extraction of false positive curves on cristae. On the contrary, too large kernels precipitated the loss of true curves. The gray deviation parameter yielded a reasonable degree of smoothing for background and membranes when it was adjusted to 0.1–0.2 considering that the gray values are normalized between 0 and 1. Higher values precipitated smoothing of the edges pixels located between background and membrane.

ii. **Ridge detection:** Gaussian derivatives are able to detect membranes when the sigma parameter are adjusted according to membrane thickness. Hence, this parameter should be arranged proportional to the expected thickness of mitochondrial membrane (4–6 nm). Extracted ridges were relatively strong in the experiments when it is set to 2–3 nm (half of membrane thickness).

iii. **Energy mapping:** The double membrane structure of mitochondria should be covered by the window of energy mapping step in order to distinguish cristae from the peripheral membranes. A robust detection is achieved when the total energy within the window is doubled for double membranes (compared to single). Therefore, the ω parameter can be set to a value up to the maximum thickness of the double membrane (~48 nm). Considering the distance among potential cristae membranes (that show double membrane motif), the average double membrane thickness (~30 nm) was preferably used as the ω parameter in the experiments. In case of crista detection, the window size should be adjusted to include a single membrane (>6 nm). However, it should be kept below the minimum expected thickness of a double membrane (<18 nm) to avoid strengthening effect of the double membranes.

iv. **Curve fitting:** Experiments indicate that utilizing local maxima of LFREM/HFREM having at least 30-50% of the maximum energy yield a stable curve fitting on both crista and peripheral membranes by avoiding false positives on non-membrane structures. Reasonably high values of update parameters τ_x, τ_y and τ_h assure the avoidance from local maxima of the energy function $E(\Omega)$. On the other hand, extremely high values may lead to extraction of distinct membranes by a single curve. According to experiments, arranging these parameters around 4–8 nm yields the best results.

v. **Curve filtering:** Curve filtering parameters (i.e. arc-length and curve energy thresholds) were tuned empirically to eliminate the most of the unwanted curves detected at irrelevant locations while preserving large- and small- scale curves at the peripheral membrane of mitochondria and cristae. Note that the window size (ω) (used in the energy mapping) affects the curve energy and

length. Thus, it is reasonable to tune these thresholds by searching from values that were scaled linearly proportional to ω when it is necessary to modify empirically. In general, acceptable results were introduced when recommended adjustments in Table 2 were used within a range of ±70%.

vi. **Snake-based shape extraction:** This step is not delicate to small alterations in weights of the snake model (w_a, w_{at}, w_b, w_{bt}, w_c, w_d, w_{az}, w_{bz}). The parameter arrangements presented in Table 2 do not necessitate additional tuning depending on the dataset or mitochondria morphology. Nevertheless, the ratio of weights with respect to each other is a substantial property. It is easier to tune the weight parameters by assigning a fixed value (i.e. 1.0) to the tension weights (w_a, w_{at}). Gap filling capability and false positive tolerance were increased by the stiffness of the snake according to the experimental study. Hence, the curvature weights (w_b, w_{bt}) were specified by following a strategy satisfying w_b, $w_{bt} \gg w_c$, w_d. Since the internal energy of 2.5D additionally calculated along the z-axis, the corresponding external energy weight (w_c) was doubled for 2.5D snakes. On the other hand, a wide range of values (i.e. $0.5, 1.0, 1.5 \dots 3.0$) should be scanned by the inflation weight (w_d) considering potential false-positive large-scale curves and diversity in membrane strength. However, the step size in w_d can be set to an even smaller value to compensate the membrane weakness and the effect of false-positive curves although the computation time would be increased. Considering that the circumference of the snake slice is much larger than the z-thickness, tension and curvature weights associated to the z-axis (w_{az}, w_{bz}) should be adjusted to a value greater than w_{at} and w_{bt} in order to improve the effect of neighboring slices.

vii. **Snake initialization:** Snake may fail growing if it is initialized too close to parabolic arc since external forces may be too strong compared to inflation force. The distance (r) between the initial point and the vertex of arc should be adjusted in conformity with weight parameters of snake model. In the experiments, boundary of snakes properly evolved while $r > 20$ nm with the suggested weight settings. The size of cluster neighborhood (ε) and upper limit of r should be adjusted with respect to the minimum expected size of mitochondrial cross-section (~250 nm). Considering a small mitochondria, ε was set to 100 nm. Clusters may be affected by nearby cue points pertaining to other mitochondria for larger values. The threshold concerning the minimum number of cue points contained in a cluster was specified according to the z-thickness of the model in the experiments. Recall improves indirectly by the utilization of small values by augmenting initializations. However, the clusters are more reliable when supported by more cue points. Acceptable results were attained when this threshold was set to 1.0–2.0 times the z-thickness.

viii. **Validator function:** The parameters of validator function were roughly adjusted by taking the morphology of mitochondria into consideration. The

parameters T_{major}, T_{minor}, T_{area_min}, T_{area_max} are determined by physical limits of mitochondria to supply an indelicate constraint for candidate regions. However, they can be tuned properly if mitochondria of a particular size are in interest. The curvature parameters (T_{curv_max} and T_{curv_ave}) are upper-limits for radial displacement of the outer membrane. These parameters regulate the removal of regions according to degree of tortuosity and can be lowered in order to detect only a globular mitochondrion if necessary. The energy parameters (T_{energy_b} and T_{energy_c}) were kept as small as possible to include mitochondria with weakly appearing membranes and rarely populated cristae. Although validation parameters may be refined in accordance with the input dataset, it must be done by considering overfitting problems.

ix. ***Post-processing***: In the conducted experiments, the merging threshold arranged between 15% and 35% yielded acceptable results. This operation can merge separate mitochondria erroneously if the threshold is too low. On the contrary, snakes may not be merged in case of utilization of high threshold causing an over segmentation problem.

5.4. Limitations

A flawless segmentation still requires a manual effort. Thus, augmenting the automatized algorithm developed in this study with some semi-automatic tools can reduce the manual effort. These tools perform several operations such as manual validation of false negatives, rejection of false positives, semi-automatic merging and splitting and manual boundary correction by dragging [70]. The user can interfere in the validation process to label correct or incorrect detections in order to reduce false-negative and false-positive error. The segmentation can be rapidly refined by initiating auto-splitting mechanism on erroneously auto-merged regions by taking basic commands from the user. Similarly, over-segmentation issues can be dissipated by the utilization of merging tools. Fortunately, the user interaction can be realized in real-time since these tools will work on pre-extracted regions. In case of inadequate detection, these tools additionally allow the user to execute the snake algorithm at a suitable location. The defective boundary may be dragged to the correct location by the user in case of a partially inconsistent segmentation.

The implementations of algorithms are not fully optimal yet. Hence, the system is not currently able to respond to users' commands in real time. Fortunately, a tremendous speed-up can be gained by parallelizing the algorithms developed since they are highly adaptable to be executed on a GPU.

Hessian ridge detector fails to detect membranes of condensed mitochondria (see Figure 27(f)). However, Hessian matrix (Equation 3) can be replaced with a tensor matrix which is based on the first derivative to detect edge features instead of ridges.

69

Additionally, it is advantageous to utilize the first derivative since it is less sensitive to noise.

The snake boundary generated by the proposed algorithm passes through mid-locations of double membranes of mitochondria since LFREM is used for the formulation of the external energy terms. The total ridge energy within a wide neighborhood (30 nm) is stored in this energy map which usually covers both inner and outer membranes. Therefore, the energy is maximized at the mid-point between these membranes. The system is expected to produce a perfect segmentation since parabolic arcs roughly fit into membranes. However, the segmentation accuracy can be remarkably improved by utilizing techniques described in a study by Jorstad and Fua [71] or a modified live-wire algorithm used in the preliminary study [52] in order to refine the segmentation.

5.5.   Future Work

Curve fitting and snake algorithms will be parallelized on GPU in the future. By the end of the second quarter of 2016, the first release of current software is planned to be made accessible. Additionally, a user-friendly application will be built as soon as parallelization and optimization of algorithms are complete.

Since the auto-merging algorithm operates based on only intersectional volume of overlapping regions, it may produce erroneously merged outputs. Such composed regions may not satisfy all validation criteria. After auto-merging process, the outcomes can be validated again to ensure that the final region satisfies desired properties. Thus, false-positives can be reduced by revalidating auto-merged regions.

The feature extraction operators can be extended to 3D to provide a better membrane detection. The proposed 2D ridge detector is not capable of extracting membranes passing parallel to tomograms. Therefore, it is reasonable to enhance the membrane detection procedure by utilizing 3D Hessian matrix. In this case, 2D parabolic arc model must be extended to cover 3D geometrical objects as well. Surface patch models such as paraboloids (including hyperbolic paraboloids) appears to be eligible to segment peripheral and crista membranes of mitochondria in 3D. Employment of a fully 3D snake models then will be feasible once the 3D features are extracted.

The validation procedure in the proposed system is a dichotomy problem in pattern recognition methods. Particularly, each extracted region corresponds to a point in a hyper-rectangular region in the parameter space. On the other hand, machine learning methods are capable of classifying objects by linear and non-linear combinations of validation descriptors. For future work, the validation function can be improved by utilization of the validation descriptors based on supervised learning techniques in order to construct a robust validation mechanism.

In addition, development and implementation of a software package involving the proposed system integrated into aforementioned semi-automatic segmentation tools and the establishment of cristae segmentation methods can be considered for future work.

REFERENCES

[1]   H. M. McBride, M. Neuspiel, and S. Wasiak, "Mitochondria: More Than Just a Powerhouse," *Current Biology*, vol. 16, no. 14. 2006.

[2]   I. E. Scheffler, *Mitochondria: Second Edition*. Hoboken, NJ, USA: John Wiley & Sons, Inc., 2007.

[3]   F. Burté, V. Carelli, P. F. Chinnery, and P. Yu-Wai-Man, "Disturbed mitochondrial dynamics and neurodegenerative disorders.," *Nat. Rev. Neurol.*, vol. 11, no. 1, pp. 11–24, 2014.

[4]   S. Franco-Iborra, M. Vila, and C. Perier, "The Parkinson Disease Mitochondrial Hypothesis: Where Are We at?," *Neurosci.*, p. 1073858415574600, 2015.

[5]   X. Wang, W. Wang, L. Li, G. Perry, H. Lee, and X. Zhu, "Oxidative stress and mitochondrial dysfunction in Alzheimer's disease," *Biochim. Biophys. Acta - Mol. Basis Dis.*, vol. 1842, no. 8, pp. 1240–1247, 2014.

[6]   T. G. Frey and C. A. Mannell, "The internal structure of mitochondria," *Trends Biochem. Sci.*, vol. 25, no. 7, pp. 319–324, 2000.

[7]   C. A. Mannella, "Structural diversity of mitochondria: Functional implications," in *Annals of the New York Academy of Sciences*, 2008, vol. 1147, pp. 171–179.

[8]   M. Zick, R. Rabl, and A. S. Reichert, "Cristae formation-linking ultrastructure and function of mitochondria," *Biochimica et Biophysica Acta - Molecular Cell Research*, vol. 1793, no. 1. pp. 5–19, 2009.

[9]   T. Róg, M. S. Hector, N. Munck, M. Orešič, M. Karttunen, and I. Vattulainen, "Role of cardiolipins in the inner mitochondrial membrane: Insight gained through atom-scale simulations," *J. Phys. Chem. B*, vol. 113, no. 11, pp. 3413–3422, 2009.

[10]   G. Perkins, C. Renken, M. E. Martone, S. J. Young, M. Ellisman, and T. Frey, "Electron tomography of neuronal mitochondria: three-dimensional structure and organization of cristae and membrane contacts.," *J. Struct. Biol.*, vol. 119, no. 3, pp. 260–272, 1997.

[11] G. A. Perkins, J. Y. Song, L. Tarsa, T. J. Deerinck, M. H. Ellisman, and T. G. Frey, "Electron tomography of mitochondria from brown adipocytes reveals crista junctions," *J. Bioenerg. Biomembr.*, vol. 30, no. 5, pp. 431–442, 1998.

[12] G. A. Perkins, C. W. Renken, I. J. van der Klei, M. H. Ellisman, W. Neupert, and T. G. Frey, "Electron tomography of mitochondria after the arrest of protein import associated with Tom19 depletion," *Eur. J. Cell Biol.*, vol. 80, no. 2, pp. 139–150, 2001.

[13] G. a Perkins, M. H. Ellisman, and D. a Fox, "Three-dimensional analysis of mouse rod and cone mitochondrial cristae architecture: bioenergetic and functional implications.," *Mol. Vis.*, vol. 9, no. February, pp. 60–73, 2003.

[14] T. G. Frey, G. a Perkins, and M. H. Ellisman, "Electron tomography of membrane-bound cellular organelles.," *Annu. Rev. Biophys. Biomol. Struct.*, vol. 35, pp. 199–224, 2006.

[15] N. V. Dudkina, R. Kouril, K. Peters, H. P. Braun, and E. J. Boekema, "Structure and function of mitochondrial supercomplexes," *Biochimica et Biophysica Acta - Bioenergetics*, vol. 1797, no. 6–7. pp. 664–670, 2010.

[16] L. Reimer and H. Kohl, *Transmission Electron Microscopy Physics of Image Formation*, vol. 51. 2008.

[17] K. Sandberg, D. N. Mastronarde, and G. Beylkin, "A fast reconstruction algorithm for electron microscope tomography," *J. Struct. Biol.*, vol. 144, no. 1–2, pp. 61–72, 2003.

[18] J. Frank, *Electron tomography: Methods for three-dimensional visualization of structures in the cell*. 2006.

[19] K. M. Davies, B. Daum, V. a M. Gold, A. W. Mühleip, T. Brandt, T. B. Blum, D. J. Mills, and W. Kühlbrandt, "Visualization of ATP synthase dimers in mitochondria by electron cryo-tomography.," *J. Vis. Exp.*, no. 91, p. 51228, 2014.

[20] J. Harapin, M. Eibauer, and O. Medalia, "Structural analysis of supramolecular assemblies by cryo-electron tomography," *Structure*, vol. 21, no. 9, pp. 1522–1530, 2013.

[21] W. Denk and H. Horstmann, "Serial block-face scanning electron microscopy to reconstruct three-dimensional tissue nanostructure," *PLoS Biol.*, vol. 2, no. 11, 2004.

[22] V. Chavan, J. Willis, S. K. Walker, H. R. Clark, X. Liu, M. a Fox, S. Srivastava, and K. Mukherjee, "Central presynaptic terminals are enriched in ATP but the majority lack mitochondria.," *PLoS One*, vol. 10, no. 4, p. e0125185, 2015.

[23] A. A. Wanner, M. A. Kirschmann, and C. Genoud, "Challenges of microtome-based serial block-face scanning electron microscopy in neuroscience," *J. Microsc.*, vol. 259, no. 2, pp. 137–142, 2015.

[24] J. R. Kremer, D. N. Mastronarde, and J. R. McIntosh, "Computer visualization of three-dimensional image data using IMOD.," *J. Struct. Biol.*, vol. 116, no. 1, pp. 71–76, 1996.

[25] H. Nguyen and Q. Ji, "Shape-driven three-dimensional watersnake segmentation of biological membranes in electron tomography," *IEEE Trans. Med. Imaging*, vol. 27, no. 5, pp. 616–628, 2008.

[26] R. Narasimha, H. Ouyang, A. Gray, S. W. McLaughlin, and S. Subramaniam, "Automatic joint classification and segmentation of whole cell 3D images," *Pattern Recognit.*, vol. 42, no. 6, pp. 1067–1079, 2009.

[27] C. Bazán, M. Miller, and P. Blomgren, "Structure enhancement diffusion and contour extraction for electron tomography of mitochondria," *J. Struct. Biol.*, vol. 166, no. 2, pp. 144–155, 2009.

[28] P. Perona and J. Malik, "Scale-space and edge detection using anisotropic diffusion," *IEEE Trans. Pattern Anal. Mach. Intell*, vol. 12, no. 7, pp. 629–639, 1990.

[29] J. Weickert, "Anisotropic diffusion in image processing," *Image Rochester NY*, vol. 256, no. 3, p. 170, 1998.

[30] M. J. Black and G. Sapiro, "Edges as Outliers: Anisotropic Smoothing using Local Image Statistics," *Scale-sp. Theor. Comput. Vis.*, vol. 1682, pp. 259–270, 1999.

[31] C. Tomasi and R. Manduchi, "Bilateral Filtering for Gray and Color Images," *Int. Conf. Comput. Vis.*, pp. 839–846, 1998.

[32] R. S. Pantelic, G. Ericksson, N. Hamilton, and B. Hankamer, "Bilateral edge filter: Photometrically weighted, discontinuity based edge detection," *J. Struct. Biol.*, vol. 160, no. 1, pp. 93–102, 2007.

[33] F. Porikli, "Constant time O (1) bilateral filtering," *Comput. Vis. Pattern Recognition, 2008. CVPR 2008. IEEE Conf.*, no. 1, pp. 1–8, 2008.

[34] W. Jiang, M. L. Baker, Q. Wu, C. Bajaj, and W. Chiu, "Applications of a bilateral denoising filter in biological electron microscopy," *J. Struct. Biol.*, vol. 144, no. 1–2, pp. 114–122, 2003.

[35] J. H. Macke, N. Maack, R. Gupta, W. Denk, B. Schölkopf, and A. Borst, "Contour-propagation algorithms for semi-automated reconstruction of neural processes," *J. Neurosci. Methods*, vol. 167, no. 2, pp. 349–357, 2008.

[36] E. Jurrus, S. Watanabe, R. J. Giuly, A. R. C. Paiva, M. H. Ellisman, E. M. Jorgensen, and T. Tasdizen, "Semi-automated neuron boundary detection and nonbranching process segmentation in electron microscopy images," *Neuroinformatics*, vol. 11, no. 1, pp. 5–29, 2013.

[37] F. Daum, "Nonlinear filters: Beyond the kalman filter," *IEEE Aerosp. Electron. Syst. Mag.*, vol. 20, no. 8 II, pp. 57–68, 2005.

[38] S. C. Turaga, J. F. Murray, V. Jain, F. Roth, M. Helmstaedter, K. Briggman, W. Denk, and H. S. Seung, "Convolutional networks can learn to generate affinity graphs for image segmentation.," *Neural Comput.*, vol. 22, no. 2, pp. 511–538, 2010.

[39] R. J. Giuly, M. E. Martone, and M. H. Ellisman, "Method: automatic segmentation of mitochondria utilizing patch classification, contour pair classification, and automatically seeded level sets," *BMC Bioinformatics*, vol. 13, no. 1, p. 29, 2012.

[40] O. Ghita, J. Dietlmeier, and P. Whelan, "Automatic segmentation of mitochondria in EM data using pairwise affinity factorization and graph-based contour searching.," *IEEE Trans. Image Process.*, vol. 23, no. 10, pp. 4576–4586, 2014.

[41] A. Lucchi, K. Smith, R. Achanta, G. Knott, and P. Fua, "Supervoxel-based segmentation of mitochondria in em image stacks with learned shape features," *IEEE Trans. Med. Imaging*, vol. 31, no. 2, pp. 474–486, 2012.

[42] J. Dietlmeier, O. Ghita, H. Duessmann, J. H. M. Prehn, and P. F. Whelan, "Unsupervised mitochondria segmentation using recursive spectral clustering and adaptive similarity models.," *J. Struct. Biol.*, vol. 184, no. 3, pp. 401–408, 2013.

[43] M. Seyedhosseini, M. Sajjadi, and T. Tasdizen, "Image segmentation with cascaded hierarchical models and logistic disjunctive normal networks," in *Proceedings of the IEEE International Conference on Computer Vision*, 2013, pp. 2168–2175.

[44] A. Martinez-Sanchez, I. Garcia, and J. J. Fernandez, "A differential structure approach to membrane segmentation in electron tomography," *J. Struct. Biol.*, vol. 175, no. 3, pp. 372–383, 2011.

[45] A. Martinez-Sanchez, I. Garcia, and J. J. Fernandez, "A ridge-based framework for segmentation of 3D electron microscopy datasets," *J. Struct. Biol.*, vol. 181, no. 1, pp. 61–70, 2013.

[46] A. Martinez-Sanchez, I. Garcia, S. Asano, V. Lucic, and J. J. Fernandez, "Robust membrane detection based on tensor voting for electron tomography.," *J. Struct. Biol.*, vol. 186, no. 1, pp. 49–61, 2014.

[47] A. Bartesaghi, G. Sapiro, and S. Subramaniam, "An energy-based three-dimensional segmentation approach for the quantitative interpretation of electron tomograms," *IEEE Trans. Image Process.*, vol. 14, no. 9, pp. 1314–1323, 2005.

[48] K. Sandberg and M. Brega, "Segmentation of thin structures in electron micrographs using orientation fields," *J. Struct. Biol.*, vol. 157, no. 2, pp. 403–415, 2007.

[49] G. E. Murphy and G. J. Jensen, "Electron cryotomography," *BioTechniques*, vol. 43, no. 4. pp. 413–423, 2007.

[50] R. A. Ali, M. J. Landsberg, E. Knauth, G. P. Morgan, B. J. Marsh, and B. Hankamer, "A 3D image filter for parameter-free segmentation of macromolecular structures from electron tomograms," *PLoS One*, vol. 7, no. 3, 2012.

[51] C. Page, D. Hanein, and N. Volkmann, "Accurate membrane tracing in three-dimensional reconstructions from electron cryotomography data," *Ultramicroscopy*, vol. 155, pp. 20–26, 2015.

[52] E. U. Mumcuoglu, R. Hassanpour, S. F. Tasel, G. Perkins, M. E. Martone, and M. N. Gurcan, "Computerized detection and segmentation of mitochondria on electron microscope images," *J. Microsc.*, vol. 246, no. 3, pp. 248–265, 2012.

[53] S. F. Tasel, R. Hassanpour, E. U. Mumcuoglu, G. C. Perkins, and M. Martone, "Automatic detection of mitochondria from electron microscope tomography images: a curve fitting approach," in *SPIE Medical Imaging 2014*, 2014, vol. 9034, p. 903449.

[54] R. C. Gonzalez and R. E. Woods, *Digital Image Processing (3rd Edition)*. 2007.

[55] L. D. Cohen, "On active contour models and balloons," *CVGIP Image Underst.*, vol. 53, no. 2, pp. 211–218, 1991.

[56] W. a Barrett and E. N. Mortensen, "Interactive live-wire boundary extraction.," *Med. Image Anal.*, vol. 1, pp. 331–341, 1997.

[57] A. A. Amini, T. E. Weymouth, and R. C. Jain, "Using Dynamic Programming for Solving Variational Problems in Vision," *IEEE Trans. Pattern Anal. Mach. Intell.*, vol. 12, no. 9, pp. 855–867, 1990.

[58] S. F. Tasel, E. U. Mumcuoglu, R. Z. Hassanpour, and G. Perkins, "A validated active contour method driven by parabolic arc model for detection and segmentation of mitochondria," *J. Struct. Biol.*, vol. 194, no. 3, pp. 253–271, Mar. 2016.

[59] M. Kass, A. Witkin, and D. Terzopoulos, "Snakes: Active contour models," *Int. J. Comput. Vis.*, vol. 1, no. 4, pp. 321–331, 1988.

[60] I. Valdés, Y. Nomura, and Y. Mitsuya, "Equidistant Snakes : Accurate Irregular Shaped Contour Detection," in *Machine Vision Applications*, 1996, pp. 285–288.

[61] J. Stewart, *Calculus, concepts and contexts*. 1998.

[62] J. Ahlberg, "Active Contours in Three Dimensions," Linköping University, 1996.

[63] M. Ester, H. P. Kriegel, J. Sander, and X. Xu, "A Density-Based Algorithm for Discovering Clusters in Large Spatial Databases with Noise," in *Second International Conference on Knowledge Discovery and Data Mining*, 1996, pp. 226–231.

[64] M. E. Martone, A. Gupta, M. Wong, X. Qian, G. Sosinsky, B. Ludäscher, and M. H. Ellisman, "A cell-centered database for electron tomographic data," *J. Struct. Biol.*, vol. 138, no. 1–2, pp. 145–155, 2002.

[65] M. E. Martone, S. Zhang, A. Gupta, X. Qian, H. He, D. L. Price, M. Wong, S. Santini, and M. H. Ellisman, "The cell-centered database: a database for multiscale structural and protein localization data from light and electron microscopy.," *Neuroinformatics*, vol. 1, pp. 379–395, 2003.

[66] M. E. Martone, J. Tran, W. W. Wong, J. Sargis, L. Fong, S. Larson, S. P. Lamont, A. Gupta, and M. H. Ellisman, "The Cell Centered Database project: An update on building community resources for managing and sharing 3D imaging data," *J. Struct. Biol.*, vol. 161, no. 3, pp. 220–231, 2008.

[67]   D. Powers, "Evaluation: from precision, recall and F-measure to ROC, informedness, markedness and correlation," *J. Mach. Learn. Technol.*, vol. 2, no. 1, pp. 37–63, 2011.

[68]   J.-J. Fernández, A. F. Lawrence, J. Roca, I. García, M. H. Ellisman, and J.-M. Carazo, "High-performance electron tomography of complex biological specimens.," *J. Struct. Biol.*, vol. 138, pp. 6–20, 2002.

[69]   R. Wang, R. L. Stone, J. T. Kaelber, R. H. Rochat, A. M. Nick, K. V. Vijayan, V. Afshar-Kharghan, M. F. Schmid, J.-F. Dong, A. K. Sood, and W. Chiu, "Electron cryotomography reveals ultrastructure alterations in platelets from patients with ovarian cancer," *Proc. Natl. Acad. Sci.*, vol. 112, no. 46, p. 201518628, 2015.

[70]   M. Cocelli, "Semi-Automatic/User-Guided Segmentation of Mitochondria on Transmission Electron Microscopy Images," Middle East Technical University, 2015.

[71]   A. Jorstad and P. Fua, "Refining mitochondria segmentation in electron microscopy imagery with active surfaces," *Lect. Notes Comput. Sci. (including Subser. Lect. Notes Artif. Intell. Lect. Notes Bioinformatics)*, vol. 8928, no. EPFL-CONF-201868, pp. 367–379, 2015.

[72]   P. Cignoni, M. Callieri, M. Corsini, M. Dellepiane, F. Ganovelli, and G. Ranzuglia, "MeshLab: an Open-Source Mesh Processing Tool," in *Sixth Eurographics Italian Chapter Conference*, 2008, pp. 129–136.

APPENDIX A: DYNAMIC STEP SIZE ON PARABOLIC ARC

In order to have a smooth curve, the size Δt is arranged to locate equidistant points on the parabolic arc and it depends on t. As shown in Figure 40, equidistant points are located by an approximation with a fixed distance S on the tangent line. The tangent line of the parabolic arc satisfies $\Delta k = \Delta t(2at + b)$ and $\Delta t^2 + \Delta k^2 = S^2$. By substitution of the former equation into the latter and after suitable arrangements, as in Equation 10, Δt is found as $S/\sqrt{1 + (2at + b)^2}$.
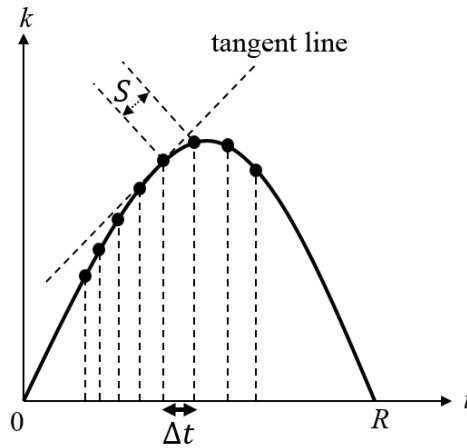

Figure 40: Equidistant points on a parabolic arc and step size on t-axis.

APPENDIX B: DERIVATION OF INTERNAL ENERGY UPDATE TERM

There are several approaches available to derive Equation 20 from Equation 15. Since the solutions are distracting and complicated, many papers involving snakes simply use the solution and omit the intermediate steps. A solution for Equation 20 is described below.

Since ∇E_{snakes} involves integration, the linearity property leads to the integration:

$$E_{\text{int}} = \int \frac{1}{2}\left(w_a \left\|\frac{dv}{dt}\right\|^2 + w_b \left\|\frac{d^2v}{dt^2}\right\|^2\right) dt.$$

For simplicity, it can be denoted as $E(v) = \frac{1}{2}(\alpha\|v'\|^2 + \beta\|v''\|^2)$. For a small change δv in v, one can substitute $v + \delta v$ to v to obtain:

$$E(v + \delta v) = \frac{1}{2}(\alpha\|v' + \delta v'\|^2 + \beta\|v'' + \delta v''\|^2).$$

Consider the following equation:

$$\|v + \delta v\|^2 = v \cdot v + 2v \cdot \delta v + \delta v \cdot \delta v$$

where $\delta v \cdot \delta v$ is negligible. Hence, the following approximation is obtained:

$$\|v + \delta v\|^2 \approx v^2 + 2v \cdot \delta v$$

Assuming that E is linear for the small interval, the formulation is simplified by using above approximation to:

$$E(v) + E(\delta v) = \int \left(\frac{\alpha}{2}(v'^2 + 2v' \cdot \delta v') + \frac{\beta}{2}(v''^2 + 2v'' \cdot \delta v'')\right) dt$$

Again using linearity property, it can be written as:

$$E(v) + E(\delta v) = \frac{\alpha}{2}\int (v'^2 + 2v' \cdot \delta v')dt + \frac{\beta}{2}\int (v''^2 + 2v'' \cdot \delta v'')dt$$

Now, subtracting $E(v)$ from above equation yields:

$$E(\delta v) = \alpha \int v' \cdot \delta v' dt + \beta \int v'' \cdot \delta v'' dt$$

This equation is further simplified by applying integration by parts once to the first term and twice to the second term and after some factorization, one can obtain:

$$E(\delta v) = -\alpha \int v'' \cdot \delta v dt + \beta \int v'''' \cdot \delta v dt$$

$$E(\delta v) = \int (-\alpha v'' + \beta v'''') \, \delta v dt$$

In the above equation, $(-\alpha v'' + \beta v'''')$ provides the direction of the gradient. In the steepest descent algorithm, the update operation should be arranged as $v \leftarrow v - \Delta v$ in order to minimize energy.

APPENDIX C: APPROXIMATION OF LOCAL CURVATURE

κ_L is an approximation of the local curvature defined in Equation 25. Formally, the curvature is the magnitude of the difference vector $\mathrm{d}\vec{\mathbf{T}}$ per unit length where $\vec{\mathbf{T}}$ is the unit tangent vector. The tangent vector can be approximated by $d(t) = v(t+1) - v(t)$ where v denotes (x, y) coordinates of the point indicated by t on the snake boundary. Hence, the tangent vector $d(t)$ is a vector from the point $v(t)$ to the next point. It is used as an approximation for the tangent of point "A" that is placed on the halfway between $v(t)$ and $v(t+1)$. Then, the term $d(t)/\|d(t)\|$ provides a unit vector which is an approximation for $\vec{\mathbf{T}}$. Similarly, $d(t-1)/\|d(t-1)\|$ gives unit tangent vector $\vec{\mathbf{T}}$ for the point "B" placed on the halfway between $v(t-1)$ and $v(t)$. Then, $\mathrm{d}\vec{\mathbf{T}}$ is given by:

$$\mathrm{d}\vec{\mathbf{T}} = \frac{d(t)}{\|d(t)\|} - \frac{d(t-1)}{\|d(t-1)\|}$$

The distance $\mathrm{d}l$ travelled between the points "A" and "B" is given by $\frac{\|d(t)\|}{2} + \frac{\|d(t-1)\|}{2}$. Dividing $\mathrm{d}\vec{\mathbf{T}}$ by $\mathrm{d}l$ yields:

$$\frac{\mathrm{d}\vec{\mathbf{T}}}{\mathrm{d}l} = \frac{2}{\|d(t)\| + \|d(t+1)\|}\left(\frac{d(t)}{\|d(t)\|} - \frac{d(t-1)}{\|d(t-1)\|}\right)$$

The local curvature is approximated by the magnitude of this vector:

$$\kappa_L(t) \cong \frac{2}{\|d(t)\| + \|d(t+1)\|}\left\|\frac{d(t)}{\|d(t)\|} - \frac{d(t-1)}{\|d(t-1)\|}\right\|$$

CURRICULUM VITAE

PERSONAL INFORMATION

Surname, Name: Taşel, Faris Serdar
Nationality: Turkish (TC)
Date and Place of Birth: August 27, 1981, Afyonkarahisar
Marital Status: Married
Phone: +90 312 284 45 00
Fax: +90 312 286 40 78
E-mail: fst@cankaya.edu.tr

EDUCATION

Degree	Intuition	Year of Graduation
M.Sc.	Çankaya Üniv., Computer Engineering	2008
B.Sc.	Çankaya Üniv., Computer Engineering	2004
High School	İzmir Atatürk Lisesi, İzmir	1999

WORK EXPERIENCE

Year	Place	Enrollment
2012 – Present	Çankaya Üniv.	Lecturer
2005 – 2012	Çankaya Üniv.	Research Assistant

LANGUAGES

Turkish (Native), English (Advanced), German (Elementary)

PUBLICATIONS

I. SCI & SSCI & Arts and Humanities:

Tasel, S.F., Mumcuoglu, E.U., Hassanpour, R.Z., Perkins, G., 2016. A validated active contour method driven by parabolic arc model for detection and segmentation of mitochondria. J. Struct. Biol. 194, 253–271. doi:10.1016/j.jsb.2016.03.002

Mumcuoglu, E.U., Hassanpour, R., **Tasel, S.F.**, Perkins, G., Martone, M.E., Gurcan, M.N., 2012. Computerized detection and segmentation of mitochondria on electron microscope images. J. Microsc. 246, 248–265. doi:10.1111/j.1365-2818.2012.03614.x

II. International Conferences and Proceedings:

Tasel, S.F., Hassanpour, R., Mumcuoglu, E.U., Perkins, G.C., Martone, M., 2014. Automatic detection of mitochondria from electron microscope tomography images: a curve fitting approach, in: SPIE Medical Imaging 2014. p. 903449. doi:10.1117/12.2043517

III. National Conferences and Proceedings:

Taşel, F.S.,2012. Hough Dönüşümünün Dairesel Şekil Tespiti İçin CUDA Üzerinde Paralelleştirilmesi, in: 5. Mühendislik ve Teknoloji Sempozyumu Bildiri Kitabı, Çankaya Üniversitesi, Ankara.

Taşel, F.S., Sönmez A.B.,2010. Metinden Bağımsız Otomatik Konuşmacı Tanıma Sistemleri ve Performans Karşılaştırması, in: 3. Mühendislik ve Teknoloji Sempozyumu Bildiri Kitabı, Çankaya Üniversitesi, Ankara.

IV. Others:

Taşel, F.S., Temizel A., 2012. Parallelization of Hough Transform for Circles using CUDA, in: GPU Technology Conference 2012.

VITA

Faris Serdar Taşel was born in Sultandağı, Afyonkarahisar on August 27, 1981. He received his B.S. and M.S. degrees in Computer Engineering from Çankaya University in August 2004 and in June 2008 respectively. He worked in Çankaya University as a research assistant in Department of Computer Engineering from 2005 to 2012. He continued to work as a lecturer in Çankaya University afterwards. His research interests include image processing, computer vision and GPU computing.